

# Università degli Studi di Napoli Federico II



DI

C

Ma

PI

Dipartimento  
di Ingegneria Chimica,  
dei Materiali e della  
Produzione Industriale  
Università degli Studi  
di Napoli Federico II

***PHD PROGRAM IN  
INDUSTRIAL PRODUCT AND PROCESS  
ENGINEERING  
XXXIII CYCLE***

***FLAME-FORMED CARBON NANOPARTICLES:  
SYNTHESIS AND CHARACTERIZATION***

**2018-2020**

**Supervisor:**

Prof. Andrea D'Anna

**Scientific Committee:**

Dott. Ing. Mario Commодо  
Dott.ssa Patrizia Minutolo

**Coordinator:**

Prof. Andrea D'Anna

**PhD Student:**

Francesca Picca

**Matr.:** DR993083

## **CONTENTS**

<b><u>ABSTRACT .....</u></b>	<b><u>3</u></b>
------------------------------	-----------------

<b><u>CHAPTER 1:INTRODUCTION .....</u></b>	<b><u>6</u></b>
--	-----------------

1.1	NANOPARTICLES AND NANOSTRUCTURED MATERIAL .....	6
1.1.1	NANO-WORLD .....	6
1.1.2	CLASSIFICATION OF NANOMATERIALS.....	8
1.1.3	HISTORY AND SOURCES.....	12
1.1.4	METHODS OF SYNTHESIS.....	13
1.1.5	FLAME SYNTHESIS .....	14

<b><u>CHAPTER 2:AIM OF THE THESIS .....</u></b>	<b><u>17</u></b>
---	------------------

<b><u>CHAPTER 3: STATE OF THE ART ON FLAME FORMED CARBON NANOSTRUCTURE .....</u></b>	<b><u>19</u></b>
--	------------------

3.1	FLAME FORMED CARBON NANOPARTICLES.....	19
3.1.1	DIAMOND .....	21
3.1.2	GRAPHITE AND GRAPHENE.....	22
3.1.3	FULLERENE .....	25
3.1.4	CARBON NANOTUBES.....	28
3.1.5	CARBON DOTS .....	31
3.2	FORMATION PROCESS OF FLAME CARBON NANOPARTICLES .....	35
3.2.1	GAS PHASE-REACTION .....	37
3.2.2	PARTICLE NUCLEATION .....	38
3.2.3	SURFACE GROWTH AND PARTICLE COAGULATION.....	43
3.2.4	OXIDATION .....	45
3.3	DOPED FLAMES .....	46

<b><u>CHAPTER 4: EXPERIMENTAL SET-UP, METHODS AND DIAGNOSTICS .....</u></b>	<b><u>51</u></b>
---	------------------

<b><u>4.1 PREMIXED LAMINAR FLAME REACTOR .....</u></b>	<b><u>51</u></b>
--	------------------

<b><u>4.2 SAMPLING METHODS .....</u></b>	<b><u>52</u></b>
--	------------------

## **4.3 EXPERIMENTAL TECHNIQUES ..... 56**

4.3.1 DIFFERENTIAL MOBILITY ANALYSIS (DMA) .....	56
4.3.2 RAMAN SPECTROSCOPY .....	57
4.3.3 ELECTRON PARAMAGNETIC RESONANCE (EPR).....	61
4.3.4 NUCLEAR MAGNETIC RESONANCE (NMR).....	70

## **4.4 DENSITY FUNCTIONAL THEORY (DFT) ..... 80**

4.4.1 MULLIKEN POPULATION ANALYSIS.....	85
---	----

## **CHAPTER 5: RESULTS..... 87**

5.1 STUDY OF CARBON NANOPARTICLES EVOLUTION IN A LAMINAR PREMIXED FLAME. THE ROLE OF RADICALS IN CARBON CLUSTERING AND SOOT INCEPTION. ....	87
5.1.1 SIZE DISTRIBUTION.....	88
5.1.2 EPR AND RAMAN SPECTROSCOPY .....	89
5.2 SOOT INCEPTION: A DFT STUDY OF $\sigma$ AND $\pi$ DIMERIZATION OF RESONANTLY STABILIZED AROMATIC RADICALS .....	101
5.2.1 PHENALENYL RADICAL .....	103
5.2.2 PAHS RADICAL: ENERGY AND DIMERIZATION .....	105
5.2.3 ELECTRONIC BANDGAP CALCULATIONS .....	111
5.3 CHARACTERIZATION OF INCIPIENT SOOT PARTICLES BY NUCLEAR MAGNETIC RESONANCE SPECTROSCOPY .....	114
5.4 RADICALS IN NASCENT SOOT FROM LAMINAR PREMIXED ETHYLENE AND ETHYLENE- BENZENE FLAMES .....	123

## **CHAPTER 6: CONCLUSIONS..... 135**

## **BIBLIOGRAPHY ..... 140**

## **APPENDIX: PUBLICATIONS ..... 168**

## ABSTRACT

Nanoparticles and nanostructured materials characterize an increasing research area, gaining strong attention from the scientific community in several fields. During the last decades, many and extraordinary technological advances have been obtained by nano-materials due to their physicochemical properties. In nature, at micro- and nano-scale, materials have existed for a long time before, but it is only through the advent of the technological era, and consequently, the development of nanotechnology, that they have come to the fore.

There are several forms of nanoparticles: metal-based, organic-based or organic/inorganic combination and carbon-based ones.

Carbon nanoparticles are the most widely studied as carbon is suitable and available raw material. Except for hydrogen, carbon has the most significant number of known compounds and is present on the planet in various forms: from carbon to light and heavy hydrocarbons. Carbon-based nanoparticles have shown a wide variety of structural arrangements that make them a great advantage as they are suitable for various purposes.

Several techniques exist to cope with the production of the nano-size materials in both liquid and gas phase; examples are arc-discharge, laser ablation, chemical vapour deposition. The more the process allows to have a production (functional to specific final characteristics of the material) on a large scale and in an economical way, the more it is taken into consideration and studied.

Among the various techniques, the use of flame and, therefore, combustion technology is increasingly taken into consideration. Traditionally, combustion is associated with the study of particulate matter and undesired products released into the atmosphere daily to understand the onset of their formation and reduce, if not abate, their emissions. Nevertheless, on the other hand, flame-formed carbon nanoparticles have been the subject of increasing interest in recent decades as a new procedure for synthesizing engineered nanoparticles.

In order to obtain flame nanoparticles with desired characteristics and with the highest yield, it is necessary to have an in-depth knowledge of their formation process through the reaction system, the flame. It is necessary to delve into the chemical and physical details of the various steps of the mechanism that lead to the final product; pay attention to the inherent characteristics of the particles, such as size distribution, chemical composition, and physical characteristics.



Moreover, depending on the final product to be obtained, flames can be modulated and varied in parameters such as temperature, residence time, mixing effect, and the fuel or additive structure.

This PhD thesis focuses on studying and characterizing the carbon nanoparticles synthesized in the well-controlled combustion conditions of premixed fuel-rich flame, using a lab-scale reactor constituted by flat laminar ethylene/air premixed flame. The primary purpose of this activity has been to perform an experimental study on flame-formed carbon nanoparticles, with great attention on the still too unclear step of particle formation in flame, i.e. the nucleation.

The first year of the PhD was primarily centred on the study and preliminary characterization of physicochemical evolution of flame-formed carbon nanoparticles. In order to produce different sizes of particles, carbon nanoparticles were collected at different distances from the flame front, i.e., the residence time in the flame was changed.

Then, various techniques were used to characterize the produced particles.

One of the first investigations was performed in the flame by the on-line differential mobility analyzer to study the particle size distribution. Subsequently, the analytical tools continued with ex-situ techniques such as Raman spectroscopy and Electron Paramagnetic Resonance, the former for chemical and structural information on particles modification and the latter to reveal and confirm the presence of radicals and to identify them.

In this thesis, great attention was laid on the presence and role of radical species, above all, in the determining step of nucleation. For this reason, the research continued in the second year with a more detailed analysis of radical formation in the flame products mechanism and a more specific structural characterization of carbon nanoparticles. Indeed, a density functional theory study investigated some aspects related to the behaviour of radical molecules in flame in terms of dimerization and formation of cluster structures. Notably, the study was helpful in the differentiation between  $\sigma$ - and  $\pi$ -radicals. Following the theoretical evaluation of the radical molecules, the question was raised about how such radicals could form, i.e., whether specific structural elements could facilitate their formation and, consequently, direct carbon particles' formation through a specific mechanism. This type of structural investigation was performed through the Proton Nuclear Resonance Spectroscopy,  $^1\text{H-NMR}$ ; for the first time used in a system such as the one studied in this thesis work.

Then, in the third and final year of this PhD research work, a comparative physicochemical evolution study in an aromatic fuel environment has been performed. The addition of an aromatic dopant, such as benzene, leads to some

change in the flame and the particle formation in terms of particles size distribution, Raman features, and especially radical production, allowing to face up the same questions in such environment and to investigate the effect of aromatic fuel on the nature and the role of radicals in particle nucleation and growth.

# CHAPTER 1:INTRODUCTION

## 1.1 NANOPARTICLES AND NANOSTRUCTURED MATERIAL

Nanoparticles (NPs) and nanostructured materials (NSMs) characterize an area of ongoing research. These structures have gained prominence in many scientific fields and outstanding technological advancements due to their tunable physicochemical characteristics such as melting point, wettability, electrical and thermal conductivity, catalytic activity, light absorption, and scattering enhanced performance over their bulk counterparts (Jeevanandam *et al.*, 2018).

NPs and NSMs have not recently emerged with the development of nanotechnology. Many micro and nanoscale structured materials have existed for decades as well as many industrial processes (e.g. polymer and steel production) have also been exploiting nanoscale phenomena for decades. The nature itself is full of nanoscale structures, such as milk (a nanoscale colloid), proteins, cells, bacteria, and viruses.

### 1.1.1 NANO-WORLD

The prefix "nano", derived from the Greek *Nanos* signifying *dwarf*, is becoming increasingly common in the scientific literature (Nouailhat, 2010). Nano is commonly used as an adjective to describe objects, systems, or phenomena with characteristics arising from a nanometer-scale structure. *Nano* is also a famous label for modern science, and many nano- words have recently appeared in dictionaries, including nanometer, nanoscale, nanoscience, nanotechnology, nanostructure, and nanotube, nanowire, nanorobot (Buzea, Pacheco and Robbie, 2007).

The birth of the nano-concept in the scientific context may be associated to a famous speech by Richard Feynman at the December 1959 meeting of the American Physical Society where he asked, "What would happen if we could arrange the atoms one by one the way we want them?" (Feynman, 1959, 2002).

According to the International System of Units (SI), the first definition provided in this area is the nanometer (nm) that, according to the International

System of Units (SI), denotes a sub-multiple of the length measurement unit precisely  $10^{-9}$  meter.

In principle, NMs are defined as materials with a length of 1–1000 nm in at least one dimension, but they are also commonly defined to be of diameter in the range of 1 to 100 nm.

Indeed, unfortunately, a single internationally accepted definition for NMs does not exist. Different organisations, such as the Environmental Protection Agency (EPA) ("Question about Nanotechnology" 2012), The US Food and Drug Administration (USFDA) ("FDA Guidance on NanotechnologyDOCUMENT: Guidance for Industry Considering Whether an FDA-Regulated Product Involves the Application of Nanotechnology," 2011), The International Organization for Standardization (ISO) ("Nanotechnologies — Vocabulary — Part 1: Core Terms" 2015) and EU Commission (European Commission, 2011) use to define the NMs differently.

Recently, the British Standards Institution (British Standards Institution, 2017) proposed the following definitions for the scientific terms:

- *Nanoscale*: Approximately 1 to 1000 nm size range;
- *Nanoscience*: The science and study of matter at the nanoscale. Nanoscience deals with understanding the size and structure-dependent properties of the matter, and it compares differences between emerging individual atoms, molecules or related bulk material;
- *Nanotechnology*: Manipulation and control of matter on the nanoscale dimension using scientific knowledge of various industrial and biomedical applications. It is possible to define nanotechnology as the design, synthesis, and application of materials and devices whose size and shape have been engineered at the nanoscale, exploiting unique chemical, physical, electrical, and mechanical properties;
- *Nanomaterial*: Material with any internal or external structures on the nanoscale dimension and material that has structural components smaller than 1 nanometer in at least one dimension;
- *Nanoparticle*: Nano-object with three external nanoscale dimensions. The terms nanorod or nanoplate are employed instead of nanoparticle (NP) when the longest and the shortest axes lengths of a nano-object are different. NPs can have amorphous or crystalline form, and their surfaces can act as carriers for liquid droplets or gases.

Many authors limit the size of nanomaterials to 50 nm (Kittelson, 2001) or 100 nm (Borm *et al.*, 2006), justifying this upper limit choice according to the

situation in which some nanoparticles' physical properties approach those of bulk when their size reaches these values. However, this size threshold varies with material type and cannot be the basis for such a classification;

- *Nanofiber*: When two similar exterior nanoscale dimensions and a third larger dimension are present in a nanomaterial;

- *Nanocomposite*: Multiphase structure with at least one phase on the nanoscale dimension;

- *Nanostructure*: Composition of interconnected constituent parts in the nanoscale region;

- *Nanostructured materials*: Materials containing internal or surface nanostructure.

Moreover, a branch of toxicology has been defined as *Nanotoxicology* to address the adverse health effects caused by nanoparticles (Donaldson *et al.*, 2004). Despite suggestions that Nanotoxicology should only address the toxic effects of engineered nanoparticles and structures (Oberdörster, Oberdörster and Oberdörster, 2005), it should also encompass the toxic effects of atmospheric particles and the toxic effect of the particles belonging to the virology and bacteriology field.

Moreover, more attention should be taken to the presence of free NP that when quickly released into the environment lead to human exposure, which can cause serious health risks. On the contrary, fixed nanoparticles, firmly attached to a larger object, should not pose a health risk when handled correctly.

Besides, it is also imperative to recognise that not all nanoparticles are toxic (Derfus, Chan and Bhatia, 2004; Goodman *et al.*, 2004; Connor *et al.*, 2005), but very often, the NPs appears to have positive effects (Bosi *et al.*, 2003; Schubert *et al.*, 2006).

### 1.1.2 CLASSIFICATION OF NANOMATERIALS

The NPs and NSMs could be organised into four material-based categories:

- Carbon-based nanomaterials containing carbon are found in various morphology such as hollow tubes, ellipsoid, spheres. Fullerenes (C60), carbon nanotubes (CNTs), carbon nanofiber, carbon black, graphene, carbon onions are some examples of carbon-based NMs;

- Inorganic-based nanomaterials include metal and metal oxide. These NMs consist of Ag, Au, or a metal oxide such as TiO<sub>2</sub>, ZnO, SiO<sub>2</sub>.
- Organic-based nanomaterials include NMs made from organic matter.
- Composite-based nanomaterials, multiphase NMs and NSMs could combine different NPs or combine NPs with larger and more complicated structures.

In addition to this generic classification, it is essential to classify the NPs and NSMs more precisely according to their size, morphology, composition, uniformity, and agglomeration.

Moreover, nanoparticles can exist as dispersed aerosols, as suspensions/colloids, or in an agglomerated state based on their chemistry and electro-magnetic properties.

The first idea for NM classification was given by Gleiter et al. (Gleiter, 2000) when they considered the crystalline forms and chemical composition of NM but not their dimensionality (Tiwari, Tiwari and Kim, 2012). Subsequently, Pokropivny and Skorokhod made a new classification scheme for NMs, which included the composites' dimensionality, defined as 0D, 1D, 2D, and 3D NMs shown in Figure 1.1 (Pokropivny and Skorokhod, 2007). This kind of classification is highly dependent on the electron movement along the dimensions in the NMs. For example, electrons in 0D NMs are entrapped in dimensionless space, whereas 1D NMs have electrons that can move along the x-axis, which is less than 100 nm. Likewise, 2D and 3D NMs have electron movement along the x–y-axis, and x, y, z-axis, respectively (Al-Hakkani, 2020).

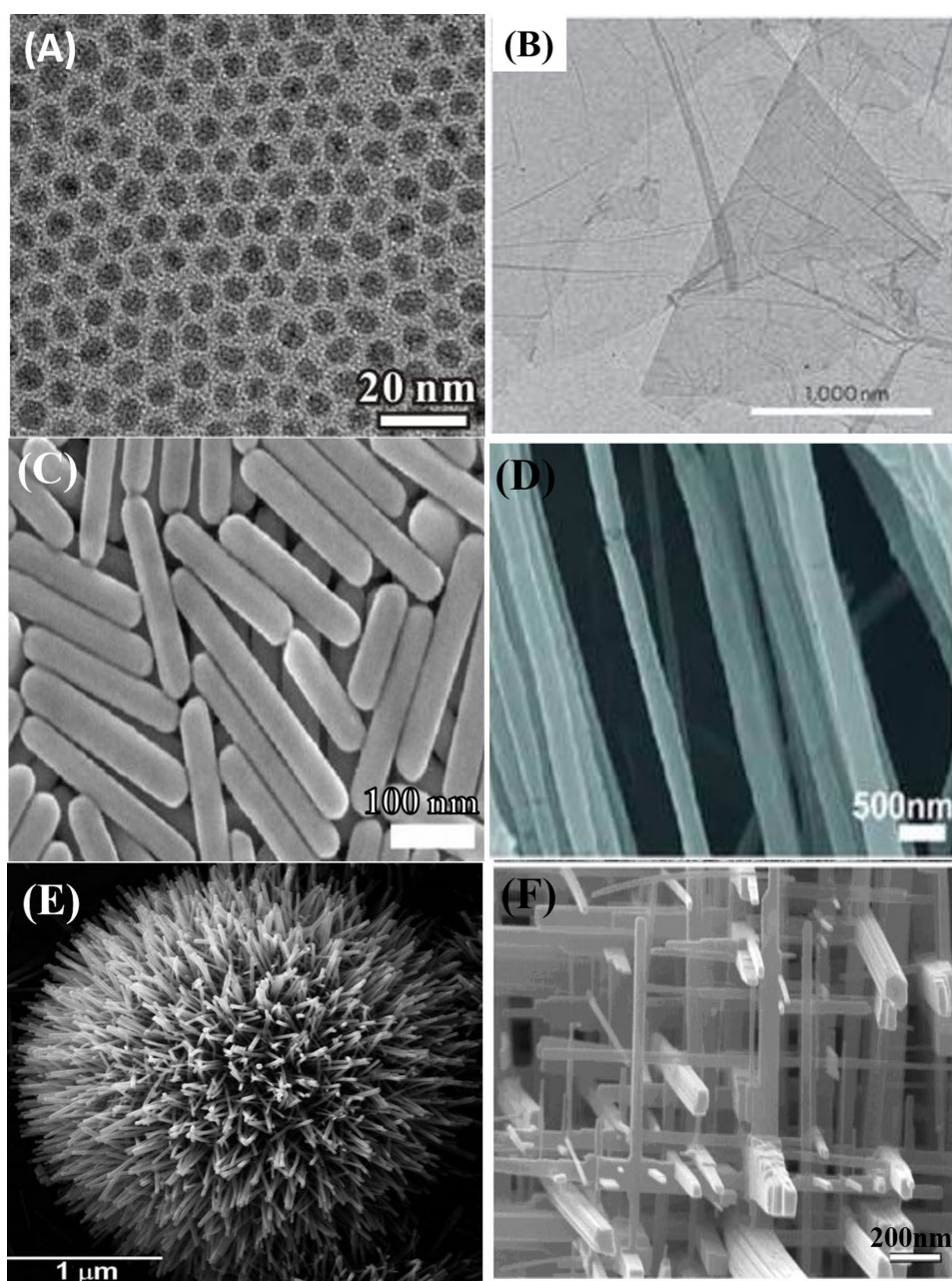


Figure 1.1: Nanomaterials with different morphologies: (A) nonporous Pd NPs (0D) (Pan, Wang and An, 2009; Zhang *et al.*, 2012), copyright Zhang *et al.*; licensee Springer, 2012, (B) Graphene nanosheets (2D) (Li, Adamcik and Mezzenga, 2012), copyright 2012, Springer Nature, (C) Ag nanorods (1D) (Zhang, Langille and Mirkin, 2011), copyright 2011, American Chemical Society, (D) polyethylene oxide nanofibers (1D) (Badrossamay *et al.*, 2010), copyright 2010, American Chemical Society, (E) urchin-like ZnO nanowires (3D), reproduced from (Gokarna *et al.*, 2014) with permission from The Royal Society of Chemistry, (F) WO<sub>3</sub> nanowire network (3D) (Zhou, Ding, *et al.*, 2005), copyright 2005 Wiley-VCH.

Apart from the previous classification, the NPs can also be classified based on their origin, natural nanomaterials, and synthetic or engineered nanomaterials. The former includes NMs produced by biological species or through anthropogenic activities. Nature is full of sources readily available. Naturally occurring NMs are present through the Earth's spheres (i.e., in the hydrosphere, atmosphere, lithosphere, and even in the biosphere), regardless of human actions. Earth comprises NMs that are naturally formed and are present in oceans, lakes, rivers, groundwater, and hydrothermal vents, rocks, soils, magma or lava at stages of evolution and in the form of micro-organisms and higher organisms, including humans (Hochella, Spencer and Jones, 2015; Sharma *et al.*, 2015).

The latter is produced by mechanical grinding, engine exhaust, smoke, or synthesised by physical, chemical, biological, or hybrid methods. Simple combustion during cooking, in vehicles, fuel oil and coal for power generation (Linak, Miller and Wendt, 2000), aeroplane engines, chemical manufacturing, welding, ore refining, and smelting are some of the anthropogenic activities that lead to NP formation (Rogers *et al.*, 2005).

NMs such as carbon NPs (De Volder *et al.*, 2013), TiO<sub>2</sub> NPs (Weir *et al.*, 2012), and hydroxyapatites (Sadat-Shojai *et al.*, 2010) are present in commercial cosmetics, sporting goods, sunscreen, and toothpaste. Moreover, owing to their peculiar properties, Transition Metal Oxides (TMO) NMs, have gained a significant increase in their application as essential components in various sectors, including in the fields of photocatalysts (Pal and Sharon, 2002; Tian *et al.*, 2003), luminescence (Zheng Wei Pan, Zu Rong Dai and Zhong Lin Wang, 2001; Kind *et al.*, 2002), piezoelectric transducers and actuators (Arul Dhas & Gedanken, 1997; Bowles, 1997; W. Gao & Li, 2009; Gulino *et al.*, 1996; Y. Liu *et al.*, 1996; M. Anpo, M. Kondo, Y. Kubokawa, C. Louis, 1988; P. M. Martin *et al.*, 2000; YQ. Huang, M.D. Liu, Y.K. Zeng, 2001; Zhou *et al.*, 2003), electrochromic (EC) displays (Xavier Marguerettaz and Donald Fitzmaurice, 1994; Carotta *et al.*, 1999), high-performance anodes in Li-ion batteries (Huang, 1995; Graetz *et al.*, 2003; Kim and Cho, 2008; Lee *et al.*, 2008), gas-sensing components (Ferroni *et al.*, 1997; Xu *et al.*, 2000), data storage media (Bergeron *et al.*, 2004), optical absorption and emission (Singh and Chauhan, 2014), biosafety and biocompatibility (Yi, Wang and Park, 2005), among others.



### 1.1.3 HISTORY AND SOURCES

NPs and NMs, present in nature, have been used since ancient times by humans for various purposes.

For instance, the synthesis of metallic NPs via chemical methods dates back to the 14<sup>th</sup> and 13<sup>th</sup> century BC by Egyptians and Mesopotamians to build some glasses. These events signed the beginning of the metallic nanoparticles era. In the following centuries, the production of NPs developed in many cultures and populations. In 1857, Michael Faraday reported the synthesis of a colloidal Au NP solution, which represented the first scientific report for NPs preparation and initiated the history of NMs in the modern scientific arena (Faraday, 1857). He also revealed that the optical characteristics of Au colloids are dissimilar compared to their respective bulk counterpart. Today manufactured NMs can significantly improve the characteristics of bulk materials in terms of strength, conductivity, durability, and lightness, and they can provide functional properties (e.g., self-healing, self-cleaning, anti-freezing, and antibacterial) and can function as reinforcing materials for construction or sensing components for safety (Faraday, 1857).

Moreover, although we usually associate air pollution nanoparticles with human activities - automobiles, industry, and coal combustion— it is known that nanoparticles are abundant in nature. All these elements can produce such vast quantities of nanoparticulate matter that profoundly affect air quality worldwide. The aerosols generated by human activities are estimated to be only about 10% of the total, the remaining 90% having a natural origin (Taylor, 2002).

Sources of nanomaterials can be classified into three main categories based on their derivation (Jeevanandam *et al.*, 2018):

- incidental nanomaterials, which are those produced as by-products of industrial and natural processes such as nanoparticles produced from vehicle engine exhaust, welding fumes, combustion processes, forest fires;
- engineered nanomaterials, which humans have manufactured to have specific required properties for desired applications;
- naturally produced nanomaterials, found in the bodies of organisms, insects, plants, animals, and humans.

Molecules are made up of atoms, which are the base structural components of all living and nonliving organisms in nature. Atoms and molecules have been manipulated several times by nature to create intricate NPs and NSMs that

continually contribute to Earth's life. Incidental and naturally occurring NMs are continuously formed and distributed throughout ground and surface water, the oceans, continental soil, and the atmosphere. One of the main differences between incidental and engineered NMs is that engineered NMs have better-controlled morphologies than incidental NMs; additionally, engineered NMs can be purposely designed to exploit novel features that stem from their small size. It is known that metal NPs may be spontaneously generated from synthetic objects, which implies that humans have long been in direct contact with synthetic NMs and that macroscale objects are also a potential source of incidental nanoparticles in the environment.

#### 1.1.4 METHODS OF SYNTHESIS

As previously said, NPs are characterised by specific physicochemical, structural, and morphological characteristics, which are essential to define the field in which NPs are used, such as electronic, optoelectronic, optical, electrochemical, environment, biomedical fields.

There are two basic approaches commonly employed to prepare NPs (Dhand *et al.*, 2015):

- the top-down approach, where the initial structure is macroscopic. There is an externally-control in the process of nanostructures. Besides, in this approach, there are mechanical-physical particle production processes. The typical mechanical-physical crushing methods for producing nanoparticles are photolithography, electron beam lithography, milling techniques, anodisation, ion, laser ablation and plasma etching;

- In the bottom-up approach, atoms or molecules build-up to create nanostructures. By a self-assembly process, atomic/molecular components lead to more complex structures but better-controlling size, shapes, and size ranges. During self-assembly, the physical forces operating at the nanoscale combine basic units into larger stable structures. Examples of bottom-up methods include self-assembly of monomer/polymer molecules, chemical or electrochemical nanostructural precipitation, sol-gel processing, laser pyrolysis and chemical vapour deposition (CVD).

In turn, the bottom-up approach splits into gas-phase and liquid-phase processes, better known as wet-chemistry. Despite the significant advantages that

wet chemistry can offer, there are still significant disadvantages in cost, purity, industrial scale-up, stability, and low yields. Conversely, the gas-phase process allows an artificial generation of a controlled high-temperature environment with several techniques such as plasma arc (Meyyappan, 2009), laser ablation (Amans *et al.*, 2009), chemical vapour deposition (Philippe *et al.*, 2007). However, these techniques' energy investment can strongly affect the process's final cost (Rosner, 2005; Roth, 2007; Strobel and Pratsinis, 2007; Camenzind, Caseri and Pratsinis, 2010; Merchan-Merchan *et al.*, 2010).

#### 1.1.5 FLAME SYNTHESIS

As mentioned in paragraph 1.1.4, to face the NPs production issue, several techniques have been tested through the years, and the production of nanomaterial on a large scale is one of the most important efforts. For this purpose, among various techniques, one of the most prominent is flame synthesis, which remains the most cost-effective advantageous method.

A flame can produce the necessary temperature conditions for the process of sustainability instantly. Flame synthesis does not require an additional energy source, but it is generated in situ driving reactions for particle formation in a faster process. In other cases, flame synthesis can represent almost the only method to implement a synthesis process.

A large-scale production needs continuous processes as that of the continuous feeding of precursors in the reactor. Flame reactors have demonstrated that adding fresh reactants or additives to the system to obtain a stable reactive process is quite simple, especially compared with other processes. This key point makes the flame synthesis of great interest in lab-scale analysis and actual industrial processes. The flame synthesis has numerous advantages; indeed, it is a method that does not involve the tedious steps of wet chemistry; it gives high products with a high degree of purity and without liquid by-products (Pratsinis and Mastrangelo, 1989).

However, flame combustion's high temperature may cause undesired products, and some combustion by-products are the subject of this thesis because they could be engineered and functionalised for many industrial purposes.

Flame-made particles have been part of history for millennia. Owing to its simplicity, flame technology represents a method capable of producing nanoparticles and nanofibers at a scale of several million metric tons annually. For

instance, flame-generated materials include carbon blacks and the highly ordered nanostructured carbon materials (such as carbon nanotubes, fullerenes, and fullerene derivatives), fumed silica, titanium dioxide or titania with and without pigmentary properties and optical fibres (Kammler, Mädler and Pratsinis, 2001; Richter *et al.*, 2008). Flames are routinely used for the synthesis of various single oxide nanoparticles such as  $\text{TiO}_2$ ,  $\text{Al}_2\text{O}_3$ ,  $\text{GeO}_2$ ,  $\text{PbO}$ ,  $\text{V}_2\text{O}_5$ ,  $\text{Fe}_2\text{O}_3$ ,  $\text{SnO}_2$ ,  $\text{ZrO}_2$ , and  $\text{ZnO}$  (Calcote and Felder, 1992; Brezinsky, 1996; Pratsinis, 1998; Wooldridge, 1998; Mädler *et al.*, 2002; Rosner, 2005; Zhou, Gong, *et al.*, 2005). Millions of tons of  $\text{SiO}_2$ ,  $\text{TiO}_2$ ,  $\text{Al}_2\text{O}_3$  (Pratsinis, 1998), and  $\text{ZnO}$  (Tani, Mädler and Pratsinis, 2002) are annually produced through this considerably rapid and inexpensive method. Various combustion-based processes and unique catalytic-fed methods have been employed for the synthesis of TMO nanopowders. It has been shown that reactant mixing, additives, and introduction of electric fields, among others, can be used to control morphology (primary particle size, agglomeration, shape, particle crystallinity) and composition in the flame synthesis.

Each of these parameters influences the characteristics of nanomaterial and so the application field.

Flame synthesis of metal-based nanoparticles starts from precursors of a particular material or a mixture of them. The feeding of these materials (Strobel and Pratsinis, 2007) is operated by the vapour of material or evaporated solution or by injection spray in flame. For all these processes, one of the most critical challenges in flame synthesis, especially for inorganic nanostructure, is the final morphology (Ehrman, Friedlander and Zachariah, 1999; Camenzind, Caseri and Pratsinis, 2010). Starting from the precursors, the formation of the first nuclei is immediately followed by the appearance of aggregates of nanoparticles (Roth, 2007). Time scale control of the process and the reactive system's temperature is fundamental for having a final material with the desired characteristic. The process of sintering occurring at high temperature is the controlling step to produce single spherical nanoparticles. As this time becomes longer, the possibility to produce aggregates and agglomerates increase. The analysis of sintering properties at flame-reactor condition is fundamental for the correct implementation of the process.

Nanocomposite materials made by different metal particles are one of the most advanced sides of the nanotechnology field. The final form of nano-sized material depends on the initial form of precursors, their reciprocal interaction, and the temperature history, which they undergo. Ehrman and co-workers (Ehrman,

Friedlander and Zachariah, 1999) have proposed a general description for the final form of nanoparticles depending on these parameters looking at single nanoparticles and aggregates.

Metal-based nanomaterials and their flame synthesis have increased their range of interest and feasibility.

## CHAPTER 2: AIM OF THE THESIS

This PhD work's primary purpose has been to study, analyze, and characterize carbonaceous nanoparticles generated by the flame process.

The scientific community is interested in this kind of particle for several reasons. For years, it has been trying to improve the flame operating conditions to reduce particulate matter formation, reducing their emission in the atmosphere leading to good advantages for human and environmental health. Then, as shown by recent researches, there is an increasing interest in the collection and characterization of the produced nano-sized carbon particles in the flame to use them as new engineered materials for a variety of application.

A deep knowledge of processes can be a fundamental step to produce carbonaceous nanomaterial with tailored properties such as size, chemical composition, and internal structure.

Initially, a physicochemical evolution of the particles along the flame has been studied. A flame condition suitable for this purpose has been adopted. Specifically, the investigated nanoparticles were generated in a laminar premixed ethylene/air flame with an atomic ratio  $C/O=0.67$  and an equivalence ratio  $\phi=2.01$ . In order to produce different sizes of particles, carbon nanoparticles were collected at different distances from the flame front, i.e., the residence time in the flame was changed.

In-situ and ex-situ techniques were used for characterizing the particles. The first investigation was performed in the flame by the on-line differential mobility analyzer (DMA) to study the particle size distribution. Subsequently, the analytical tools continued with ex-situ techniques such as Raman spectroscopy and Electron Paramagnetic Resonance (EPR), the former for chemical and structural information on particles modification and the latter to reveal and to confirm the presence of radicals and to identify them.

The presence of radicals and the possibility of studying and theorizing their role within the nucleation step has led to increasing interest in computational studies in this thesis work. Through the theoretical study of functional density (DFT), it was possible to study some aspects related to the dimerization of PAHs and their reorganization into clusters. Thus, hypotheses have been put forward on the nucleation process and, therefore, on the formation of incipient molecules, a step still unclear to the scientific community. The formation of dimers from radicals generated by homolytic cleavage on some specific structural elements has

led to the research into specific studies to detect these elements among the collected particles. Specifically, having identified in the previous physicochemical evolution study the height above the burner (HAB), corresponding to a residence time at which probable nucleation occurs, a spectroscopic study by nuclear resonance (NMR) has been performed.

Then, a comparative physicochemical evolution study in a separate fuel environment has been performed. Indeed the addition of an aromatic dopant, such as benzene, leads to some change in the flame and the particle formation in terms of particles size distribution, Raman features, and especially radical generation allow facing up the same questions in a different environment and to investigate the effect of aromatic fuel on the nature and the role of radicals in particle nucleation and growth. For this purpose, two sets of flames have been examined. Each flame set consists of a laminar premixed flame burning pure ethylene and the same flame, i.e., same equivalence ratio, temperature, and unburned gas velocity, in which 30% of ethylene carbon was replaced by benzene.

## CHAPTER 3: STATE OF THE ART ON FLAME FORMED CARBON NANOSTRUCTURE

### 3.1 FLAME FORMED CARBON NANOPARTICLES

The flame phenomena consist of a formation of condensed-phase materials that are nanoparticles suspended in burned combustion gases. The pure hydrocarbon gas combustion leads to the production, in a significant manner, of carbon nanoparticles that are generally related to the formation of soot particles which remain one the most effective pollutant produced, as the undesired product, in ordinary combustion devices (Calcote, 1981; Kennedy, 1997; Richter and Howard, 2000; Bockhorn *et al.*, 2007).

These particles have been the object of several studies in the last decades; most of them concerned human health and environmental/climate change issues. These particles can be easily trapped and accumulated in the human body, causing critical and adverse health effects (Oberdörster *et al.*, 2004; Kennedy, 2007; Pedata *et al.*, 2015; Bhandari *et al.*, 2019). Moreover, soot strongly absorbs solar radiation influencing the Earth's radiative balance through the aerosol-radiation and aerosol-clouds interactions, thus influencing surface albedo and atmospheric stability (Bond *et al.*, 2013). However, these nanoparticles have also aroused the scientific community's interest because of the possibility of using them as potential new low-cost materials with a vast application field (Li *et al.*, 2016). Under controlled synthesis conditions, these carbon nanoparticles may be produced and functionalised to form desirable materials.

Carbon black is probably the most prominent example of carbonaceous flame-made material and, at the same time, the first kind of particles produced by the flame in humanity's history, since it was already used as a pigment in cave paintings or as ancient tattoos ink. Today, the same materials find a great utilisation for many versatile applications such as automobile tires, toners, and catalysts (Kay and Grätzel, 1996), dye-sensitised solar cells (Grätzel, 2003; O'Regan & Grätzel, 1991).

The discovering and isolation of fullerene (Kroto *et al.*, 1985), caused by its suggestive form, paved the way for new materials such as the carbon nanotubes (Iijima, 1991) and graphene sheets (Novoselov *et al.*, 2005), only to cite few examples. Meanwhile, a wide moiety of compounds prevalently made by carbon with nanometric size has been discovered and characterised (Endo and Kroto,



1992; Kroto, 1992; Sattler, 1995; Subramoney, 1998). The main features of these materials have generated a great interest in industrial applications, and great efforts have been spent to increase the selectivity of these materials produced by the combustion process.

Nowadays, there are seven known allotropic forms of carbon as pictured in Figure 3.1, and, as just said, flame synthesis represents one of the methods to produce some of them.

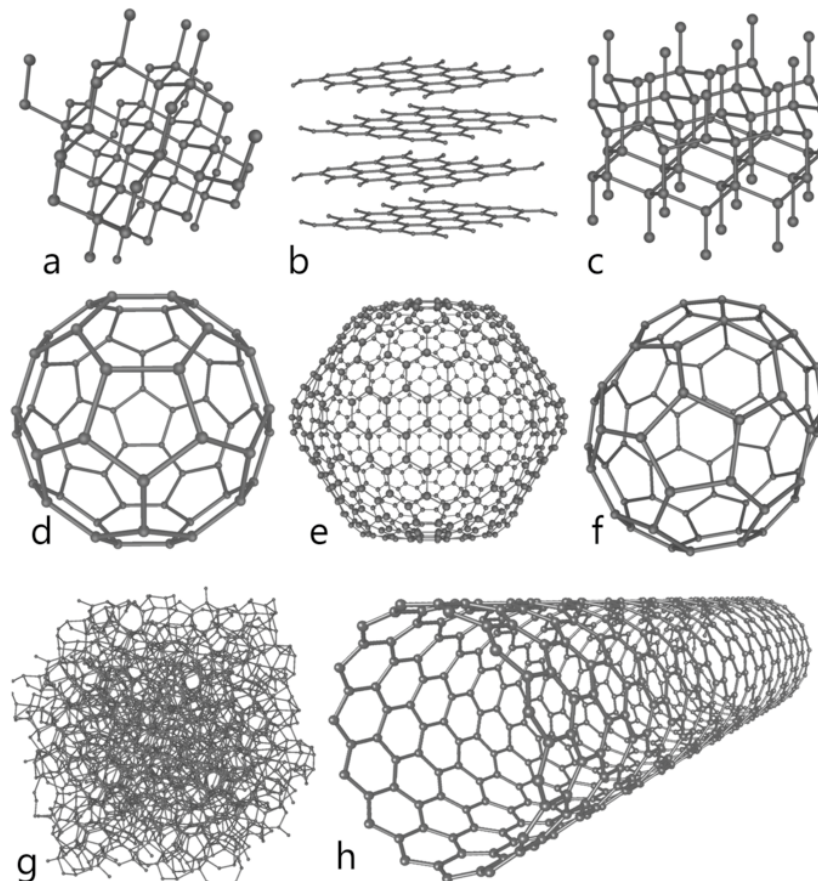


*Figure 3.1 Allotropes of Carbon: a) Diamond; b) Graphite; c) Lonsdaleite; d)-f) Fullerenes C60 (Buckminsterfullerene or buckyball), C540, f) C70; g) Amorphous carbon; h) single-walled carbon nanotube, or buckytube. (Kharisov et al., 2019)*

In the following sections, an overview of the different kinds of the leading carbon nanoparticles that could also be produced by flame will be exposed.

### 3.1.1 DIAMOND

Diamond, Figure 3.2a, is probably the most well known carbon allotrope.

The insert in Figure 3.2b shows the carbon atoms arranged in a lattice which is a variation of the face-centred cubic crystal structure.

Diamond has superlative physical qualities, most of which originate from the strong covalent bonding between its atoms. In a diamond, each carbon atom, hybridised  $sp^3$ , is covalently bonded to four other carbons in a tetrahedron. The rings assume the most stable conformation: the chair. This conformation allows for zero bond-angle strain and makes the diamond a material incredibly strong. Besides, its rigid lattice prevents contamination by many elements. The surface of the diamond is lipophilic and hydrophobic. Diamond polycrystalline films and single-crystal diamond films are expected to find many industry applications precisely because of the unique combination of excellent technological properties such as high hardness, good thermal conductivity, optical transparency, chemical inertness, and wear resistance (Narayan, Boehm and Sumant, 2011). The use of diamonds or large single-crystal diamond films is desirable for coating the cutting tools for machining non-ferrous metals and alloys, but large single-crystal diamonds are not yet readily available. Many methods of low-pressure diamond synthesis have been proposed so far to achieve a good quality diamond, such as thermal chemical vapour deposition (CVD) (Spitsyn, Bouilov and Derjaguin, 1981), the hot-filament method (Hirose and Terasawa, 1986), electron-assisted CVD (Sawabe and Inuzuka, 1985) the microwave plasma CVD (MP-CVD) (Klages, 2008). There has also been substantial attention to the use of flame synthesis to produce diamonds. In 1990, Hirose and Kondo described a flame method to synthesise diamonds in an ambient atmosphere (Hirose, Amanuma and Komaki, 1990). Subsequently, Donnet et al. used a flame method to create large single crystals diamond with the advantage of a high growth rate of diamond films (Donnet *et al.*, 2006).

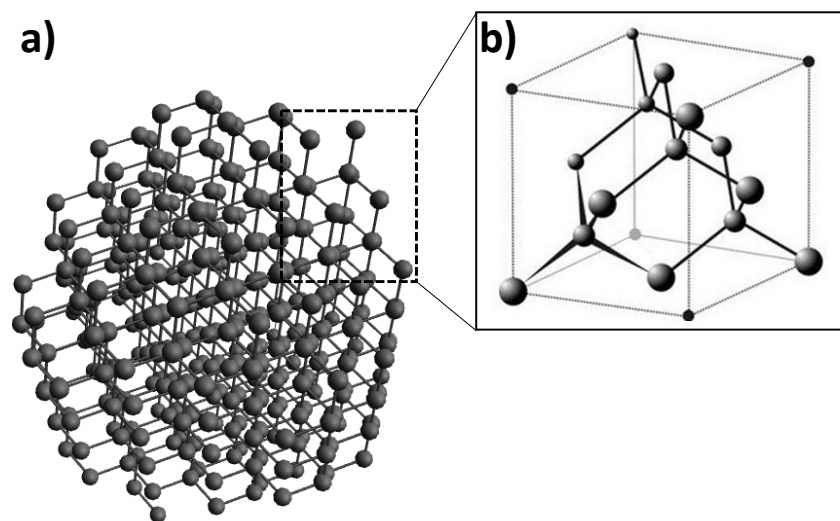


Figure 3.2: a) Diamond representation; b) Diamond lattice. Each  $sp^3$  carbon atom covalently bonds four other carbons in a tetrahedron.

### 3.1.2 GRAPHITE AND GRAPHENE

Graphite, shown in Figure 3.3, unlike diamond, is an electrical conductor and a semi-metal, utilized in thermochemistry as the standard state for defining the heat of carbon compounds' formation (Chung, 2002).

There are three types of natural Graphite (Chung, 2002):

1. Crystalline flake graphite: isolated, flat, plate-like particles with hexagonal edges;
2. Amorphous Graphite: fine particles, the result of thermal metamorphism of coal; sometimes called meta-anthracite;
3. Lump or vein graphite: occurs in fissure veins or fractures, appears as growths of fibrous or acicular crystalline aggregates;

Graphite has a layered, planar structure. In each layer, the carbon atoms arranged in a hexagonal lattice with a separation of 0.142 nm, and the distance between planes (layers) is 0.335 nm. The two known forms of Graphite, *alpha* (hexagonal) and *beta* (rhombohedral), have very similar physical properties (except that the layers stack slightly differently). The hexagonal Graphite may be either flat or buckled. The alpha form can convert itself to the beta form through mechanical treatment, and the beta form reverts to the alpha form when heated

above 1300 °C. There is usually a mixture of these two forms in naturally occurring graphites, containing about 30% of the rhombohedral (beta) form. It is also possible to make Graphite synthetically, giving Graphite prevalently in the alpha form. Graphite can conduct electricity due to the vast electron delocalisation within the carbon layers; as the electrons are free to move, electricity moves through the planes. Graphite also has self-lubricating and dry lubricating properties. Graphite has applications in prosthetic blood-containing materials and heat-resistant materials as it can resist temperatures up to 3000 °C.

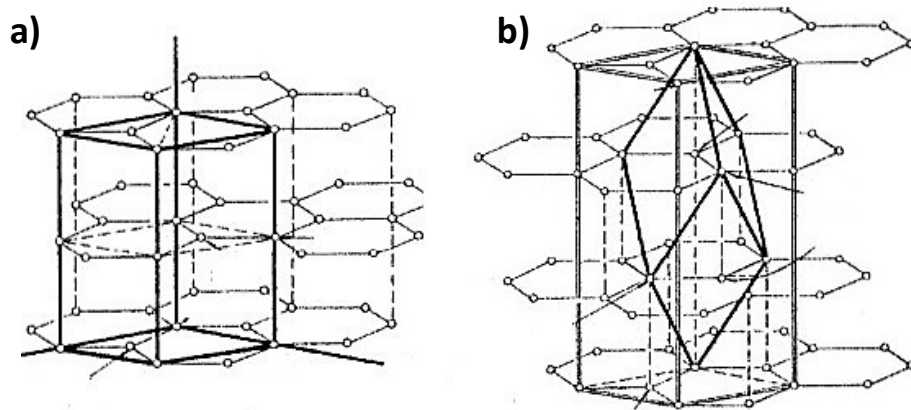


Figure 3.3 Graphite lattice: a) alpha or hexagonal Graphite; b) beta or rhombohedral graphite. The layer is composed of  $sp^2$  carbon with a distance of 0.142 nm and a distance between the planes of 0.335 nm. (Inagaki, 2013)

A single graphite layer is called graphene, presented by the scientific community as the world's thinnest material. This material displays extraordinary electrical, thermal, and physical properties. It consists of a single planar sheet of  $sp^2$  bonded carbons densely packed in a honeycomb crystal lattice. Graphene is the fundamental structural element of carbon allotropes such as graphite, charcoal, carbon nanotubes, and fullerenes. Graphene is a semi-metal or zero-gap semiconductor, allowing it to display high electron mobility at room temperature.

Graphene was isolated by a simple experiment (Novoselov, Geim, et al. 2005; Novoselov, Jiang, et al. 2005), which was worth the noble prize in 2010. Graphene has been characterised experimentally by different groups and studied by modern physics theories for many years (Radovic and Bockrath, 2005; Stauber, Guinea and Vozmediano, 2005). The two-dimensionality of this material gives it excellent properties used for various industrial applications. Indeed, the high conductivity is considered ideal for high-speed electronics (Avouris, 2010; Bonaccorso *et al.*,

2010; Yazyev and Louie, 2010), but it is possible to use it as data energy storage. Recently, there has been significant development of the liquid crystal display (LCD) and organic light-emitting diode (OLED), both produced using a graphene-based electrode that is flexible and more/limitless compared to indium tin oxide. Moreover, graphene-based electrodes could be made low cost while maintaining efficiency (Mahmoudi, Wang and Hahn, 2018), and in this way, it could replace the platinum-based electronics to produce solar photovoltaic cells. The use of graphene extends to self-healing materials, material to space application, gene delivery, and bioimaging (Goenka, Sant and Sant, 2014), tissue engineering (Shin *et al.*, 2016), graphene-based metal-air batteries (Yoo and Zhou, 2011).

Since graphene was discovered, industrialists have been searching for suitable fabrication methods for producing high quality, defect-free, stable and high yield, and cost-effective methodologies. The fabrication methodology of graphene is challenging because the utilisation of this material for various applications mostly depends on fabrication methods on a large scale. Several methods have been applied. Micromechanical exfoliation produces graphene-based materials that involve peeling systematically ordered pyrolytic Graphite using adhesive tape (Sinclair, Suter and Coveney, 2019). After completion of the peeling, multi-layer graphenes remain on the tape. Graphene is sliced into various flakes of few layers by continuously peeling the multi-layer graphene. In this process, layers of graphene are bonded strongly by van der Waals bonding (Rudrapati, 2020).

Liquid phase exfoliation (LPE) is another production method of graphene materials that use a solvent like acetic acid, sulfuric acid, and hydrogen peroxide to exfoliate Graphite through ultrasonication (Cui *et al.*, 2011; Monajjemi, 2017). This method creates graphene nanoribbons, but large-scale graphene growth is a difficult task in this method. CVD is one of the most crucial deposition methodologies used to transition metals.. During the CVD process, a film of metallic catalyst is deposited on the substrate. Chemical etching is performed on the deposited material on the substrate. After chemical etching, a mixture containing the carbon is passed into the reaction chamber, obtaining high-quality graphene (Mattevi, Kim and Chhowalla, 2011; Kidambi *et al.*, 2012; Zhang, Zhang and Zhou, 2013). During pulsed laser deposition (PLD), the laser energy source is outside the chamber, and the chamber is maintained ultrahigh vacuum. In this process, the material is deposited at an angle of 45° between the ablated target and substrate material. During this process, substrates are added to their surfaces parallel to the target at a distance of 2–10 mm. The PLD process's main

advantage is the low-temperature growth rate achieved such that high-quality graphene is made without defects (Tite *et al.*, 2014; Kodu *et al.*, 2016).

Finally, among the methods, there is the flame synthesis that is looked at with great interest for reasons such as making graphene materials exploiting its advantages like scalability and cost-effectiveness (Memon *et al.*, 2011; You *et al.*, 2011), and also it is fast and straightforward (Prihod'ko *et al.*, 2015; Prihod'Ko *et al.*, 2014). When utilising combustion, hydrocarbon gas provides both the high temperature and carbon species necessary for growth on metal substrate resulting in an efficient and robust process. The graphene lattice's growth occurs on transition metals substrate, providing a low energy pathway for hydrocarbon dissociation (Bhaviripudi *et al.*, 2010). However, the growth mechanisms that can lead to the formation of isolated and stable graphene sheets are far from being wholly understood (Whitesides *et al.*, 2009; You *et al.*, 2011).

### 3.1.3 FULLERENE

Fullerenes (also called buckyballs) have been the subject of intense research, because of their unique chemistry and technological applications. Fullerenes occupy an essential role in materials science, electronics, and nanotechnology. They are applied in different fields, from the solar cell (Thompson and Fréchet, 2008) to medicine (Anilkumar *et al.*, 2012). There are many forms of fullerenes (Yang *et al.*, 1995; Zhou, Gong, *et al.*, 2005), showed in Figure 3.4 and 3.5. The most common is the C<sub>60</sub> or buckyball (Hebard, 1993), constituted by 60 Carbon atoms linked together by single and double bonds to form a hollow sphere with 12 pentagonal and 20 hexagonal faces (Kroto *et al.*, 1985). Many possible combinations with other polymers or different species also exist (Brabec *et al.*, 2010).

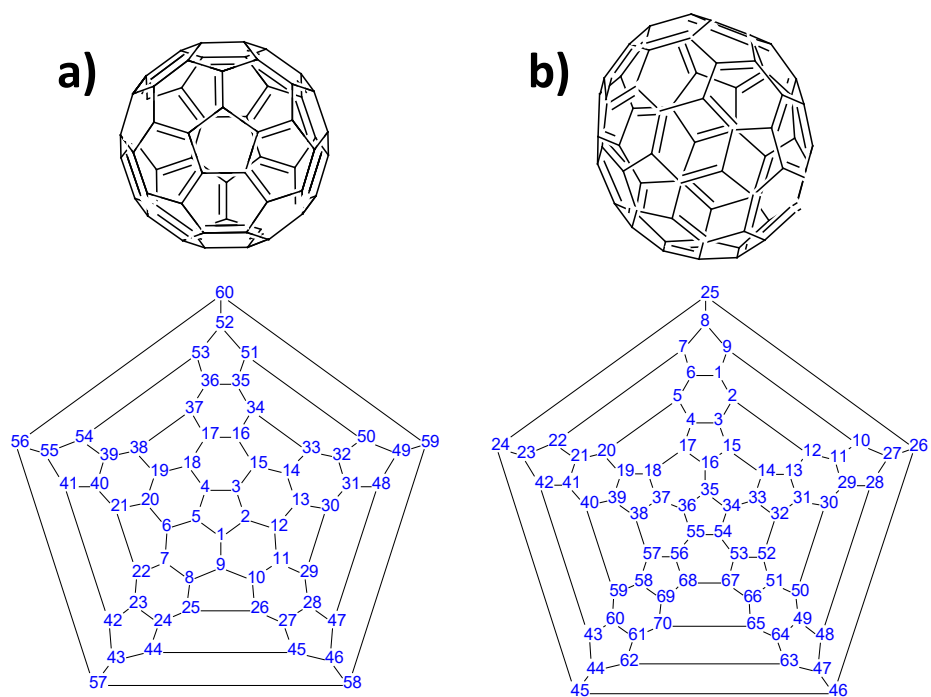


Figure 3.4 A representation of a) C<sub>60</sub> and b) C<sub>70</sub> in the top view. In the bottom view, the visualisation of flat fullerene with a schematisation of Carbons.

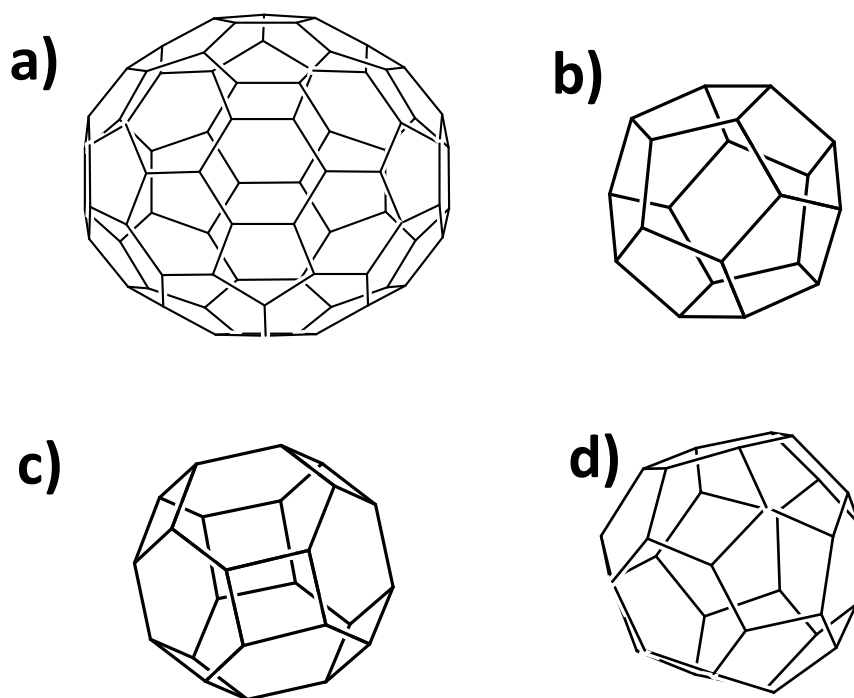


Figure 3.5 A picture of: a) C<sub>78</sub> fullerene; b) C<sub>20</sub> fullerene; c) C<sub>24</sub> fullerene; d) C<sub>32</sub> fullerene.

Innovative developments in fullerene applications are now ongoing, for example, in the fields of lubricants, hard materials, medicines, superconducting materials, and semiconductors. Some studies suggest that commercial uses of C<sub>60</sub> in such diverse areas as fuel cells and pharmaceuticals for AIDS and Parkinson's disease may not be far away (Takehara *et al.*, 2005). Despite the immense possibility of appliances, the fullerenes suffer the difficulty of producing high yield and selectivity concerning undesired products (Kataura *et al.*, 2001). Several methods to produce fullerene have been proposed through years, but the use of flame reactors, already used just after fullerene discovery, remains of great interest for the possibility of easy scale-up to the industrial level. However, the process of fullerenes formation is not entirely understood. Fullerenes were first synthesised through laser vaporisation of carbon in an inert atmosphere, but this laser vaporisation method produced tiny amounts of fullerenes (Geckeler and Samal, 1999). In this method, fullerenes are produced in a supersonic expansion nozzle by a pulsed laser-focused on a graphite target in an inert atmosphere (helium). However, large quantities of fullerene C<sub>60</sub> were later synthesised through arc heating of Graphite and laser irradiation of polyaromatic hydrocarbon (PAHs). The former involves generating an electric arc between graphite rods in an inert atmosphere which produces soot. A fraction of soot contains fullerenes that are extracted by solvation in a small amount of toluene (Montellano López, Mateo-Alonso and Prato, 2011), which then is removed by evaporation. The obtained mixture made up of mostly C<sub>60</sub> with a small amount of higher fullerenes is subjected to liquid chromatography to obtain pure C<sub>60</sub> (Shanbogh and Sundaram, 2015). The latter is based on polycyclic aromatic hydrocarbons (PAHs) that already have the required carbon frameworks. Such PAH molecules are "rolled up" to form fullerenes under flash vacuum pyrolysis (FVP) conditions (Amsharov and Jansen, 2008). It has been reported that a polycyclic aromatic hydrocarbon which consists of 60 carbon atoms, forms fullerene C<sub>60</sub> when it is laser irradiated at 337nm wavelength (Boorum *et al.*, 2001). However, the combustion method is a continuous and easily scalable process, and for this reason, it was considered to have more potential for fullerene production than the other ones. Even if less suitable for fullerenes' laboratory-scale production than the carbon arc, the combustion synthesis method is the technology used in the world's largest fullerene production facility (Murayama *et al.*, 2004). Most previous laboratory investigations of fullerene synthesis via sooting flames have used acetylene, toluene or benzene as the hydrocarbon feedstock (reviewed in (Homann, 1998). Fullerene was believed to be related with the initial steps in soot formation process



(Homann, 1998). The process of fullerene formation has many similarities with soot formation and carbonization (Chung and Violi, 2010).

However, nowadays, fullerene production remains a sub-process of soot formation that can become relevant and dominant only in certain conditions (Howard *et al.*, 1992; Homann, 1998).

### 3.1.4 CARBON NANOTUBES

Carbon nanotubes (CNTs) are cylindrical carbon molecules that exhibit extraordinary strength and unique electrical properties and are efficient heat conductors. CNTs were first discovered by Baker *et al.* in the 1970s (Baker *et al.*, 1972). However, at that time, CNTs did not spark as much interest in the scientific community as Iijima's re-discovery in 1991. For the first time, Iijima observed the CNTs by TEM (Transmission electron microscopy) and subsequently reported the conditions for synthesising large quantities of nanotubes (Iijima, 1991).

CNTs can be described as graphite sheets that are rolled up into cylindrical shapes. CNTs are considered a derivative of both carbon fibres and fullerene with carbons arranged in particular muffled tubes (Polizu *et al.*, 2006). According to the number of carbon layers, two types of carbon nanotubes are classified: single-walled carbon nanotubes (SWCNTs) and multi-walled carbon nanotubes (MWCNTs).

SWCNTs consist of a single graphene layer with a diameter varying between 0.4 and 2 nm and usually occur as hexagonal-packed bundles.

MWCNTs consist of two or several-cylinder, each made up of graphene sheets.

The diameter varies from 1 to 3 nm (Iijima, 1991; Iijima and Ichihashi, 1993). A SWNT can be visualised as a flat graphene sheet rolled up to make a seamless cylinder. The end caps of the nanotube can be visualized as two halves of the fullerene molecule. SWNTs exhibit extraordinary physical properties, including very high thermal and electrical conductivity in the axial direction (Hone *et al.*, 1999; Nanot *et al.*, 2013). A MWNT can be visualized as a structure composed of concentric cylinders of increasing diameters and, at each end, of correspondingly larger hemispherical end caps. However, MWNTs are more "commercial", and their synthesis and production are more considerable than SWNTs. Another classification of CNTs regards the six-member carbon ring orientation in a

honeycomb lattice concerning the nanotube axis. Three possible structures include an armchair, zig-zag, and chiral, as shown in Figure 3.6. Armchair and zig-zag structures are achiral; that is, their mirror image is identical to the original. The main characteristic of chiral structures is the total absence of a symmetry plane that involves the peculiarity of non-superimposable mirror images.

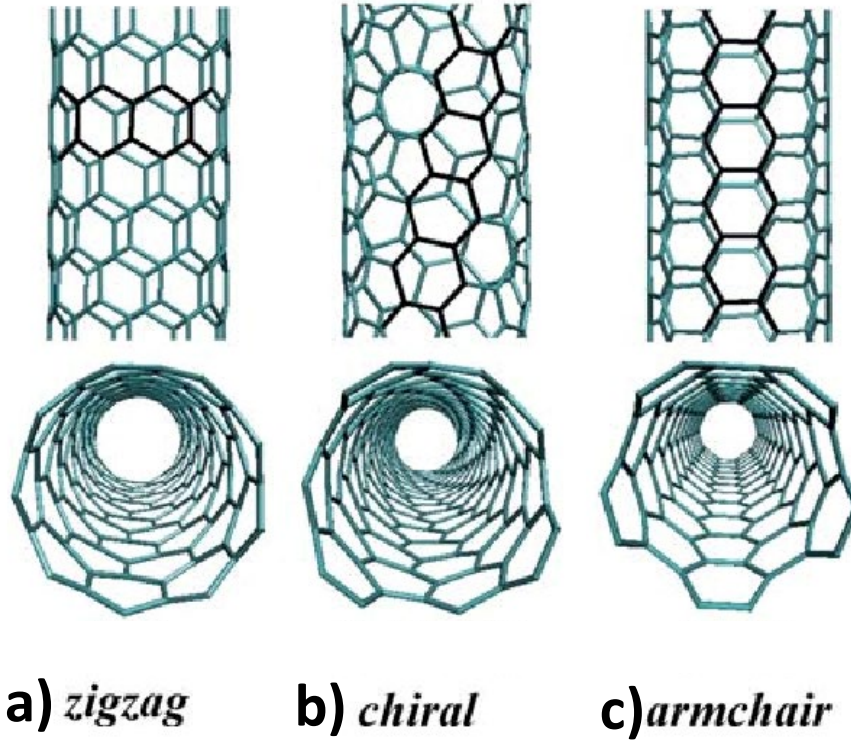


*Figure 3.6 Classification of CNT based on the orientation of the hexagonal in the honeycomb lattice. a) Armchair; b) Zig-zag lattice; c) Chiral lattice. The image is taken from (Galano, 2010).*

Carbon nanotubes have extraordinary material properties, such as high stiffness and strength and excellent electrical and thermal conductivities compared to other promising carbon materials (Gogotsi, 2017). Material properties of carbon nanotubes, including their stiffness and conductivity, have a unique dependence on their atomic structure, size, and geometry. Carbon nanotubes physical properties are different depending on hexagonal carbon rings' orientation in their atomic lattice structure.

Pulsed laser vaporisation (Maser *et al.*, 1998), arc-discharge (Iijima, 1991), and CVD (Cassell *et al.*, 1999) were the first processes to produce carbon

nanotubes. The first process uses a high energy laser which is directed to ablate a carbon target that contains some nickel and cobalt in a tube furnace at the temperature of  $\sim 1400$  K. A flow of inert gas is passed through the chamber to carry the CNTs downstream to a collector surface (Gore and Sane, 2011). The second involved condensation of carbon atoms generated from the evaporation of a solid carbon source. In this method, graphite electrodes, placed at a distance of approximately 1 mm, are used. A high electric current ( $\sim 50 - 120$  A) passes through them in the synthesis chamber, causing sublimation of the material, leading to forming the nanotubes on the anode. The third involves decomposing a hydrocarbon gas over a transition metal catalyst and initiating CNT synthesis by some of the resulting carbon atoms. However, due to high production costs and low feasibility at the industrial scale, an alternative route to produce this material has been investigated. The use of metallic catalysts could address the growth of CNTs in a disordered way or a specific direction (Merchan-Merchan *et al.*, 2010), influencing the possibility to apply this material to various fields (Merchan-Merchan *et al.*, 2010). From this point of view, the control of the process results again of fundamental importance. In this regard, hydrocarbon flames provide a unique combination of the chemical and catalytic factors required for the initiation and growth of carbon nanotubes. Indeed the chemical energy released in the form of heat in the flame supports the endothermic carbon deposition reactions. Catalysts in an appropriate form (substrate or aerosol) provide the reaction sites for solid carbon deposition.

Flame synthesis of CNTs received much attention, and nowadays, a set of reactors have been individuated to produce a noticeable amount of CNTs. Both premixed (Howard *et al.*, 1992; Vander Wal, 2002; Gopinath and Gore, 2007) and diffusion flames (Saito *et al.*, 1991) are suitable for production from many different fuels, generally with a metallic catalyst. As for the fullerenes, CNTs result in a particular pathway of more general high molecular mass aromatic hydrocarbon formation and growth. Soot particles are always present as by-products in the environment and can affect both the material's final form and the global process's costs.

### 3.1.5 CARBON DOTS

Carbon Dots (CDs) is the term to indicate different nano-sized carbon materials.

Generally, all nano-sized materials composed mainly of carbon and possessing at least one dimension smaller than 10 nm in size can be called CDs. CDs always possess fluorescence as their intrinsic properties. The structure of CDs consists of  $sp^2/sp^3$  carbon and oxygen/nitrogen-based groups or polymeric aggregations.

Among the CDs, Carbon quantum dots (CQDs) caught great attention in the scientific community. CQDs are a class of carbon nanomaterials discovered accidentally in 2004 during the purification of SWNTs (Xu *et al.*, 2004), then later Sun *et al.* gave them this name (Sun *et al.*, 2006). This new class of zero-dimensional nanomaterial, with exceptional optical proprieties, contains a carbon core with surface functional groups. The crystallinity of the carbon nucleus and quantum confinement are necessary characteristics that these particles must have to be part of this compound class. Therefore, a nano-sized carbonaceous particle that contains an entire amorphous core and does not display quantum confinement is simply a Carbon Nano Dot (CND).

On the other hand, when a particle displays quantum confinement and possesses a carbon core, it may be classified as a CQD. Essentially quantum confinement is a change of electronic and optical properties when the material sampled is of sufficiently small size; the bandgap increases as the nanostructure's size decreases. As the dot size increases, the emission wavelength red-shifts, and the fluorescence intensity decreases.

One immediate and direct consequence of the quantum effect is the photoluminescence characteristics of CQDs, which is size-dependent. In contrast, carbon nanoparticles necessitate surface passivation or heteroatom doping to modify surface properties and stabilize the optical properties, allowing to tune the photoluminescence (Zhu *et al.*, 2015). Then, the origin of fluorescence, photoluminescence, chemiluminescence proprieties has related to  $sp^2$  domain size and the abundance of oxidised surface defects.

CQDs are spherical particles comprising an amorphous or monocrystalline core with a predominantly graphitic ( $sp^2$  carbon) shell, even though CQDs could have a carbonic core that could have a crystalline and amorphous part.

Many structural models of CQDs core have been suggested, such as a diamond like-structure (Hu *et al.*, 2009), Graphite (Bourlinos *et al.*, 2008; Hola *et al.*, 2014), or amorphous carbon structure (Zhu *et al.*, 2013; Kwon *et al.*, 2015). The surface is functionalised to tune the properties for a selected application. The surface functional groups present on carbon-based quantum particles depend on the precursor used and the reaction conditions. Generally, surface functionalizations, including carboxylic acid, hydroxyl, and amine groups, are created on CQDs' surface using molecular precursors such as citric acid, glucose, or polyethylene di-amine (PEI) to give some examples (Nekouei *et al.*, 2019).

Since their discovery, CQDs have been extensively studied because of the vast plethora of applications. CQDs are provided of an excellent solubility, chemical inertness, high resistance to photobleaching, and also low toxicity and biocompatibility make them materials useful for bioimaging (Antaris *et al.*, 2013), drug delivery (Tang *et al.*, 2013; Feng *et al.*, 2016), biosensing (Andrius *et al.*, 2013; Zhu *et al.*, 2013). Moreover, there is an increasing interest in using these materials in photocatalysis, as light harvesters (Briscoe *et al.*, 2015; Wang *et al.*, 2016), electron donors/acceptors (Kwon *et al.*, 2014; Paulo *et al.*, 2016), and electrode/ electrolyte dopants (Bin Yang *et al.*, 2013) in photovoltaic devices.

Many methods are used to produce and functionalize them, such as laser ablation, chemical and electrochemical oxidation, using the microwave or thermal decomposition. In each method, the obtained CQD underwent a modification process. Unfortunately, a unique method to obtain them advantageously does not exist. All the processes have some advantages and disadvantages because a controlled size and morphology make the process difficult and expensive. On the contrary, when the process is more straightforward and at a low cost, there are problems with the yield, size control, and uniformity.

Laser ablation of carbon-based materials is a fast way to obtain CQDs. Hu *et al.* found that the size control of CQDs can be realised by tuning the laser pulse width (Hu *et al.*, 2011). The interaction between the laser beams and the graphite flakes produces an instant local high-temperature and high-pressure vapour/plasma plume at the graphite flake interface and the surrounding liquid medium. Due to the liquid's confinement, a bubble is formed at the laser focus and quickly expands to a maximum radius. After the end of the a laser pulse , the bubble starts to shrink due to the surrounding liquid's pressure, leading to the cooling of its inner region and forming clusters or nuclei. Bubbles with different cluster densities can be formed when the laser pulse width is changed, further producing CQDs with different sizes (Hu *et al.*, 2011).

Laser ablation of activated carbon (4% ash) in a water/ethanol solution (5:2) was shown by Yogesh et al., forming CQDs of 4 nm in size (Yogesh, Shuaib and Sastikumar, 2017). A one-step process based on laser irradiation of a graphite target using the second harmonic beam at 532 nm of the Nd: YAG in H<sub>2</sub>O/ethanol for the formation of 3 nm-sized CQDs was reported by Tarasenko (Tarasenko *et al.*, 2017).

Conversely, chemical oxidation is a practical and convenient approach for large scale production and requires no complicated devices. Qiao et al. presented a facile approach to produce CQDs, with a size distribution of 2-6 nm, using three typical activated carbons treated by HNO<sub>3</sub> etching and followed by a passivation process (Qiao *et al.*, 2010).

The microwave method allows shortening the reaction time leading to rapid heating and uniform size distribution of quantum dots (Zhai *et al.*, 2012); using sucrose as the carbon source and diethylene glycol as reaction medium resulted in the formation of green luminescent CQDs within only one minute under microwave irradiation (Liu *et al.*, 2014).

All these techniques require high energy consumption and multistep processes, and the doping elements are restricted, which are primarily responsible for the high cost of manufacturing doped carbon, thus limiting their practical applications.

For many years, the formation of carbon-based quantum particles has been achieved by pyrolysis or incomplete combustion of hydrocarbons (Nekouieian *et al.*, 2019), leading to the formation of condensed carbonaceous particles (soot). It was discovered that soot derived from candles or natural gas burners' combustion represents an excellent CQD source. In 2007, Liu et al. collected candle soot that then mixed with oxidising agents and refluxed for 12 h. Successively, CQDs smaller than 2 nm were collected (Liu, Ye and Mao, 2007).

Han et al. adopted a simple combustion flame method to efficiently produce CQDs doped by various heteroatoms (B, N, P, and S) (Han *et al.*, 2015). A technique, which could be applied to the large-scale formation of CQDs for further industrial applications, uses a specific precursor that has added a solution to an alcohol lamp. A beaker was placed on the top of the smouldering flame, and after some hours, a large amount of soot is deposited on the beaker's inner wall. After oxidative acid treatment, the doped CQDs are obtained (Han *et al.*, 2015).

Besides, recently Liu et al. have found a quantum dot behaviour in CNPs, produced by premixed, stretched-stabilised ethylene flames, demonstrating size dependences in their photoemission ionisation energy, optical band gap, and

electrochemical ionisation potential that are consistent with the behaviours of a quantum dot (Liu *et al.*, 2019).

## 3.2 FORMATION PROCESS OF FLAME CARBON NANOPARTICLES

In the previous paragraph, a summary of the leading carbon nanoparticles has been reported. Several methods could produce all CNPs, and for each of them, flame synthesis has been revealed one of the main advantageous methods considering the cost, the facility, the time, the scalability, and the possibility of obtaining stable products owning the control on their size, structure, and morphology. Under controlled synthesis conditions, these CNPs may be produced and functionalised to form desirable materials.

As anticipated, the flame system's high temperature can cause by-products, such as soot particles. Indeed, in many flame phenomena, starting from incomplete hydrocarbon combustion, condensed-phase materials are formed. These materials are produced mainly in fuel-rich flames, characterised by a flame equivalent ratio ( $\Phi$ ), i.e., the fuel-to-oxidiser ratio to the stoichiometric fuel-to-oxidiser ratio, higher than one.

Soot, as already said, is a severe and increasing threat to human health and the environment. Soot particles, particularly at the nanoscale level, can be easily trapped and accumulated in the human body, causing critical and adverse health effects (Oberdörster *et al.*, 2004; Kennedy, 2007; Bond *et al.*, 2013; Pedata *et al.*, 2015; Bhandari *et al.*, 2019). Furthermore, emitted soot particles represent one of the most substantial sources of anthropogenic radiative forcers, possibly second only to CO<sub>2</sub> (Bond *et al.*, 2013)—these issues motivated past and current interest in understanding the mechanism behind soot formation in combustion. The formation of soot particles in flames results from a series of complex chemical and physical processes occurring in a short time scale (of the order of few milliseconds) and a highly reactive environment.

The process which leads to the particle formation in flame has been studied and theorized for decades even though an in-depth and complete knowledge of all mechanism involved is not achieved yet (Andrea D'Anna, 2009; Hai Wang, 2011). In order to overcome this difficulty, the combustion community has extended the attention to multidisciplinary fields involving molecular dynamic (Schuetz and Frenklach, 2002; Herdman and Miller, 2008; Iavarone *et al.*, 2017; Mao, van Duin and Luo, 2017), ab initio calculation (Kubicki, 2006; Rossi, 2008; Semenikhin *et al.*, 2020), mass spectrometry (Happold, Grotheer and Aigner, 2007; Faccinnetto *et al.*, 2011; Grotheer, Wolf and Hoffmann, 2011; Irimiea *et al.*, 2019), spectroscopy



measurements (Sadezky *et al.*, 2005; Alfè *et al.*, 2007; De Falco *et al.*, 2017), resonance technique such as electron paramagnetic (Jones *et al.*, 2004; Wang *et al.*, 2009; Herring *et al.*, 2013) and nuclear magnetic resonance spectroscopy (Santamaria *et al.*, 2010; Salamanca *et al.*, 2012a; Wiedemeier *et al.*, 2015; Savy *et al.*, 2017), the use of microscopy (Liu and Li, 2006; Cain *et al.*, 2014; Minutolo *et al.*, 2014).

Figure 3.7 shows a picture of the mechanisms of carbonaceous particle formation in the flame.

Soot formation is a complex physicochemical process that could be divided into some significant processes (Andrea D'Anna, 2009; Frenklach, 2002a; Hai Wang, 2011):

1. gas-phase reactions;
2. particle nucleation ;
3. particle coalescence surface growth ;
4. particle coagulation;
5. particle oxidation ;

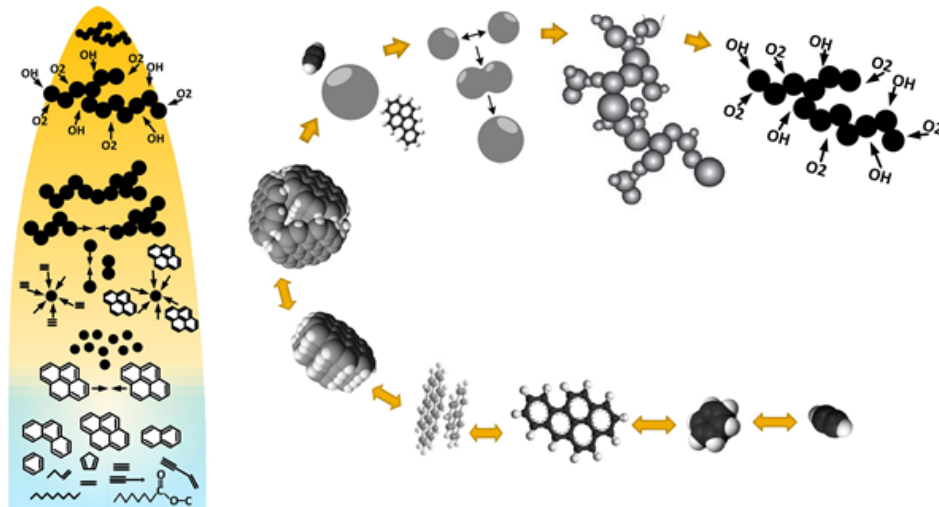


Figure 3.7 Detailed and Fundamental Modeling of Soot Formation,  
<https://thomsonlab.mie.utoronto.ca/detailed-and-fundamental-modeling-of-soot-formation/>

The formation process starts with gas-phase pyrolysis and the oxidation of fuel. In fuel-rich flames, the incomplete oxidation of fuel molecules results in gas-phase products close to the flame front, which later recombines, forming benzene,

naphthalene, and other larger polycyclic aromatic hydrocarbons (PAHs). To describe the soot formation process, it is fundamental to understand the structure of the PAH compounds acting as building blocks of the soot particles and as precursor molecules of nanoparticle formation and growth (Sirignano, Kent, and D'Anna 2010; Henning Richter et al. 2005). Indeed, once formed, these aromatic structures begin to assemble into just-nucleated particles or incipient soot, whose size is usually of the order of few nanometers, i.e., 2-3 nm (Commodo *et al.*, 2018), through a gas-to-solid nucleation mechanism.. The transition from the gas phase PAHs to compounds that present a condensed-phase behaviour is called the inception or nucleation mechanism. Nowadays, this step remains unclear yet, and its understanding would represent a remarkable breakthrough. Once formed, incipient soot undergoes size growth via coagulation/coalescence processes and surface chemical reactions with gas-phase molecules and eventually carbonisation and oxidation. This next step results in the formation of larger particles, with a mean size that shifts from about 4-10 nm to 10-100 nm and more, depending on the flame equivalence ratio and the flame residence time increase (Commodo, De Falco, *et al.*, 2015).

The following is a brief account of the main processes of the mechanism.

### 3.2.1 GAS PHASE-REACTIONS

The first aromatic ring, such as the benzene, is formed from molecules and radicals resulting from the decomposition/pyrolysis of the fuel. The first hypothesis involved acetylene  $C_2H_2$ , the most abundant hydrocarbon intermediate and the most prominent growth species, due to its thermal stability and abundance. In the reaction, acetylene reacts with an  $H^\bullet$  radical that gives rise to chain reactions, like all radical species. This mechanism idea comes from Frenklach and Wang, who first used the acronym HACA (H-abstraction- $C_2H_2$ -addition) back in 1991 (Frenklach and Wang, 1991). Then with the formation of the first aromatic ring, the activation of an aromatic site can be not just by H abstraction but also by H addition (Frenklach, Schuetz and Ping, 2005), and in this way, an increase of the molecular weight happens. This increase occurs because of the creation of a free radical site on a PAH through the abstraction of H-atoms from the aromatic ring using an external H-atom ( $A_i + H \rightarrow A_i^\bullet + H_2$ ), which is followed by the

addition of  $C_2H_2$  on the radical site and the ring closure ( $A_i + C_2H_2 \rightarrow \text{Products}$ ). However, HACA can be more generally thought of as an acronym for H-Activated-Carbon-Addition featuring the underlying kinetic– thermodynamic coupling, where "H-Activated" implies "H-Abstraction", "H-Addition", or even "H-migration" (Frenklach and Mebel, 2020).

Thus, the other vital factor to consider is the radical species, namely compounds characterised by at least an unpaired electron. Generally, the "activation" process could start from H or OH radical species, very abundant in flame conditions, but other gas species could initiate the radical propagation.

The presence PAH radicals immediately links to a radical stabilization by resonance; indeed, the unpaired electrons are delocalised on the aromatic structure. The other route to form multi-rings species involves resonantly stabilised radicals (RSRs) which consist of multiple reactive sites and undergo self-recombination reactions or reactions with other RSRs coupled with dehydrogenation and aromatisation. They play an essential role in the molecular-weight growth chemistry in combustion (A. D'Anna *et al.*, 2000; Gomez *et al.*, 1984; D.-H. Kim *et al.*, 2007; Lamprecht *et al.*, 2000; Lu & Mulholland, 2001; Matsugi & Miyoshi, 2012; A. Violi *et al.*, 2001). Some common RSRs, recognised for their roles in the aromatic formation, are propargyl ( $C_3H_3$ ), allyl ( $C_3H_5$ ), cyclopentadienyl ( $C_5H_5$ ), benzyl ( $C_6H_5CH_2$ ), and indenyl ( $C_9H_7$ ). Propargyl recombination seemed to contribute significantly to benzene formation in flames (Tang, S. Tranter and Brezinsky, 2006; Hansen *et al.*, 2011).

Recently, high-resolution atomic force microscopy (HR-AFM) provided an accurate image of PAHs radicals (Schulz *et al.*, 2019) that, together with their revelation by photoionisation mass spectrometry (Johansson *et al.*, 2018), give experimental evidence of radical existence in flame.

However, the radicals can be distinguished in  $\sigma$  or  $\pi$  radicals that have a different implication in the growth process and are discussed in the next paragraph.

### 3.2.2 PARTICLE NUCLEATION

There is a consensus in the scientific community about the crucial role that polycyclic aromatic hydrocarbons (PAHs) play as precursors in soot nucleation and growth.

PAHs are ubiquitous by-products of fuel-rich flames that survive from fragmentation at high temperature due to the high stability of the six-membered benzenoid rings (Haynes and Wagner, 1981; Harris and Weiner, 1985; Stein and Fahr, 1985; Richter and Howard, 2000; Frenklach, Schuetz and Ping, 2005; Wang, 2011). The most stable individual molecules are organised in peri-condensed systems; examples are naphthalene, , pyrene, coronene, and even larger peri-condensed aromatics.

During molecular growth, PAHs can form clusters of two or more units, generating condensed-phase incipient particles, but the process involved in this crucial step is still unresolved. The units are comprised of aromatic structures in turbostratic stacks, with approximately 3–4 PAH in a stack, stabilised by intermolecular interactions. Then, the stacks coalesce into roughly spherical primary particles of about 10–30 nm diameter. Subsequently, these primary particles aggregate to form fractal-like structure of soot with a typical size between 200 and 300 nm. Generally, nucleation is associated with pure van der Waals interactions among mostly condensed aromatics (A. D'Anna *et al.*, 2001; Andrea D'Anna, 2009; Frenklach & Wang, 1991; Howard, 1991; Schuetz & Frenklach, 2002), where the binding energies involved in cluster formation depend on the size of the aromatic molecules, i.e., the number of fused benzenoid rings per molecule (Herdman and Miller, 2008; Chung and Violi, 2011). This physical route is responsible for the attraction of instantaneous or permanent dipoles present in the molecules.

In the PAH molecules, the  $\pi$ -electron cloud extends above and below the molecular plane by the condensed aromatic rings, creating a sizeable electronic structure in which there is a strong interaction between the planes, thus forming a stacked structure. Out of plane interactions of gas-phase, PAHs and their stacking are the critical step for forming three-dimensional structures (Frenklach and Wang, 1991, 1994; Miller, 1991). The PAHs considered through the years for this process ranged from a molecule with more than seven rings to very small PAHs like naphthalene. Other recent studies have concluded that inception begins with a ten-ring or 16-ring PAH (Botero *et al.*, 2016, 2019; Adkins, Giaccai and Miller, 2017).

Initially, there was a strong belief about the vital role of pyrene in nucleation. Frenklach and co-investigators first proposed that dimerisation of PAHs as small as pyrene was necessary to correctly reproduce soot particle size distributions (Frenklach and Wang, 1991, 1994). Miller and co-workers (Miller, 1991; Herdman and Miller, 2008) also tested the importance of PAH dimerisation in the

soot nucleation process. Initially, Miller et al. precluded the possibility of PAH dimerisation as the start of soot nucleation (Houston Miller, Smyth and Mallard, 1985). Then, they revisited the concept from a kinetic perspective, and they concluded that the process could occur when the PAH size is four times larger than pyrene (Miller, 1991). However, Schuetz and Frenklach (Schuetz and Frenklach, 2002) re-emphasised the role of pyrene by investigating the collision of two pyrene molecules using semi-empirical molecular dynamics method.

Recent theoretical studies indicate that pyrene dimerisation might not be an essential step in the soot formation process. For example, Chung and Violi (Chung and Violi, 2011) observed pyrene dimers or trimers using molecular dynamics simulations and concluded that they are not stable enough to grow into soot nuclei at soot generating temperature conditions. Kraft and co-workers (Totton, Misquitta and Kraft, 2012) studied the physical nucleation of several PAHs using simulations, concluding that in low-temperature regions of the flame (500 K–1000 K), physical nucleation may still be a competitive route for particle inception and growth for molecules larger than pyrene and the only circumcoronene was found to dimerise at 1500 K (Totton, Misquitta and Kraft, 2011).

In a recent work, Kholghy et al studied the importance of reactive PAHs dimerization as driver of soot nucleation (Kholghy, Kelesidis and Pratsinis, 2018). In the study, the evaluated mechanism was based on the reversibility of nucleation in which: chemical bond formation reactions do not require H atoms to proceed; a fully reversible dimerization as the first step in PAH reaction for soot nucleation was considered; and chemical bond formation after reversible dimerization also was taken in account (Kholghy, Kelesidis and Pratsinis, 2018).

Thus, they concluded that soot nucleation must involve strong chemical bond formation between dimers. Thus, initially unstable dimers are formed through reversible dimerization and then covalent bonds are formed. The species involved in this mechanism were especially the very abundant small PAHs that forming dimers could serve as soot nuclei (Kholghy, Kelesidis and Pratsinis, 2018).

However, in addition to this issue, that is the size of PAHs to start with cluster formation, it is mandatory to understand the exact physical forces involved. Indeed, purely van der Waals interactions do not provide a universal or consistent explanation for the soot nucleation processes observed under different flame conditions. Detailed knowledge of this transformation is crucial for understanding soot formation in combustion systems. Besides, more profound knowledge of the mechanism of cluster formation is required to control structural transformations affecting the order/disorder degree of flame-generated engineered carbonaceous

particles, and thus their magnetic and conductive properties, which are of interest for optoelectronic applications (Kusakabe and Maruyama, 2003; Li *et al.*, 2016; Mulay *et al.*, 2019).

In this regard, radical sites at PAH edges play a crucial role in forming condensed species. This concept dates back to the 1980s and the work done in Gottingen and Darmstadt by Wagner's and Homann's groups and at MIT by Howard's group (Homann and Wagner, 1967; Wagner, 1979; Howard, 1991; Keller, Kovacs and Homann, 2000). Later, in a series of contributions, D'Anna and co-workers proposed a soot nucleation mechanism based on the formation of cross-linked three-dimensional high-molecular-mass structures via chemical pathways involving propagation and termination of aryl and resonantly stabilised radicals (RSRs) (A. D'Anna *et al.*, 2001; Andrea D'Anna, 2009; Andrea D'Anna *et al.*, 2010; Sirignano *et al.*, 2010). Notably, it was suggested that the generation and propagation of RSRs begin with adding an aryl radical to the double bond 9,10 in phenanthrene and five-membered-ring PAHs (A. D'Anna *et al.*, 2001). These double bonds in phenanthrene and five-membered-ring PAHs can be easily broken, forming intermediate species in which electrons can migrate over the entire structure and continue the addition sequence, forming higher-molecular-mass species without encountering a barrier (Violi, Sarofim and Truong, 2001). The difficulty in explaining the rapid clustering to form carbon solids in flame has attracted renewed interest in clustering/reaction pathways involving radicals.

In addition to the purely benzenoid PAHs, five-member rings are also present, and they seem to have a controlling role in the formation and growth of aromatic. Acenaphthylene-type rings, i.e., acenaphthylene and cyclopenta(cd)pyrene, are formed in flames due to their high stability, as predicted by Fahr and Stein (Stein and Fahr, 1985). This type of pentagonal ring can be rapidly formed by hydrogen abstraction followed by acetylene ( $C_2H_2$ ) addition on a zig-zag edge of an aromatic structure as computationally observed by Frenklach and co-workers in a series of earlier investigations (Frenklach *et al.*, 1985; Frenklach, Schuetz and Ping, 2005; Whitesides and Frenklach, 2010). In a combined experimental and computational study, Johansson *et al.* (Johansson *et al.*, 2017) suggested a relevant contribution of five-membered rings for the soot precursor structures, as opposed to only six-membered rings. However, only the recent use of high-resolution atomic force microscopy (HR-AFM) succeeded in providing a definitive assessment of the contribution and type of pentagonal rings in the incipient soot molecules (Commodo *et al.*, 2019; Schulz *et al.*, 2019). Other than acenaphthylene-type rings, a large variety of cross-linked bi-phenyl-, fluorene- and fluoranthene-like

PAHs have also been detected at the soot inception in laminar premixed flame. Notably, a remarkable number of PAHs containing pentagonal rings or even six-membered rings with methylene groups ( $-\text{CH}_2-$ ) were also detected (Commodo *et al.*, 2019; Schulz *et al.*, 2019).

The presence of groups, such as  $\text{CH}_2$  in a saturated ring or a  $\text{CH}$  in an unsaturated one or even a  $\text{CH}_3$  in an aliphatic chain, is fundamental in explaining how different radicals could be formed and their different roles in the inception step. Radicals can be classified as  $\pi$  or  $\sigma$ , according to whether the spin-bearing orbital is of the p or s type. Orbitals of s type are defined as symmetric and p orbitals as antisymmetric to the molecular plane that is also the  $\pi$  system nodal plane.  $\pi$ -radicals, in particular those with a comprehensive  $\pi$  system, are thermodynamically more stable than  $\sigma$  ones. However, more relevant to lifetime of radicals than their thermodynamic stability is their kinetic stability (or persistence). Persistent radicals (Griller and Ingold, 1976) are often sterically protected so that dimerization and other reactions are impeded. The formation of neutral radicals involves, in principle, homolytic cleavage of a covalent bond. A C-H or C-C bond must be broken to produce a hydrocarbon radical. This scission requires dissociation energy of 300 to 400 kJ/mol unless the bond is weakened by steric strain (Rüchardt and Beckhaus, 1980).

Because of their low stability and high reactivity,  $\sigma$  radicals are less easy to detect.

In the nucleation, H atom abstraction to  $-\text{CH}_2-$  of the partially protonated rim-based pentagonal rings or H atom addition to acenaphthylene-type cyclopentadienyl rings form delocalized  $\pi$  radicals. Indeed, if an H atom is removed from the aromatic molecule composed of purely benzenoid rings, the unpaired electron occupies an orbital lying in the local molecular framework plane, forming a  $\sigma$  radical. Conversely, supposing that an H atom is removed from an  $\text{sp}^3$  hybridized carbon at the periphery of an aromatic molecule, such as a  $-\text{CH}_2-$  group in a five-membered or six-membered ring in a PAH, or that an H atom is added to an unsaturated ring, in that case, the unpaired electron occupies an orbital perpendicular to the local molecular framework, thus forming a  $\pi$  radical which delocalize over the entire molecule (Howard, 1991).

Unpaired electrons in orbitals lying in the plane ( $\sigma$  radicals) cannot be delocalized on the aromatic system: it is the case of phenyl radicals. These  $\sigma$  radicals undergo sequential reactions of acetylene addition, leading to bigger aromatics (Frenklach *et al.*, 1985). The self-combination of these types of radicals

forms bi-phenyl-like, cross-linked compounds (A. D'Anna et al., 2001). An unpaired electron located in an orbital perpendicular to the plane,  $\pi$  radical, can be delocalized through the entire molecule and stabilized by resonance. Besides, to be critical about the formation of the first aromatic ring (Miller and Melius, 1992), the resonantly stabilized  $\pi$  radicals have long been considered essential species in promoting soot nucleation and growth (Homann and Wagner, 1967; Keller, Kovacs and Homann, 2000).

On the base of this new experimental evidences (Johansson *et al.*, 2018; Commodo *et al.*, 2019; Schulz *et al.*, 2019), it has been speculated that resonantly stabilized  $\pi$  radicals, mainly due to partially protonated rim-based pentagonal rings, might be involved in the nucleation/ clustering of aromatics. These radicals promote bridging reactions (Frenklach & Mebel, 2020; J. W. Martin et al., 2019), leading to three-dimensional carbon structures. The role of resonantly stabilized radicals in aromatic growth and soot inception was already hypothesized by D'Anna et al. (A. D'Anna et al., 2000). Aromatic radicals are known to play a fundamental role in numerous branches of organic chemistry; one of the most investigated aromatic  $\pi$  radical compound, the phenalenyl radical, has been found to form a  $\pi$ -stacking intermolecular attraction, sometimes referred to as "pancake bond" or "multi-electron/multi-centre (me/mc)" consisting on an unusual delocalized covalent-like bond (Mou *et al.*, 2014; Gao *et al.*, 2016; Kertesz, 2019). This compound's particularity is the rapid interchange between a covalent bond formation and this pancake bond interaction. Recent literature, especially by DFT calculation, investigates the role of this unconventional stacking which is a half pure covalent bond and half pure van der Waal, in the inception step. The trial is to understand whether soot's growth may start from a combination of physical interaction and covalent bonding. The goal should be to understand how different levels of localization or delocalization of radicals on PAHs compound more or less aromatic influence the dimer and so the stacking formation in soot nucleation (Martin *et al.*, 2019; Gentile *et al.*, 2020).

### 3.2.3 SURFACE GROWTH AND PARTICLE COAGULATION

Once the first species pass to condensed status, the formation process continues by surface growth, namely a mass addition.



The addition involves not only acetylene, but aromatic particles also contribute to the growth by aromatization. Depending on the compound mainly responsible, structures linked by an aliphatic chain or larger aromatic islands are formed in this phase. Therefore, these two kinds of surface growth lead to the final form and amount of particles, even though by two different routes (Andrea D'Anna, 2009). The particles assume a spherical-like stacked configuration.

However, both reactions involve molecular species and particles with the active site, namely with radicals. The formation of radicals on a surface is the limiting step for surface growth because as the reaction progresses, the reactive sites for the formation of radicals decrease since hydrogen atoms decrease, and the radicals tend to quench each other.

A better knowledge of the radical sites on the reacting surface is a fundamental parameter to estimate the growth rate of particles. From this perspective, molecular growth depends on the ageing process occurring on the surface (Blanquart and Pitsch, 2009; Sirignano, Kent and D'Anna, 2010). Indeed, a factor that could drive the formation of the active site is the high temperature.

Going on in the flame, the primary soot particles coagulate. Coagulation processes control the numerical concentration of soot particles, the size and the final morphology (Smoluchowski, 1916).

This process is strongly controlled by physical characteristics of soot particles and combustion conditions, responsible for the nature of particles, which control the inception process, indirectly affecting the coagulation rate and, thus, the surface growth (D'Alessio et al., 2005).

It is possible to classify two different coagulation ways: coalescent coagulation and aggregating coagulation.

In coalescent coagulation, tiny particles or condensed species act like small droplets and tend to form a larger particle for a collision. In this case, van der Waals forces are responsible for the species' attraction and the formation of intra- and intermolecular bonds. Moreover, coagulation leads to a bimodal distribution in particle formation during combustion (Zhao *et al.*, 2003; Sgro *et al.*, 2007).

The sticking coefficient measured for small nanoparticles is temperature-dependent, and in the flame, conditions can be up to three orders of magnitude smaller than at room temperature. This very low sticking efficiency makes these nanoparticles a not negligible intermediate state from the gas phase to large particles. They survive along the flame reactor and can be emitted (Minutolo *et al.*, 2008).

### 3.2.4 OXIDATION

For the last step of the mechanism, that is the oxidation, a specification must be done. Two kinds of oxidations processes exist, gas-phase oxidation and catalytic oxidation. The latter is widely diffused in the after-treatment system, e.g. in engine particulate filter stages, due to the possibility to reduce emissions of the largest particle formed in combustion (Seipenbusch *et al.*, 2005; Choi and Foster, 2006; Messerer, Niessner and Pöschl, 2006).

Gas-phase non-catalytic oxidation has been studied, on the contrary, as a limiting stage during soot formation. The influence on the total amount of soot produced depends on the soot's oxidation resistance and the combustion environment's capability to give place to the oxidation process. The first problem is linked with the characteristic of the particles produced and the possible points of attack by oxidant species (Vander Wal and Tomasek, 2003). Molecular oxygen,  $O_2$ , and hydroxyl radical,  $OH\bullet$ , are the combustion environment's main oxidant species. Molecular oxygen is more present in a lean flame than a rich one. Conversely,  $OH\bullet$  is present in almost all combustion conditions.

The oxidation process is always active and intimately linked with the growth process, making the correct evaluation of the growth process even harder. An underestimation in the oxidation process can easily lead to an overestimation of the total soot amount.

Different experimental and numerical studies have been performed to study the oxidation process. However, since the first studies on the oxidation process, two oxidation steps were individuated: surface oxidation and oxidation-induced fragmentation (Echavarria *et al.*, 2011).

Surface oxidation is when oxidizing species from the gas phase (predominantly hydroxyl radicals and molecular oxygen) react with soot particles' surface, removing carbon. This process is always active and is due to all oxidant species.

### 3.3 DOPED FLAMES

As previously written, flame synthesis is one of the most profitable methods to obtain nanoparticles. Whether they are carbon nanoparticles or inorganic nanoparticles such as  $\text{TiO}_2$ ,  $\text{SiO}_2$ ,  $\text{Al}_2\text{O}_3$ , the general path that leads to their formation consists of the same steps, i.e. a gas phase followed by nucleation with mass and surface growth. Then, through agglomeration and coalescence, the clusters thus formed provide the "final product". To obtain nanoparticles of different natures or entity, it needs to act on the precursors used as a dopant in the hydrocarbon fuel. The state of the precursor can also affect the characteristics of the final product. Three methods exist to add a precursor in flame (Strobel and Pratsinis, 2007):

- Vapour-fed aerosol flame synthesis (VAFS), a volatile precursor is burned in a hydrocarbon flame;
- Liquid-fed aerosol flame synthesis (LAFS), a method for non-volatile precursors in which a liquid, an emulsion or slurry, is sprayed and converted into the final product.
- The flame spray pyrolysis process (FSP), a liquid-phase mixture containing a metallorganic compound and a solvent, is dispersed into a flame where the resulting mixture droplets are combusted, generating small clusters. A relatively small pilot flame is used as such a source to ignite and sustain spray combustion.

Several nanoparticles in different states, such as powder, solid, films, are produced through these combustion approaches.

For example, to detect and investigate the nitrogen chemistry in flame, using a suitable precursor as a dopant is a practice always more diffuse.

Indeed, nitrogen leads to  $\text{NO}_x$  formation representing another combustion field issue because  $\text{NO}_x$  are considered one of the main air-polluting chemical compounds. In all combustion systems, there are three ways to form  $\text{NO}_x$ . A given molar concentration of nitrogen and oxygen at a specific temperature leads to  $\text{NO}_x$  formation; if the combustion temperature is below  $1300^\circ\text{C}$  smaller concentrations of thermal  $\text{NO}_x$  are formed. Then, some fuels contain nitrogen (e.g., coal) and in this way are made "fuel  $\text{NO}_x$ " that results from oxidation of the already-ionized nitrogen contained in the fuel (Environmental Protection Agency (EPA), 1999). Another kind of  $\text{NO}_x$  is formed by molecular nitrogen in the air combining with fuel in fuel-rich conditions. This nitrogen then oxidizes along with the fuel and

becomes NO<sub>x</sub> during combustion (Environmental Protection Agency (EPA), 1999).

Researchers use a doped flame in different pressure, temperature profile, and flame conditions (lean, rich, or stoichiometric).

For instance, Shmakov et al. studied the formation and consumption of NO in lean, near-stoichiometric, and rich H<sub>2</sub> + O<sub>2</sub> + N<sub>2</sub> flames doped with 0.03–0.1% of NO or NH<sub>3</sub> using molecular-beam mass-spectrometry (Shmakov *et al.*, 2010).

Again, the valuation of NO<sub>x</sub> formation in the flame is also detected with a CH<sub>4</sub>+O<sub>2</sub>+N<sub>2</sub> flame by always using NH<sub>3</sub> as dopant with previous model work (Konnov, Dyakov and De Ruyck, 2006).

In the past, the use of dopant in the pure hydrocarbon fuel was also practical to better understand the process of soot formation, with a clear comprehension of radical and non-radical species that formed in the nucleation and giving in this way an outstanding contribution to computer modelling (McEnally and Pfefferle, 1998).

Due to the depletion of fossil fuels, more and more attention has been given to biofuels, including a blending of pure fuel with alcohols, ethers, and esters considered one of the best alternatives to petroleum-based transportation fuels. The scientific community's expectation on biofuels is mainly focused on the possibility to reduce the production of environmental pollutants, clean the air, avoid all disasters, both human and ecological, which in recent years have been increasingly in the news.

With this purpose, a significant section of the combustion community has been studying biofuels to have the opportunity to investigate their nature, but above all, the consequences they could have. Indeed, very often, using these fuels does not make it safe to be free from polluting by-products. In various studies, it has been discovered that using these alternative fuels to reduce the production of a pollutant leads to the introduction into the atmosphere of other types of harmful products. Biofuels' production must be carefully studied as it must be subject to low costs to become more convenient and attractive. Many factors need to be considered to assert with absolute certainty that it's worth the hassle, i.e. that the use of biofuels can give rise to an era in which coal and petroleum will not be needed.

Studies and ad-hoc considerations have been made on the different biofuels, on their combustion chemistry, on the differences with pure hydrocarbon fuels. It is also mandatory to consider these alternative fuels' compatibility and fuel additives compatibility with current fuel-delivery infrastructure and engine performance.

An example of replacement or alternative to conventional hydrocarbon fuels are the oxygenates one that must be critically examined from different practical viewpoints such as availability and production costs, the energy content but also and especially the chemistry aspect and composition of the fuels (Agarwal, 2007; Chen, Shuai and Wang, 2007; Demirbas, 2007; Lapuerta, Armas and Rodríguez-Fernández, 2008; Bolszo and McDonell, 2009; Fang and Lee, 2009; Klein-Douwel *et al.*, 2009). What is studied very carefully is the influence of all these characteristics on the emissions of pollutants. For example, it has been studied that particulate emission can be reduced by adding ethanol (Chen, Shuai and Wang, 2007). Nevertheless, undesired aldehyde emissions may then increase significantly (Agarwal, 2007). Also, increased NO<sub>x</sub> emissions have been observed from biodiesel combustion (Fang and Lee, 2009). Several variants of oxygenated fuels are currently available from starch, sugar, or oil crops, including bio-alcohols and biodiesel.

However, the scientific community's primary interest remains to reduce the pollutant emission as CO<sub>2</sub> and NO<sub>x</sub>. The current policy uses mixtures of fossil and biogenic fuels to replace the neat hydrocarbon fuels without any changes in the respective combustion engine. Indeed, the oxygenates additives could improve the combustions, leading to an early formation of radical species (Chen *et al.*, 2007; Huang *et al.*, 2009). Interactions of the reactive intermediates from all fuel blends components may affect combustion emissions (Pang *et al.*, 2008; Piperel, Dagaut and Montagne, 2009).

For example, oxygenate addition leads to increased levels of C<sub>3</sub>H<sub>3</sub>, a major benzene precursor, by the combination of CH<sub>3</sub> and C<sub>2</sub>H<sub>x</sub> species. The oxygenate additives could affect soot and pollutant formation, depending on flame configuration, such as a premixed and non-premixed flame (Song *et al.*, 2003; McEnally and Pfefferle, 2007; Bennett *et al.*, 2009).

However, detailed models are required to study general decomposition and oxidation behaviour for some oxygenate fuels and fuel blends and to be able to attribute the correct influence on some pivotal reactions. Therefore, typical biofuel families include alcohols, ethers, esters, and some nitrogenated chemicals. Clearly, to understand intermediates and products formed, including pollutants, it is necessary to know or have a general comprehension of the involved chemical reaction and particularly to know the fuel molecule's innate chemical structure. Typical biofuels can produce PAHs and soot, like conventional hydrocarbon fuels. These emissions may be reduced concerning pure hydrocarbon molecules of similar size. This benefit is often paid for with the increased formation of carbonyl

compounds, including formaldehyde, acetaldehyde, acetone, and higher aldehydes and ketones

Moreover, since aromatic compounds are the first species to be formed in hydrocarbon combustion chemistry, it can be very advantageous to extend this kind of study using fuels mixed with aromatic compounds, such as benzene, toluene, and other similar substance. Therefore, these fuels, containing directly aromatic additives, have been analysed and used in the laboratories to replicate usual pure fuels. This approach leads to a better understanding of their combustion and a significant possibility of reducing pollutant emissions (Simmie, 2003; Eddings *et al.*, 2005; Battin-Leclerc, 2008). As previously said, the molecular fuel structure is crucial for the formation of PAHs and soot (Andrea D'Anna, 2009; H. Richter & Howard, 2000), responsible for the environmental pollution, above all. Thus, the approach to use an aromatic compound as an additive to fuel allows a detailed investigation of the role of aromatics in soot and PAHs production. The most used aromatic additive is benzene, the first aromatic ring generated in the combustion process. Indeed, in this work, the benzene has been chosen to make an investigative and comparative study. The behaviour of flame doped with benzene is quite different from that of pure hydrocarbon one. First, aromatic addition leads to some changes in the combustion conditions such as fuel velocity, temperature, and above all, the sooting tendency.

Indeed, whereas in aliphatic flames, there is a slow conversion of the aliphatic molecule to aromatic compounds, in aromatic flames, the aromatics are already present in the flame front zone, inducing the early formation of first particles.

Also, for benzene flames, the processes of fuel oxidation and pyrolysis overlap: particle inception occurs in the primary oxidation region, in a flame environment utterly different to that encountered in the ethylene flame where particles nucleate in the post-oxidation region of the flame (D'Alessio *et al.*, 1992; Andrea D'Anna & Violi, 2005; Haynes *et al.*, 1980). Since these observations, precursor nanoparticles' transformation to soot may be controlled by different processes concerning aliphatic flames, and kinetic aspects could be more relevant than physical coagulation of the precursor nanoparticles.

The benzene's importance arises from the fact that the first aromatic ring formation is the kinetic controlling step during soot formation (Homann and Wagner, 1967; Frenklach, 2002b; Violi, 2004; Alfè *et al.*, 2007).

The fuel chemical structure and the reaction environment result to influence also radical formation. It is the case of aromatic hydrocarbons, which during oxidation form resonantly stabilised  $\pi$ -radicals, e.g., cyclopentadienyl, benzyl, or

indenyl radicals, depending on the aromatic molecules involved in the oxidation process. The formation of such radicals promotes molecular growth, and for this reason, soot formation in aromatic fuel flames occurs across the flame front in an environment still rich in oxidising species. The different propensity of aromatic fuels in forming resonantly stabilised radicals already at the flame front and understanding the role of radicals in the formation of nascent particles are additional motivations of this thesis work.

## CHAPTER 4: EXPERIMENTAL SET-UP, METHODS AND DIAGNOSTICS

### 4.1 PREMIXED LAMINAR FLAME REACTOR

The synthesis of carbonaceous nanoparticles was performed using a premixed laminar flame at atmospheric pressure, generated on a commercial burner, as a reactor. In this configuration, fuel and oxidant are mixed before the flame front, where they react together. This system represents an accessible combustion apparatus allowing to follow the combustion process, temperature, and species concentration, as a function of only one variable: the distance from the burner, or equally as a function of the residence time in the flame. Indeed, a premixed flame is a one-dimensional reactor, considered as a plug flow reactor.

The burner used in this thesis work is a McKenna type, producing flat and high-stable flames, with a porous plug of 60 mm in diameter and a forced water circulation cooling system, allowing to stabilize flames with several cold gas velocities and equivalence ratios. The flame is stabilized by a plate, positioned at about 40 mm above the burner. Figure 4.1 shows some pictures of the McKenna burner.

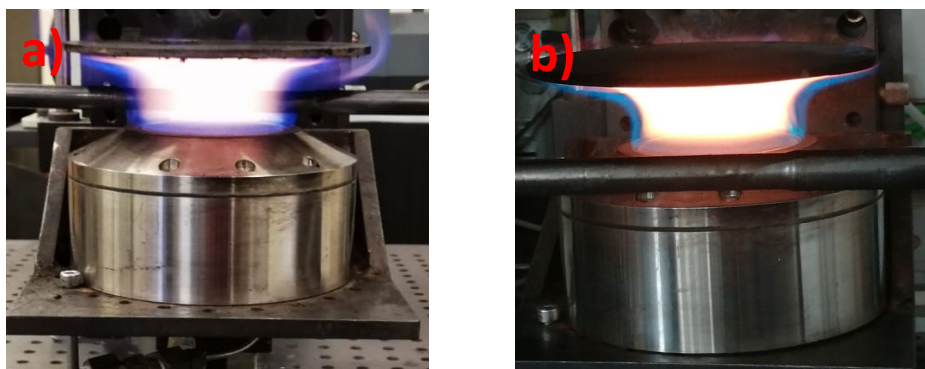


*Figure 4.1 Some pictures of McKenna Burner with experimental flame: a-b)  
Premixed ethylene-air flame*

First, carbon nanoparticle synthesis was performed by operating with a premixed ethylene air flame with a cold gas velocity equal to 9.8 cm/s (NTP) and a carbon-to-oxygen atomic ratio (C/O) set to 0.67, corresponding to a flame equivalence ratio ( $\Phi$ ) of 2.01.



These carbon nanoparticles were compared with those produced in a subsequently comparative study with benzene, used as a dopant to the flame. During the comparative study, two flames were investigated, a laminar premixed pure ethylene flame and the same flame in which 30% of ethylene carbon was replaced by benzene. The two flames were identical, i.e., the same equivalence ratio, temperature, and unburned gas velocity. Each flame was split into two set: the first with an equivalence ratio,  $\Phi$ , fixed at 1.89 and a C/O ratio equal to 0.63; the second flame set with a  $\Phi$  fixed at 2.01 and a C/O ratio equal to 0.67. The gas velocity and equivalence ratio are kept constant with the only difference in the gas temperature. Indeed, to avoid the benzene condensation and assure equal inlet conditions, the gases were pre-heated to 100 °C.

The flames temperature was measured by an R-type thermocouple (Pt/Pt-13% Rh) with a spherical junction with a diameter of 300  $\mu\text{m}$  using a rapid insertion procedure as described in a previous work by (De Falco *et al.*, 2017).

The flame operation was performed with gases supplied by Brooks mass flow controllers.

## 4.2 SAMPLING METHODS

The production of flame carbon nanoparticles was performed using a horizontal tubular probe with a downward orifice positioned at the flame's sampling point. The probe is made of stainless steel with a 1 cm outer diameter and an orifice with a thickness of 0.5 cm. The orifice diameter is of different measure depending on the experimental analysis. A diameter of 0.2 mm was used for particle size distribution analysis; probes with a diameter of 0.3mm, 0.6 mm and 2.5 mm were often used to collect particles on filters for off-line characterizations. In each sampling, the probe underwent rapid clogging, and had to be mechanically cleaned. The sampled flow entering the probe was mixed to a turbulent N<sub>2</sub> diluent flow, reaching a dilution ratio on the order of 1:3000. The nitrogen flow rate and the sampling procedure were optimized to prevent particle aggregation and to quench chemical reactions, thus preventing particle mass growth within the sampling line.

The particles were collected on filters (Whatman QM-A Quartz Microfiber Filters, 47 mm and 25 mm; Fluoropore<sup>TM</sup> PFTE Membrane Filter, showed in Figure 4.2) positioned in a filter holder.

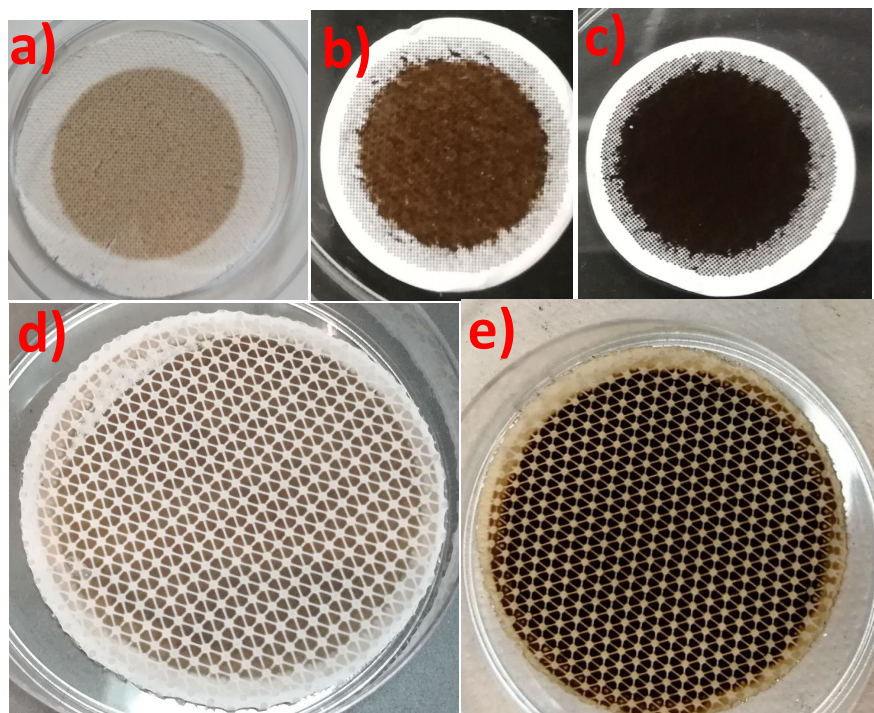


*Figure 4.2 Picture of some sampled filters. a)-c) Quartz filters; d)-e) Teflon Filters*

Several samplings were performed collecting the particle to different residence times, i.e. different height above the burner, HAB, to study particles' evolution in the flame. The amount of sampled materials depended on the under-pressure created in the probe; in these samplings, the value was fixed approximatively to -60 mm H<sub>2</sub>O.

Figure 4.3 shows a schematic of the sampling apparatus.

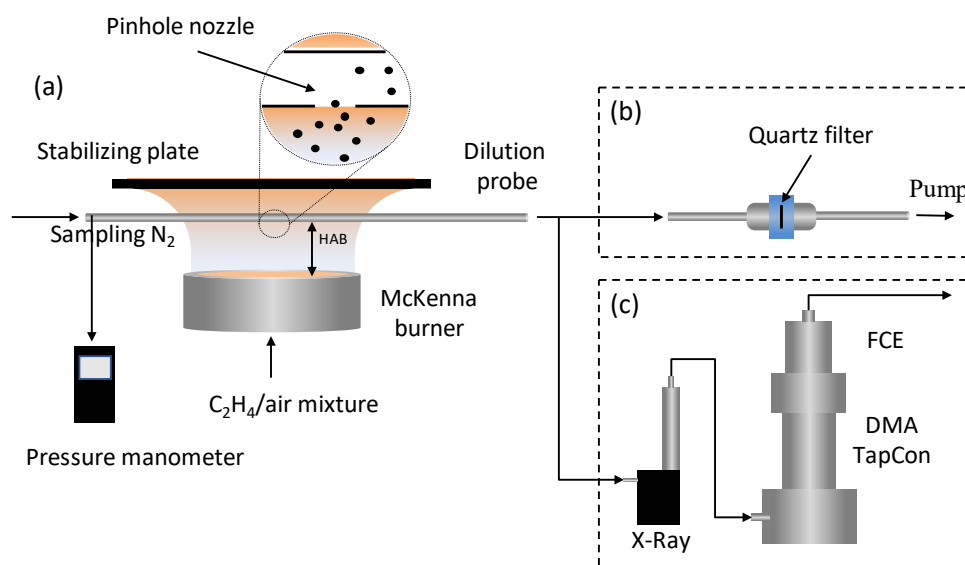


Figure 4.3 Experimental set-up. a) McKenna burner generates a premixed laminar ethylene-air flame stabilized by a plate. The Carbon nanoparticles are introduced by a small orifice of the dilution probe and diluted by using  $N_2$ . A manometer regulates the pressure. b) the Particles are collected on a filter located in a filter holder at the end of the probe. c) Linked to the probe, there is the DMA for on-line measurement (for a simplification of the image, DMA has been painted at 90 degrees with respect to the sampling line).

The sampling system was similar to collect particles in the flame doped with 30% Benzene, as shown in Figure 4.4. However, there was a need to introduce benzene in this second apparatus. Benzene had to be vaporized by a condenser from which air and  $N_2$  enter. The three components pass through a tube about 6 m long, heated by appropriate heating elements, and then mix with ethylene just before entering the burner.



## 4.3 EXPERIMENTAL TECHNIQUES

### 4.3.1 DIFFERENTIAL MOBILITY ANALYSIS (DMA)

Differential mobility analysis (DMA) is one of the possible detection systems that give some information about particle size distribution function leading to a clear view of what happens in the flame.

DMA utilizes two simple principles: separation of particles forming a mono-disperse aerosol and counting particles present in this aerosol.

DMA consists of three components: a neutralizer, an electrostatic classifier, and a detector.

The neutralizer charges particles with a known steady-state charge distribution, which are then selected for their electrical mobility in the electrostatic classifier and divided into different monodisperse aerosols. The detector counts the number of particles per unit volume of each monodisperse aerosol. A Condensation Particle Counter (CPC), based on an optical counting of particles, or an Electrometer, a very sensitive ampere-meter that directly measures the charges, can be used as detectors.

The electric field, which is radially oriented, acts on charged particles that flow through. Charged particles change their trajectory according to laws of interaction between charges and electric fields. The particles' movement is strongly dependent on the electrical mobility diameter,. With an opportune opening at the end of the cylinders and by varying the electric field applied, it is possible to obtain from a poly-disperse aerosol many different mono-disperse aerosols according to the law of Millikan-Fuch for spherical particles:

$$Z = \frac{qeC_e}{3\pi\mu d_M} \quad (4.1)$$

Where  $q$  is the number of charges in the particle,  $e$  is the unit charge, and  $\mu$  is the carrier gas's viscosity. The Cunningham factor  $C_e$  is a function of the Knudsen number (Hinds, 1982).

The mono-disperse aerosol is sent to the particle counter, which gives the number of particles per volume. The analysis of single mono-disperse aerosols can reconstruct the particle size distribution function.

CPC counts the particles after they pass through a chamber in which a supersaturated atmosphere of volatile alcohol, generally butanol, is created to let particles grow and thus more easily be counted. The counting method depends on the type of particles, supersaturating level, and how particles grow; however, it has been quite reliable for a wide range of conditions. Several errors could occur during the analysis because of the instrument and the sampling system, but many adjustments can minimize the sampling effect on the sampled material.

In the studied system and sampling method, such as the flame and probe sampling, the possible artefacts generally rely on two points: the perturbation on the flame and the effect on the material within the probe. The first one is almost impossible to avoid since the insertion of a sampling system in the flame cause somewhat perturbation. However, the perturbation can be minimized by reducing the size of the probe.

The Differential Mobility Analysis system used for this research activity was a TSI equipped with an X-ray charger (TSI Model 3088), an electrostatic classifier (TSI Model 3082), and counted by an ultrafine condensation particle counter (TSI Model 3776). The aerosol flow was set at 1.5 L/min, and the sheath flow at 15 L/min, the particle size region achieved by the instrument is 1.98-65 nm with high voltage at 9700 V, no impactor was used. The Aerosol Instrument Manager (AIM) operating software converted the measurement data to the size distributions, calculated as  $dN/d\log D_p$ . Afterwards, corrections for multiple charge and diffusion loss were performed using the Multi-Instrument Manager software.

#### 4.3.2 RAMAN SPECTROSCOPY

Raman spectroscopy is vibrational spectroscopy, considered a powerful technique to investigate the chemical and structural modification of nanostructures.

In 1928 Raman discovered this new type of radiation (Raman and Krishnan, 1928), which led him to the Nobel Prize in Physics in 1930. Raman spectroscopy is a two-photon inelastic light-scattering event. Here, the incident photon is of much greater energy than the vibrational quantum energy and loses part of its energy to the molecular vibration with the remaining energy scattered as a photon with reduced frequency. In Raman spectroscopy, the interaction between light and matter is an off-resonance condition involving the molecule's Raman polarizability.

Raman vibrational spectra are composed of bands that are characterized by their frequency (energy), intensity (polarizability), and band shape (environment of bonds). Since the vibrational energy levels are unique to each molecule, the Raman spectrum provides a "fingerprint" of a particular molecule. These molecular vibrations' frequencies depend on the masses of the atoms, their geometric arrangement, and their chemical bonds' strength. The spectra provide information on molecular structure, dynamics, and the environment.

In a typical Raman experiment, a laser is used to irradiate the sample with monochromatic radiation. Laser sources are available for excitation in the UV, visible, and near-IR spectral region. The light scattered photons revealed by Raman spectroscopy include the dominant Rayleigh elastic

scattering and only a minimal amount of Raman scattered light, both processes are depicted in Figure 4.5. No energy is lost for the elastically scattered Rayleigh light while the Raman scattered photons lose some energy relative to the exciting energy to the specific vibrational coordinates of the sample.

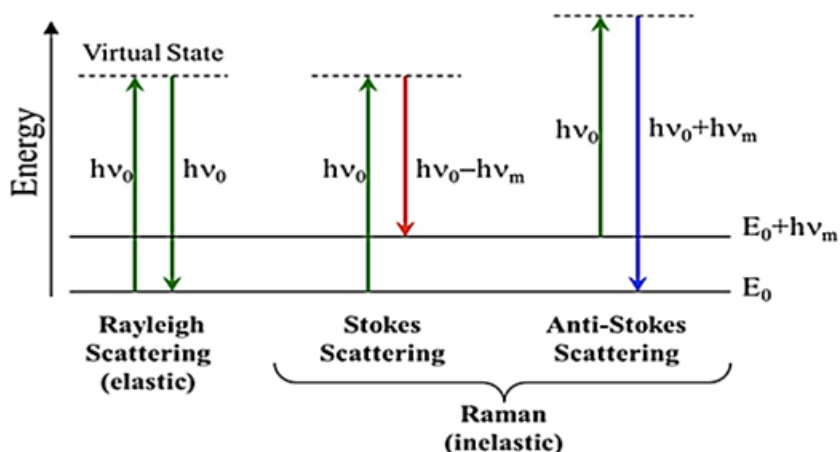


Figure 4.5 Jablonski diagram of Rayleigh and Raman scattering representation.

Both Rayleigh and Raman are two-photon processes involving the incident light's scattering, from a "virtual state." A transition from the ground state momentarily absorbs the incident photon into a virtual state, and a new photon is created and scattered by a transition from this virtual state.

Rayleigh scattering occurs when the scattered photon transitions from the virtual state back to the ground state. This elastic scattering, resulting in no change in energy (i.e., occurs at the laser frequency) is the most probable event with a scattered intensity is ca.  $10^{-3}$  less than that of the original incident radiation. Conversely, Raman scattering is far less probable than Rayleigh scattering with an

observed intensity ca.  $10^{-6}$  less than that of the incident light for strong Raman scattering. This scattered photon results from a transition from the virtual state to the first excited molecular vibration state.

As shown in Figure 4.5, two types of Raman scattering exist, Stokes and anti-Stokes. Molecules initially in the ground vibrational state give rise to Stokes Raman scattering, molecules in the vibrationally excited state give rise to anti-Stokes Raman scattering. The Stokes' intensity ratio relative to the anti-Stokes Raman bands is ruled by the sample's absolute temperature and the energy difference between the ground and excited vibrational states. At thermal equilibrium, Boltzmann's law describes the ratio of Stokes relative to anti-Stokes Raman lines. The Stokes Raman lines are much more intense than anti-Stokes since most molecules are in the ground state at ambient temperature.

Figure 4.6 reports a typical Raman spectrum of diffused light reported as intensity (arbitrary units) concerning the Raman shift, i.e. the shift from incident light frequency. Stokes and Anti-Stokes lines are symmetrical with the Rayleigh line, and the position of the peaks for the Rayleigh line represents the energy shift that occurred during molecule variation of its initial vibrational level. Stokes lines provide information about molecule functional groups and their vibrational modes.

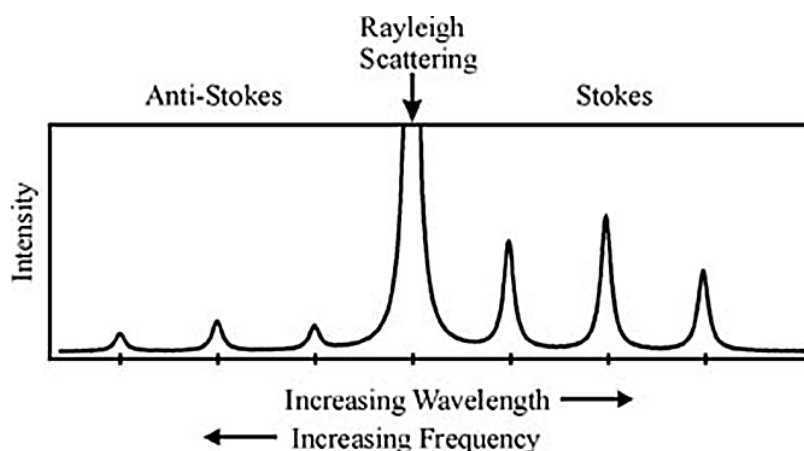


*Figure 4.6 Scattered light spectrum. Stokes and Anti-Stokes lines are symmetrical with the Rayleigh line. (www.omegafilters.com)*

Raman spectroscopy system consists of:

- Laser beam generator;
- A sampling system to deliver a laser beam on the sample and collect Raman signal;



- A filter system to separate Raman scattering signal from Rayleigh elastic one;
- A detector.

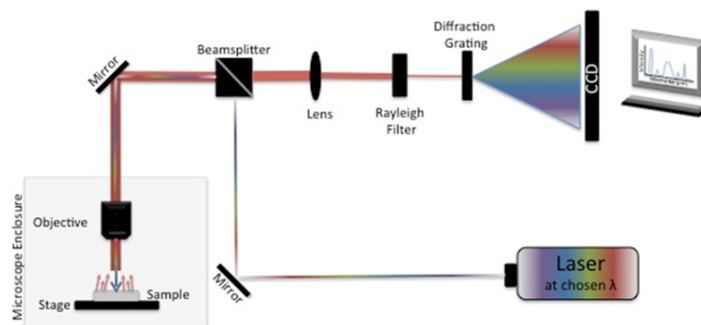


Figure 4.7 Blocks diagram of Raman spectrometer (Baker, Hughes and Hollywood, 2016).

The laser beam from an excitation source overcomes a series of filters to isolate a monochromatic light, cutting all other frequencies and focalized on the sample using a microscope objective. Diffused light focusing on a mirror passes through some filters to remove laser wavelength (commonly a notch and edge filter). Scattered light, mainly composed of inelastically component, is then focused on the detector that collects the signal sending it to a computer for processing.

Raman spectroscopy plays an essential role in characterizing carbon materials, mainly because it gives some necessary chemical/structural information.

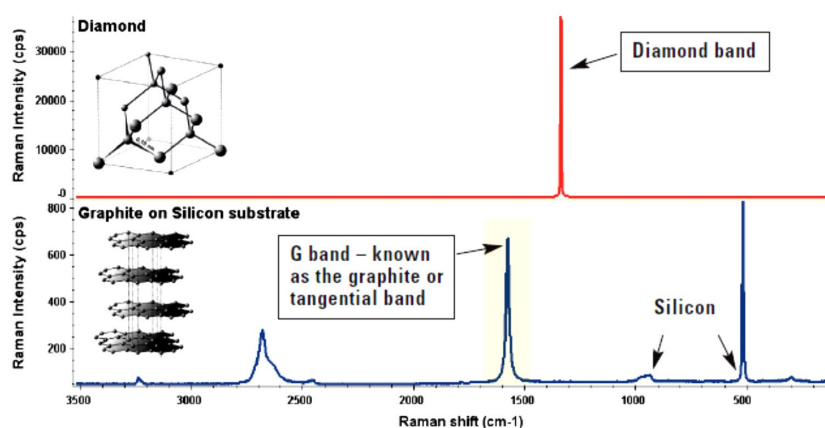


Figure 4.8: Raman spectra of diamond and a sample of graphite on a silicon substrate(Thermo Scientific)

Figure 4.8 shows several standard features of the Raman spectra of two carbon materials such as Graphite and Diamond. The 800–2000  $\text{cm}^{-1}$  region, the first-order region, is mainly dominated by the so-called G and D peaks, which lie at around 1580  $\text{cm}^{-1}$  and 1350  $\text{cm}^{-1}$  for visible excitation (Ferrari and Robertson, 2001b).

The G peak (graphitic peak), which is due to every  $\text{sp}^2$  bond, is mostly insensitive to defects only presenting small changes in width and position of the maximum as a function of the different carbon structures. The D peak (Disorder peak) is observed at about 1350  $\text{cm}^{-1}$ . It is due to disorder produced by defects in the otherwise perfect aromatic network. Defects could be of different types (small crystallite sizes or grains, vacancies). The second-order region, 2000–3500  $\text{cm}^{-1}$ , of the Raman spectrum, is due to overtones and combination modes of the bands observed in the first-order region.

Raman analysis was performed in this thesis work using a Horiba Xplora Raman Microscopes equipped with a 100X objective (NA0.9, Olympus). The laser source was a frequency-doubled Nd: YAG laser ( $\lambda = 532 \text{ nm}$ , 12 mW maximum laser power at the sample) and an infrared laser ( $\lambda = 785 \text{ nm}$ ). The system's calibration was performed against the Stokes Raman signal of pure silicon at 520  $\text{cm}^{-1}$ . A 200  $\mu\text{m}$  pinhole was used for confocal photons collection. The excitation laser beam's power and exposure time were opportunely adjusted to avoid the sample's structural changes due to thermal decomposition. Spectra were obtained with a laser beam power of 1%, and then baseline corrected and normalized to the maximum of the G peak.

#### 4.3.3 ELECTRON PARAMAGNETIC RESONANCE (EPR)

For the first time, the study of carbon nanoparticles produced in a laminar flame is implemented with resonance techniques, specifically EPR and NMR.

The first one is a technique used in this work for the detection of radicals in flame. EPR technique can also identify which kind of radicals are present in the analyzed compounds. Namely, the technique gives information such as the unpaired electron's position if placed on a C atom or upon/near a heteroatom. This information is of extreme importance to understand the presence of oxygen, for example. Some examples of EPR analysis of similar materials could mention EPR acquisition performed on particulate soot emissions and residue ash from controlled combustion of common types of plastic (Valavanidis *et al.*, 2008)

broadness of the EPR signal indicates the presence of several paramagnetic species. Also, cigarette tar has been analyzed by EPR (Church and Pryor, 1985). These analyses revealed that cigarette tar contains several exceptionally stable radical species observed directly by electron spin resonance spectroscopy. Moreover, EPR analyses were performed to study the atmospheric environment (Yordanov, Lubenova and Sokolova, 2001) in different places to separate the contribution of various carbon compounds to air pollution.

However, in this thesis work, this technique has been applied to investigate the presence of radicals previously observed by AFM analysis (Commodo *et al.*, 2019; Schulz *et al.*, 2019) and study the change of the radical nature as the particles evolved in flame.

EPR is a non-destructive analytical technique and is the only method available to detect paramagnetic species directly. EPR allows the identification and quantification of free radicals and transition metal ions in solids, liquids, gases, cells, and in vivo. From cell membranes to nano-diamonds, EPR applications spread far and wide through many fields: chemistry, material research, life science, quantum physics and quality control. In electrochemistry, redox chemistry, photochemistry, and catalysis, EPR can study metal centres and radicals involved in chemical processes. Among the many areas in material science, applications include polymer synthesis, testing the purity of silicon in solar cells, and characterising nano-diamonds and diamond grading. In this thesis work, EPR proved to be a magnificent technique that allowed us to confirm radicals' presence and study their role in the flame evolution process.

EPR is a resonance spectroscopy technique that utilizes microwave radiation to probe species with unpaired electrons, introduced in an externally applied static magnetic field. Therefore, this technique's application is handy in studying paramagnetic species and characterization of those species' chemistry and kinetic formation.

An electron is a negatively charged particle with two types of angular movements, showed in Figure 4.9. The first one is the spinning around the nucleus, which brings to an orbital magnetic moment,  $\mu_l$ . The other is the intrinsic angular momentum, spin magnetic moment,  $\mu_s$ .

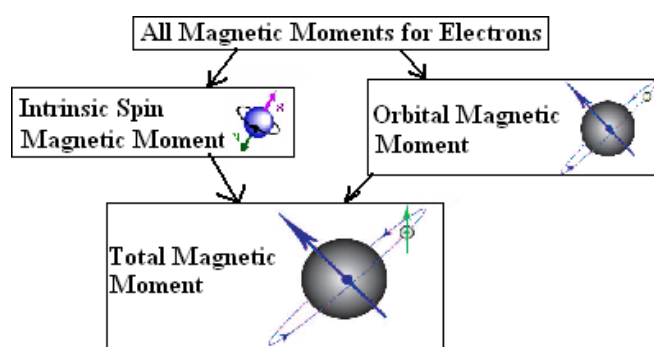


Figure 4.9 Representation of magnetic moments for electrons

Electrons angular magnetic momentum and spin momentum are reported in the following equations:

$$\mu_l = -\frac{e}{2m_e} \sqrt{l(l+1)} \frac{h}{2\pi} = -\mu_B \sqrt{l(l+1)} = -\mu_B m_l \quad (4.2)$$

$$\mu_s = -g \frac{e}{2m_e} \sqrt{s(s+1)} \frac{h}{2\pi} = -g\mu_B \sqrt{s(s+1)} = -g\mu_B m_s \quad (4.3)$$

where:

- $e$  = electronic charge;
- $m_e$  = electron mass;
- $l$  = angular quantum number;
- $m_l$  = magnetic quantum number;
- $s$  = spin quantum number;
- $m_s$  = magnetic spin quantum number;
- $h$  = Planck constant;
- $g$  = Landè factor;
- $\mu_B$  = Bohr magneton.

The Bohr magneton,  $\mu_B$ , is the value of the orbital magnetic moment of hydrogen atom electron in the ground state. It represents a fundamental physics constant for measurement of the magnetic moment of atoms, atomic nuclei, electrons, and subatomic particles momentum, and it is defined as:

$$\mu_B = \frac{eh}{4\pi m_e} \quad (4.4)$$

The Landè factor,  $g$ , is a characteristic parameter of the radical whose value depends on:

- the angular spin momentum;
- the orbital angular momentum (which depends on the shape and symmetry of the electron orbital);
- the environment around the electron.

The factor  $g_e$  is known as the free electron g-factor with a value of 2.002319304386 (one of the most accurately known physical constants).

In the situation of a single unpaired electron,  $m_s$  assumes two values that are  $m_s = \frac{1}{2}$  and  $m_s = -\frac{1}{2}$  also indicating like the two spin states known as  $\alpha$ , (  $\uparrow$ , spin up) and  $\beta$  (  $\downarrow$ , spin down). In this way,  $\mu_s$  assumes these following expressions:

$$\mu_s = \left\{ -g\mu_B \frac{1}{2}; g\mu_B \frac{1}{2} \right\} \quad (4.5)$$

In the absence of an external magnetic  $\alpha$  and  $\beta$  are degenerate.

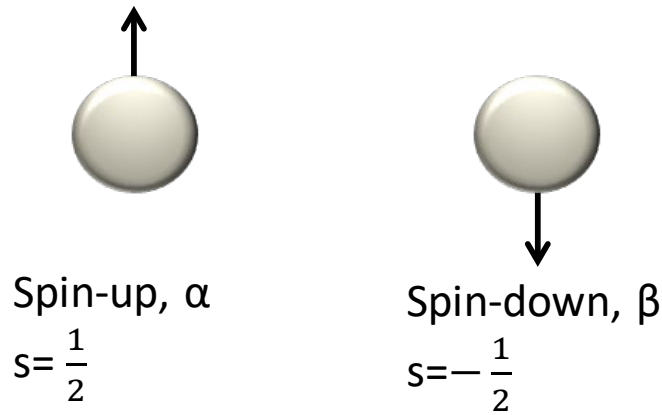


Figure 4.10: spin up and down prefiguration

When the electron interacts with an external magnetic field ( $B$ ), the interaction energy will be equal to:

$$E = -\mu_s B = -(-g_e \mu_B m_s) B = +g_e \mu_B m_s B \quad (4.6)$$

Therefore,  $E$  is different for the two different spin states:

$$E_+ = E_{+\frac{1}{2}} = +\frac{1}{2} g \mu_B \text{ for } m_s = +\frac{1}{2} (\text{spin up}; \alpha) \quad (4.7)$$

$$E_- = E_{-\frac{1}{2}} = -\frac{1}{2} g \mu_B \text{ for } m_s = -\frac{1}{2} (\text{spin down}; \beta) \quad (4.8)$$

The difference between the two energy states,  $E_+ - E_- = \Delta E = g_e \mu_B B$  is defined as electron-Zeeman splitting, which is proportional to the strength of applied external magnetic field  $B$ , as displayed in Figure 4.11. At a value of  $B=0$ , the two energy levels are degenerate, but the energy difference increases with  $B$ .

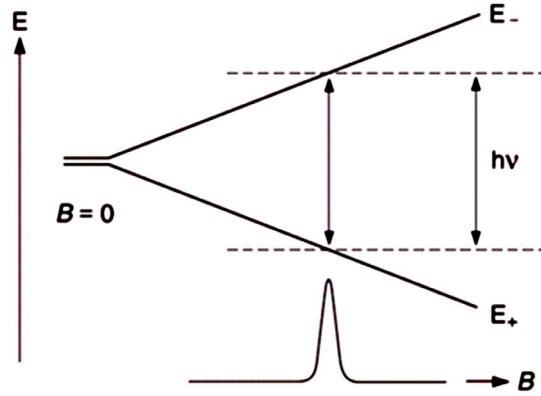


Figure 4.11: Electron- Zeeman splitting representation.

The transition between the two levels, i.e., spin inversions  $\alpha \leftrightarrow \beta$ , is induced by an electromagnetic radiation  $h\nu$ , provided that:

- the direction of the magnetic field associated with this radiation is perpendicular to that of the external magnetic field  $B$ , i.e., it lies in the XY plane;
- the energy of the radiation is equal to that of the Zeeman splitting,  $h\nu = g_e \mu_B B$ .

The second point is the well-known resonance condition, expressed as:

$$\nu = g_e (\mu_B / h) B = \gamma B \text{ or } \omega = g_e \left( \frac{\mu_B}{\hbar} \right) B = 2\pi\gamma B \quad (4.9)$$

where  $\nu$  (in  $\text{Hz} = \text{s}^{-1}$ ) is the frequency of the electromagnetic radiation. Conversely,  $\omega = 2\pi\nu$  is the angular frequency that is also the frequency of the spin  $S$  processing around  $B$ , Larmor frequency.

An EPR experiment could be acquired by varying  $\nu$ ,  $B$ , or both to attain the resonance condition. For technical reasons, the choice falls in keeping the frequency  $\nu$  constant and varying the field strength  $B$  to bring it to the value at which the resonance condition is rewarded. One generally uses the microwave

(MW) X band with a ca. 9500 MHz frequency, which requires a field strength B of ca 340 mT.

Besides the resonance condition, other pre-requisites are required for a successful electron spin resonance experiment. Indeed, to observe an ESR signal, many electrons in a suitable environment are needed.

The numbers of electrons in the two Zeeman levels,  $E_+$  and  $E_-$ , are their populations  $n_+$  and  $n_-$ , respectively. According to the Boltzmann distribution law, the ratio of these populations is:

$$\frac{n_+}{n_-} = e^{\frac{\Delta E}{kT}} = e^{\frac{-g\mu_B B}{kT}} \quad (4.10)$$

where k is the Boltzmann constant, and T is the absolute temperature in K.

In the absence of an external magnetic field the two population are degenerate but for  $B > 0$ , the population  $n_-$  is larger than  $n_+$ , i.e., there is an excess of spins in the lower energetic level than the higher one.

A transition occurs when some spin-up electron converts in spin down. This process, leading to magnetization, involves energy transfer from the spin ensemble to the lattice, and it occurs by spin-lattice relaxation (SLR).

To understand the SLR effect, it needs to introduce the Heisenberg uncertainty relation,  $\Delta E \cdot \Delta t \approx \hbar$ .

An equivalent formula also expresses the Heisenberg relation:

$$\Delta\nu\Delta t = \gamma\Delta B\Delta t \approx 1/2\pi \quad (4.11)$$

Where  $\Delta\nu$  or  $\Delta B$  stands for the ESR signal's width,  $\Delta t$  is a spin state's lifetime. Thus, by relaxation time and by lifetime spin state depend on an EPR signal's width so a long, or short, lived state gives rise to a narrow, or broad, EPR signal.

The lifetime,  $\Delta t$ , of the spin state  $\alpha$  or  $\beta$  is determined by the relaxation times  $T_{1e}$  and  $T_{2e}$ :

$$1/\Delta t \sim (1/T_{1e}) + (1/T_{2e}) \quad (4.12)$$

$T_{1e}$  is the above mentioned spin-lattice relaxation (SLR) time, and  $T_{2e}$  is the spin-spin relaxation (SSR) time of electron. Whereas SLR governs energy exchange between the spins and the environment (lattice), SSR comprises interactions within the spin ensemble without such an exchange.

Generally,  $T_{1e}$  is long for organic radicals without heavy atoms ( $10^{-3}$  to  $10^{-1}$  s). Because  $T_{2e}$  is much shorter ( $10^{-5}$  to  $10^{-7}$  s) then it is possible to write:

$$1/\Delta t \sim 1/T_{2e} \quad (4.13)$$

Hence, according to the uncertainty principle, the linewidth becomes:

$$\Delta\nu = \gamma\Delta B \propto \frac{1}{\Delta t} \approx \frac{1}{T_{2e}} \quad (4.14)$$

The EPR spectrum usually reports the signals as the first derivative,  $dA/dB$ , of the absorption  $A$  concerning  $B$  as a function of  $B$ , Figure 4.12. The absorption peak  $A$  and the subsequently first derivative peak could be associated with a Gaussian, a Lorentzian, or an appropriate mixture of both curves. The bell-like form of the Gaussian curve has a broader waist and shorter tails than its Lorentzian counterpart

In an EPR spectrum is mandatory to evaluate characteristic parameters such as  $A_{\max}$ , the maximum of  $A$ ,  $\Delta B_{1/2}$ , the peak width at its half-height ( $A_{\max}/2$ ), and  $\Delta B_{pp}$ , the peak-to-peak distance of the derivative curve  $dA/dB$ , Figure 4.12.

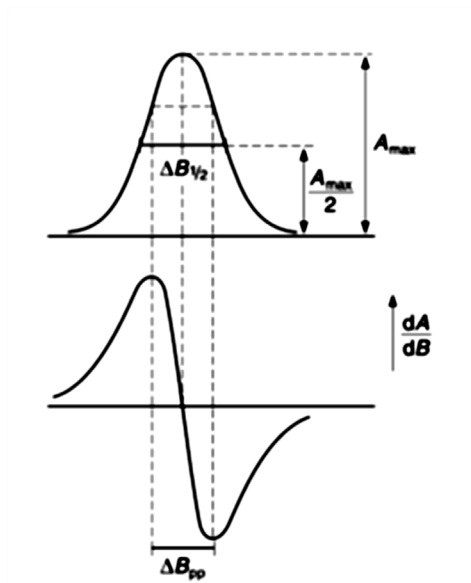


Figure 4.12: An example of EPR signal. It is usually recorded as the first derivative,  $dA/dB$ . The image also reported the characteristic parameters of a spectrum:  $A_{\max}$ , and  $\Delta B_{1/2}$ , the peak width at its half-height ( $A_{\max}/2$ ) and  $\Delta B_{pp}$ , the peak-to-peak distance of the derivative curve  $dA/dB$ .



By formula 3.9 the resonance condition depends on both the magnetic field's intensity and the electromagnetic radiation frequency. Indeed, an EPR experiment is mandatory to specify the band in which the spectrum has been acquired. The different bands with their specification have reported in table 4.1.

*Table 4.1 Different acquisition band in an EPR experiment. For each band, the correspondent frequency and magnetic field are reported.*

<b>BAND</b>	<b>FREQUENCY (GHz)</b>	<b>MAGNETIC FIELD (Gauss)</b>
L	1.1	390
S	4.0	1430
X	9.75	3480
Q	34.0	12100
W	94.0	33500

Obviously, in a molecule, other nuclei can act as a secondary magnetic source, leading to a nucleus-electron interaction that must be taken into account. These interactions originate the peaks subdivision into a series of peaks whose number depends on nuclei types.

As regards the instrumentation, a typical EPR spectrometer. consists of the following components:

1. microwave bridge, containing the microwave source and the detector;
2. sample holder cavity;
3. magnets, placed on the sides of the sample holder;
4. controller, for data analysis and for controlling spectrum acquisition parameters.

The first component of the microwave bridge is the microwave source. The source can be a diode-Gunn or a klystron; in both cases, it can generate a microwave beam at a precise and constant frequency between 9 and 10 GHz. The radiation is sent to the sample through the waveguide and reflected from the sample holder cavity back to the microwave bridge where the detector, consisting of a photodiode, detects the light signal and transforms it into an electrical signal. This signal, first through the console and then through the computer, is reprocessed and transformed into the conventional spectrum.

Precisely, the detector consists of a Schottky barrier diode, which converts the light signal's power into an electric current. The diode current generated is proportional to the light power for the light power signal's low values called a

*linear detector*. Instead of high radiation power values, the diode current is proportional to the power's square root, and therefore it is called a *square-law detector*.

To ensure this within the microwave bridge additional radiant power, also called "bias", is sent to the detector.

Inside the microwave bridge, there is a current control system generated by the diode, as if this exceeds 400  $\mu\text{A}$ , the power of the radiation is too high for the detector which could be damaged. When this situation occurs, the radiant power is automatically lowered.

The sample holder cavity consists of a metal container whose geometry changes according to the sample. When the resonance condition is reached, the source's radiation is held inside the cavity and not immediately reflected.

When the cavity's resonance conditions are verified, the radiation's electrical and magnetic components are out of phase: when the electric field is at the minimal value, the magnetic field is at maximum one, and vice versa.

Therefore, it is worth placing the sample inside the cavity in the correct position to electric field interference during the measurement acquisition.

The sample is placed in a tubular cuvette and then in the cavity.

In this work, EPR spectroscopy experiments are acquired for Carbon nanoparticles produced by flame and collected on several quartz and Teflon filters. The sampling procedure was explained in paragraph 4.2. The production of flame Carbon nanoparticles was performed using a horizontal tubular probe with a downward orifice positioned at the flame's sampling point. For the filters acquisition in the EPR experiments, the used probe was characterized by a 0.3mm orifice. The analysis was carried out employing X-band (9 GHz) Bruker Elexys E-500 spectrometer (Bruker, Rheinstetten, Germany), equipped with a super-high sensitivity probe head.

Defined quartz filters were co-axially inserted in a standard 8 mm quartz sample tube, and the measurements were performed at 25 °C. The instrumental settings were as follows:

- sweep width, 100 G;
- the resolution, 1024 points;
- modulation frequency, 100 kHz;
- modulation amplitude, 1.0 G.

EPR spectra were recorded at an attenuation value of 15 dB, and 128 scans were accumulated to improve the signal-to-noise ratio. The g-factor values were

evaluated through an internal standard (Mg/MnO), inserted in the quartz tube co-axially with the samples.

#### 4.3.4 NUCLEAR MAGNETIC RESONANCE (NMR)

The second resonance technique, NMR, is widely adopted in organic chemistry, and also routinely used to characterize hydrocarbon fuels, solvent-soluble coal fractions, and asphaltenes (Guillén, Díaz and Blanco, 1998; Dutta Majumdar *et al.*, 2013) but only a few attempts have been performed for soot analysis and more in general for fuel-combustion products (Santamaría *et al.*, 2006, 2007).

In our specific case, NMR proved to be very useful in identifying H atoms belonging to functional groups responsible for forming the radicals involved in different evolutionary patterns of PAHs in the flame in the nucleation process.

NMR analysis acquisition utilizes basic properties of atoms, namely the ability to create a magnetic field by rotating around its axis, i.e., through its spin.

The atomic nucleus possesses a charge and charge in motion generates a magnetic field, characterized by its proper magnetic moment,  $\mu$ .

The spin properties of protons and neutrons in a nucleus combine to define the total spin, namely the nuclear spin quantum number ( $I$ ), from which their possible magnetic moment derives. Indeed, not all atomic nuclei have magnetic properties, but only nuclei with  $I \neq 0$ , namely all those nuclei with odd atomic numbers and/or atomic mass.

The most studied nuclei in the NMR analysis are  $^1\text{H}$  and the  $^{13}\text{C}$  both with the quantum spin  $I$  number equal to  $\pm 1/2$ .

The following equation relates  $I$  and  $\mu$ :

$$\mu = \frac{\gamma \cdot I \cdot h}{2\pi} \quad (4.15)$$

Where  $h$  is Planck's constant and  $\gamma$  is the gyromagnetic ratio representing the nucleus frequency in an external magnetic field. This parameter differs from a nucleus to another being an intrinsic characteristic of the nucleus, not predicted theoretically but only experimentally.

Related to  $I$  there is the magnetic quantum number,  $m=2I+1$ , that represents the number of spin states in which a nucleus is split in an external constant magnetic field ( $B_0$ ).

Being  $I = \pm 1/2$ ,  $m=2$  represents the two energy state levels  $\alpha$  and  $\beta$ , which are degenerate in the absence of magnetic perturbation. When an external magnetic field is applied, the two energy levels split and  $\alpha$  level,  $\mu=1/2$  parallel to a magnetic field, goes to an energy level lower than  $\beta$  one,  $\mu=-1/2$  antiparallel to the magnetic field.

The theory of NMR is very similar to the EPR, described in the previous paragraph. Therefore, the following will be reported only a brief overview of NMR experiment principles.

NMR acquisitions work within Radio Frequencies (RF) range and when the absorption of a photon in the RF region occurs, a transition between the two energy states, with the spin inversion, is involved, as shown in Figure 4.13

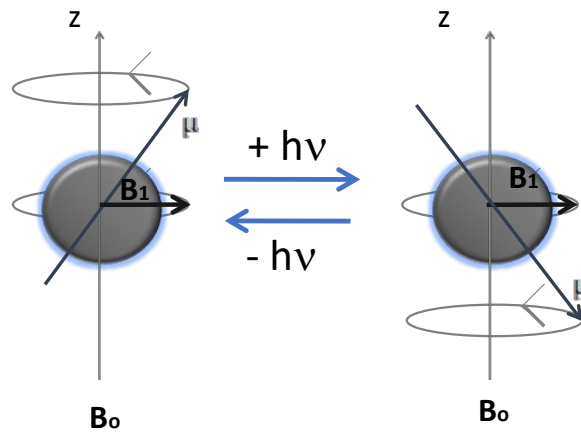


Figure 4.13 A spin inversion occurs when a nucleus in an external magnetic field, absorbs or emits a photon. Adapted from (James, 1998)

This photon's energy must be precisely equal to the difference in energy between the two states, namely  $\Delta E = \hbar\nu$ . The frequency  $\nu$ , in turn, in addition to the magnetic field strength depends on the gyromagnetic  $\gamma$  ratio of the particle:

$$\nu = \gamma B_0 \quad (4.16)$$

Therefore, the energy gap could be expressed as:

$$\Delta E = \frac{\hbar\gamma}{2\pi} B_0 \quad (4.17)$$

Equation 3.17 is defined as a resonance condition, mandatory for the transition between the two spin states; the irradiation frequency is defined as resonance frequency or Larmor frequency.

As the applied field  $B_0$  increases, the frequency of Larmor increases, and therefore the difference in energy between the two levels increases.

Even in this case, Boltzmann distribution regulates the population ratio between the two states, that is:

$$\frac{N_\beta}{N_\alpha} = e^{\frac{\Delta E}{k_B T}} \quad (3.18)$$

When the sample is irradiated by electromagnetic radiation with a frequency equal to the frequency of Larmor, an interaction between the magnetic component of the radiation and the magnetic moments nuclear is possible. The radiation's energy can be transferred to the nuclei causing the spin inversion and generating the resonance condition.

In the first NMR instrumentations, the acquisition was performed by irradiating the sample, immersed in the  $B_0$  magnetic field, with a beam of radiowaves of increasing frequency to excite in sequence all the nuclei under examination. Then the amount of radiation absorbed was recorded. This technique, however, results too slow and is no longer used.

In modern FT-NMR instruments, the signal is generated with the pulse method and the Fourier transform. With this technique, all the nuclei are excited at the same time by a radiofrequency pulse, and then the data are computer-processed with the Fourier transform technique.

To better explain the NMR acquisition, the vector  $M_0$ , Macroscopic Magnetization, need be introduced.  $M_0$  is the resultant of all nuclear magnetic moments, as pictured in Figure 4.14.

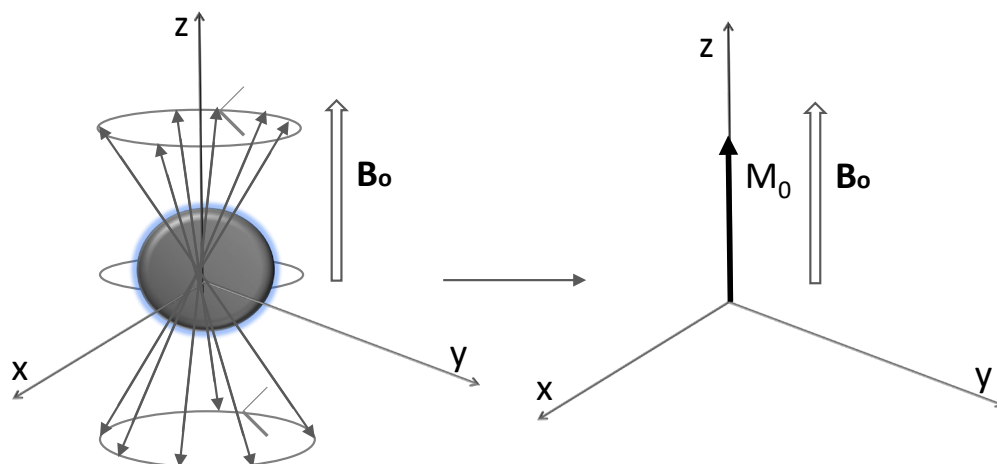


Figure 4.14 A representation of  $M_0$  vector. The sum of all nuclear magnetic moments results in this vector. Adapted from (James, 1998)

Since there is a slight excess of nuclei aligned with the  $B_0$  magnetic field, the vector  $M_0$  is small and aligned with the field along the z-axis. When irradiation occurs, along the x-axis, the nuclei absorb the energy and undergo a spin transition, generating the rotation of  $M_0$ , which acts like a whirligig.

Starting from the z-axis,  $M_0$  approaches the XY plane, starting a precessional motion, as shown in Figure 4.15.

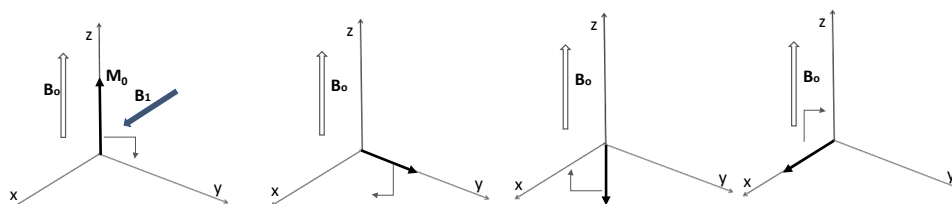


Figure 4.15 A representation of precession movement of  $M_0$  vector. When the external magnetic field  $B_1$  irradiates the nuclei along the XY plane, the  $M_0$  pass through the YYZ plane and go into XY plane to return in the initial position along the Z-axis. Adapted from (James, 1998)

The energy absorbed by the nuclei is slowly released to nearby atoms due to spin-spin relaxation phenomena (with the dipoles of the surrounding molecules) that affect the  $M_z$  component, and spin-spin relaxation phenomena (with the hydrogen nuclei nearby) that affect the  $M_y$  component.

Because of this energy dissipation the vector  $M$ , creating a precession spiral around to the  $z$ -axis, returns to the initial value  $M_0$ , a position for which the  $M_y$  component is zero.

When the single, intense and short RF pulse is over, the nuclei in the sample return to their state of equilibrium re-emitting photons at their resonance frequency. The emission has an exponential trend over time. A graph showing the emission over time, shown in Figure 3.16, is an interferogram called FID, (Free Induction Decay).

The FID is easy to read for a single nucleus, but with more nuclei, the FID becomes almost incomprehensible. Therefore, the FID is an overlapping of radio frequencies over time emitted at different resonance frequencies depending on the nucleus that produces them.

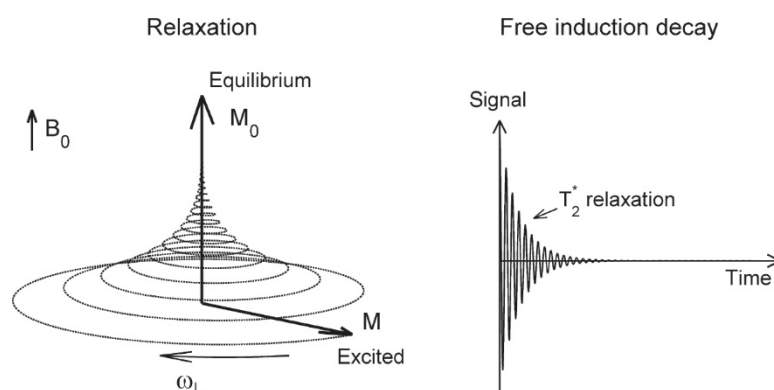


Figure 4.16 An example of relaxation process and Free Induction Decay (FID) interferogram. The Figure is taken from (Prasad and Storey, 2008)

Therefore, the usual frequency-domain spectrum can be obtained by computing the Fourier transform of the signal-averaged FID.

Thus, the FID emission is a representation of the relaxation of the nucleus to the equilibrium state.

In the NMR, the relaxation times are divided into :

- the nuclear spin-lattice relaxation time or longitudinal relaxation time ( $T_1$ ), that is a measure of how fast the magnetization relaxes back along the  $z$ -axis;
- nuclear spin-spin relaxation time or transverse relaxation time ( $T_2$ ) measures how fast the spins exchange energy in the transverse (XY) plane.

In Figure 4.17, an NMR spectrometer representation is reported. The spectrometer is composed by:

1. Superconducting solenoid, to generate the magnetic field at the desired intensity. It is placed in a dewar of liquid Helium and in a dewar of liquid Nitrogen to reach low temperature;
2. Shim coils (RF coils), to produce radiofrequency field;
3. Probe, to place the sample ;
4. Computer, to connect the spectrometer through software. The software is useful both for data analysis and for controlling spectrum acquisition parameters.

The heart of the NMR spectrometer is the superconducting magnet, kept at 4 K by liquid Helium . The probe, containing the RF coil, sits at the bottom of the magnet within its bore. The sample is placed within the NMR tube; it is gently dropped into the probe on an air cushion. Here the superconducting magnet causes the spin of the proton, and the RF coil sends RF pulses to excite them and collects the free-induction decay as they relax back to equilibrium. The pulse programs are performed using the computer and sent to the console, that acts both as a radiofrequency transmitter and receiver. The signals are amplified on transmission and receipt. The FIDs are mathematically deconvoluted to produce NMR spectra of intensity versus chemical shift ( $\delta$ ).

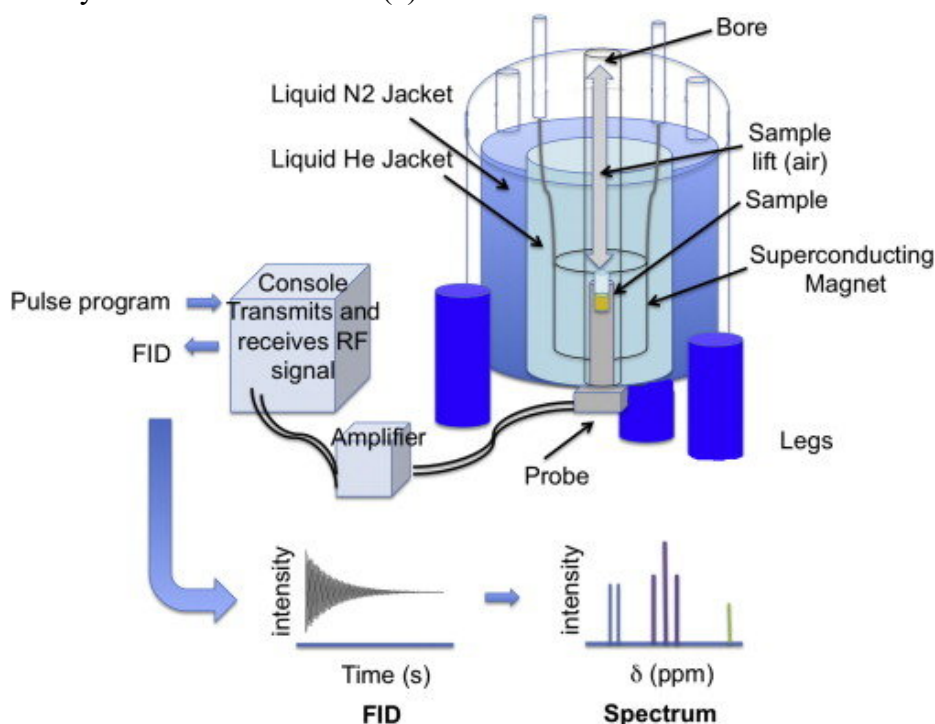


Figure 4.17 NMR spectrometer. (Rankin *et al.*, 2014)



### *Chemical shift*

The main characteristic of NMR analysis is that similar protons absorb at slightly different frequencies according to their chemical surroundings. Indeed, a hydrogen atom strongly depends on the electronegativity of the atom to which it is bound. With the application of an external magnetic field, each atom's electrons generate a small opposite magnetic field. Therefore, the effective magnetic field ( $B_{\text{eff}}$ ) will be different from the applied one,  $B_{\text{eff}} = B_0 - \sigma B_0$ , with  $\sigma$  defined as shielding factor. When an H bonds a poorly electronegative atom, bond electrons are closer to H, a greater shielding effect occurs with a more intense induced magnetic field, which decreases more the effective field ( $B_{\text{eff}} = B_0 - \sigma B_0$ ) and then undergoes the transition to a lower frequency.

Conversely, a proton, bonded to more electronegative atoms, result in less shielding from the bonding electrons. Thus, a weaker induced field and a more intense effective field ( $B_{\text{eff}} = B_0 - \sigma B_0$ ) occur, and protons absorb higher frequencies.

The absorbed frequency variation is responsible for the signal position in the spectra, called chemical shift,  $\delta$ . Differences in nuclei absorption frequencies are on hundreds of Hz relative to and dependent on spectrometer frequency values (MHz). Therefore, to compare spectra obtained from spectrometers with different magnetic fields, a relative dimensionless scale is used in which the difference in signal resonance, measured concerning an internal reference, is normalized for the spectrometer frequency.

By convention, the internal reference is the tetramethylsilane (TMS)  $\text{Si}(\text{CH}_3)_4$  with a value of chemical shift equal to zero. The protons of TMS are strongly shielded because of the low electronegativity of silicon, and thus, the chemical displacements of all organic molecules are always positive.

In summary, the absolute chemical shift is the difference between the absorbed frequency (in Hz) of the examined hydrogen ( $H_e$ ) and that of the hydrogen of TMS (H TMS):

$$\text{Absolute chemical shift} = \text{Hz}(H_e) - \text{Hz}(\text{H TMS}) \quad (4.19)$$

The absolute chemical shift is proportional to  $B_0$  because it is generated by electron shielding induced by the same  $B_0$  magnetic field. Thus, NMR spectrometers using more intense magnetic fields produce more significant chemical displacements.

It is preferable to use only one reference scale, that is the relative chemical shift  $\delta$ , expressed in ppm and defined as follows:

$$\delta = \frac{\text{frequency of signal (Hz)} - \text{frequency of standard (Hz)}}{\text{spectrometer frequency (MHz)}} * 10^6$$

$$= \frac{\nu_{He} - \nu_{TMS}}{\nu_{INS}} * 10^6 \quad (4.20)$$

Generally, hydrogen or carbons bond to more electronegative atoms are unshielded, therefore affected by a more intense applied magnetic field and undergo the transition to higher frequencies and, in the spectrum, are located further to the left, at a higher chemical shift, as illustrated in Figure 4.18.

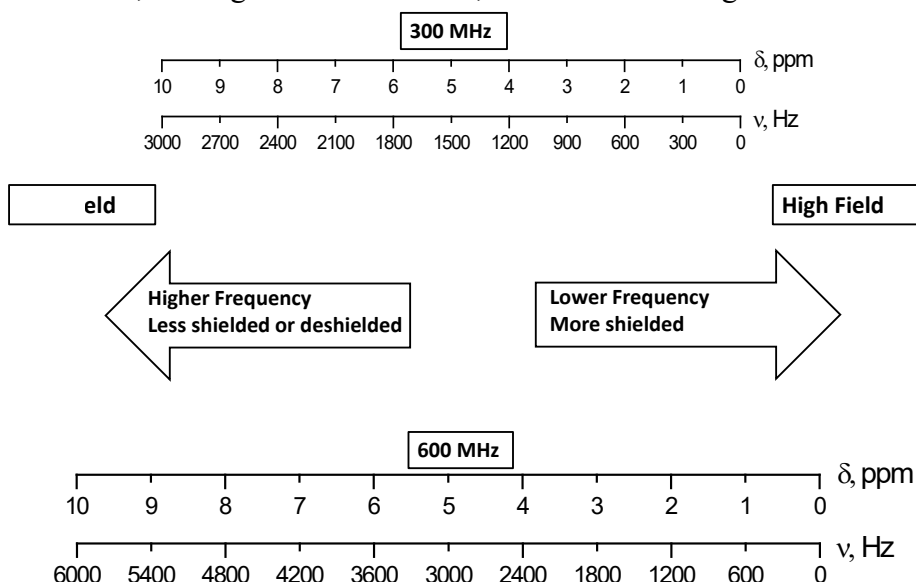


Figure 4.18 A scheme of chemical shift in the spectrum.

The ability to distinguish the several protons is fundamental for the flame particles. The possibility of recognising, identifying, and confirm the presence of specific and characteristic protons for radicals formation has been a significant step in researching carbon particles produced in flame.

Moreover, through the NMR technique, it is possible to discriminate between alkanes, alkaline, methylenic, allylic, or aromatic H. Indeed, the  $\pi$  electron cloud creates a phenomenon, known as ring current, more or less intense depending on the chemical compounds. During this phenomenon, the magnetic field induced,

produced by the  $\pi$  cloud, is opposite to the applied field  $B_0$  in the middle of the molecule (shielding effect), but concordant with  $B_0$  in the peripheral area, where there are the vinyl and phenyl hydrogens (deshielding effect). Therefore, these hydrogens are affected by an effective field more intense than  $B_0$  and absorb at a  $\delta$  particularly high.

Other phenomena and effects affect an NMR spectrum, but the full description is beyond this work's scope. On the contrary, the ring current's effect, as mentioned above, is directly related to this thesis's research work.

The distance (in ppm) between the resonant frequency observed and the TMS signal depends on the proton's chemical environment, i.e. the molecular structure. Different protons in different parts of the molecule have a distinct chemical shift and molecules give a specific pattern of peaks, in terms of both the chemical shift and the intensities of those peaks.

An NMR spectrum could be subdivided into different small regions depending on the protons which produce the signal.

In this research work, for the NMR analysis, the carbon particles collected on quartz filters were dissolved and extracted. The sampling procedure was explained in paragraph 4.2. The production of flame Carbon nanoparticles was performed using a horizontal tubular probe with a downward orifice positioned at the flame's sampling point. In NMR experiments, the used probe had a 2.5 mm orifice and particles were collected at an 8 mm of distance from the burners. The quartz filters were dissolved in 60 ml Chloroform ( $\text{CHCl}_3$ ) by stirring for 24 hours and dried up with a Rotavapor. Then the residue was dissolved in deuterated chloroform ( $\text{CDCl}_3$ ) to be placed into an NMR cuvette, as shown in figure 4.19:

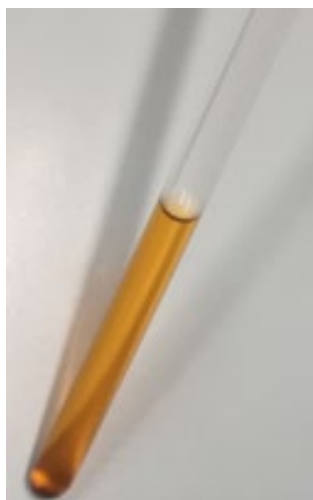


*Figure 4.19 NMR tubes with Carbon Nanoparticles dissolved in CHCl<sub>3</sub>.*

NMR cuvette is a cylindrical glass tube with a 5 mm x 20 cm dimension in which a max of 1 mL of the sample solution is to insert. The NMR analysis was carried out with a *Bruker Ascend<sup>TM</sup>* spectrometer operating at the <sup>1</sup>H frequency of 400.130 MHz in CDCl<sub>3</sub>. <sup>1</sup>H spectra were obtained using the following parameters: 128 transients, 65 K data points.

For NMR analysis, deuterated solvents are used, particularly chloroform is the most widely used. The deuterated solvents always show a slight protonic residue, whose signal occurs in a specific and always the same chemical shift value. Using CDCl<sub>3</sub>, an overlapping signal at 7.24 ppm is present in the spectra, causing some inaccuracy.

## 4.4 DENSITY FUNCTIONAL THEORY (DFT)

There are many fields within the physical sciences and engineering where the key to scientific and technological progress is understanding and controlling the properties of matter at the level of individual atoms and molecules. DFT is a phenomenally successful approach to finding solutions to the fundamental equation that describes the quantum behaviour of atoms and molecules, the Schrödinger equation, in practical value settings (Sholl and Steckel, 2009). This approach has quickly gone from being a technique used by a small number of researchers, mainly chemists and physicists, to being a tool used regularly by a large number of researchers in the most varied science applications.

DFT is a computational quantum mechanical modelling method used in several science fields to investigate the ground-state of the electronic structure of atoms, molecules, condensed phases. The proprieties of the examined systems are studied using the functional, mostly the electron density's functional.

Thus, DFT is a ground-state theory in which the emphasis is on the charge density as the relevant physical quantity. DFT has proved to be highly successful in describing structural and electronic properties in a vast class of materials, ranging from atoms and molecules to simple crystals to complex extended systems (including glasses and liquids). DFT has become a standard tool in first-principles calculations to describe – or even predicting – properties of molecular and condensed matter systems (Sholl and Steckel, 2009).

DFT theory requires knowledge and information that embraces a great chemistry and physics, the relativistic and non-relativistic quantum world. The complex concepts that have led over the decades to develop the theories and approximations of density functional go beyond this thesis's scope.

However, a multitude of DFT approximations exists, DFT is not a single method but a family of methods because the exact density functional is unknown. The values for the properties produced by them can differ significantly from a method to another. Some criteria must be used to choose a given functional to predict a given property. Most often, density functional approximations are evaluated against some benchmark data sets and quantities (like the mean error and mean absolute error) to assess the approximation's validity.

Therefore, in a specific system, the use of an approximation predicts a particular property better than another. Do not exist the best or the perfect functional or error-free one. It all depends on the type of performed studies.

DFT methods can be divided into several classes based on the types of functional dependencies that they possess. The simplest type of DFT is the local spin density approximation (LSDA), which depends only on electron density. Generalized gradient approximation (GGA) functionals depend on the electron density and its reduced gradient, while meta-GGA functionals also depend on the kinetic energy density. Hybrid and meta-hybrid functionals are combinations of GGA and meta-GGA functionals with the Hartree-Fock exchange.

As previously written, in the entire process of flame particle formation, nucleation is still the unclear step, subjected to continuous debate in the community of combustion. What is certain is that in the formation of incipient particles are involved radical species, radical PAHs, that could play a fundamental role in the evolution of CNPs in flame. In the paragraph of nucleation discussion, the difference between the two types of radicals existing in nature,  $\sigma$  and  $\pi$ , was discussed. The concept that is of fundamental priority to understand is their different behaviour in the flame at the nucleation time. How do they do react? How the unpaired electron or the unpaired electrons move along the aromatic structure? Is it possible that the presence of elements such as Penta-rings, their location in the aromatic structures, could influence particles' reactivity and mechanism?

The community's attention is also on the possibility of their dimerization and in particular, which type of dimer is formed and which dimeric configuration is more plausible that resists in the flame environment carrying the process forward. There are several proposed chemical inception mechanisms in the literature.

On the other hand, since the NMR experiment, we have observed structural elements that lead to their formation in this thesis work. On the other side, EPR also confirmed its chemical and environmental characteristic.

In this thesis work, a study of DFT has been purposed to move a step forward in understanding such radicals species' behaviour, their reactivity, and their role in the mechanism.

Computational techniques have reached an outstanding level of accuracy. Different sites' reactivity on aromatic molecules can be predicted directly from the ground state electronic structure using chemical reactivity theory (Bulat *et al.*, 2012).

It is known that the thermal stability of aromatic cross-links requires highly accurate energies and hybrid meta-GGA density functional theory such as M06-2X,40 providing bond energies to within a few kcal/mol and transitions states to within 3–7 kcal/mol (Hou and You, 2017; Frenklach *et al.*, 2018; Wang *et al.*, 2018). Moreover, DFT methods with empirical dispersion corrections (DFT-D)

can also study physical interactions in stacked aromatic configurations. However, Totton et al. found that this correction systematically overbinds PAH (Totton et al., 2011b). Then they performed highly accurate benchmark calculations of PAH dimers that quantified and corrected the systematic overbinding (Totton, Misquitta and Kraft, 2012) allowing physical interactions and chemical bonding to be directly compared.

Martin et al. used dispersion corrected density functional methods to study the implications of radicals on rim-based rings, the reactivity of different sites, how thermally stable cross-links formed between these sites were systematically determined from calculating the bond energies between the set of reactive sites (Martin *et al.*, 2019a).

They found geometry optimizations at the B3LYP/6-311G(d,p) level of theory and single point calculations at the M06-2X/ccpVTZ level of theory provide energetics within chemical accuracy for hydrogen abstractions (<1 kcal/mol) (Hou and You, 2017).

In combustion, DFT has proven to be a surprising means to predict the geometries, the reactivity of aromatics, radicals, and predict properties of fundamental importance for the material's characterisation. An example is the optical band gap (OBG) whose values are related to PAHs' specific structures. A hybrid functional that has proved to be a suitable choice for the accuracy of results in the specific prediction of OBG for cross-linked, curved, and radical PAHs systems, has been the HSE06 as studied by Menon et al. (Menon *et al.*, 2019).

In this study, starting from two incipient PAHs visualized through HR-AFM, a functional density study was carried out. Density functional theory DFT-D3 calculations, with hybrid functional and localized Gaussian basis set (B3LYP/6-31G\*\*), was performed to study the interactions of two  $\pi$ -PAH radicals found in the ensemble of soot molecular constituents visualized by HR-AFM (Commodo *et al.*, 2019), named in the following R1 and R2 (IS1 and IS13 in Ref. (Commodo *et al.*, 2019)).

This thesis work showed the application of the DFT-D3 on the structures of single radicals and their dimers (with the formation of cross-linked structures or not) to assess radical aggregation's role on the inception of soot particles. The Mulliken population analysis (MPAN) of the spin density (Mulliken, 1955) helped to understand the effect of radical delocalization on different dimerization pathways. Besides, an analysis of the two different dimerization processes, in terms of binding energy and spectroscopic behaviours (bandgap), has also been performed.

It is not easy to consider absolute values when a study of multi-variational space with many parameters.

This thesis work availed of B3LYP functional use to perform a comparison investigation and trend determination.

Therefore, the choice of B3LYP as functional has been determined by the presence of not a specific system. B3LYP best matches all situations averagely, indeed it is a primary choice and the most used. For instance, the meta GGA also adopted in the works mentioned above (M06, MO6X, ) may work better in some particular systems but lose generality.

Having three different systems (a radical system, a closed shell system that covalently dimerizes, and a stacking one, formed by two radicals that stabilize the triplet state), B3LYP approach very well with reasonable errors, if the study was only on one of these systems, then functional HSE06 or HISS could work better and not overestimate the gap. The same consideration comes for other parameters such as dimerization energy, there is no only choice, but some functional overestimate and others underestimate, it depends on the analyzed systems.

Hence, calculations have been performed using the DFT-D3 approach with a linear combination of atomic orbital (LCAO). All systems are treated with the use of the unrestricted spin-polarized method. The Hamiltonian adopted is the B3LYP global hybrid functional (Becke, 1993) as implemented in the Crystal17 program (Dovesi *et al.*, 2018). All-electron 6-31G\*\* double zeta split valence plus polarization basis set of Gaussian-type functions, centred on the nuclei, has been adopted for C, the number of atomic orbitals spans from 457 to 505 in isolated radical cases and the twice (from 914 to 1010) in the dimer cases.

The asymmetric geometry of the studied compounds produces a C1 point symmetry. The truncation of Coulomb and exchange series is controlled by five thresholds  $T_i$ , which have been set to 8 ( $T_1$ - $T_3$ ), 12 ( $T_4$ ), and 50 ( $T_5$ ), for a correct evaluation of the exchange interactions. The convergence threshold on energy for the self-consistent-field (SCF) procedure has been set to  $10^{-8}$  Hartree for structural optimizations. The convergence criteria of the route mean square (RMS) of the analytical gradient and the displacement were tightened, from the default values of 0.0003 a.u. and 0.0012 a.u. to 0.0001 a.u. and 0.0004 a.u., respectively, to provide accurate geometry optimizations of the final structures. The DFT exchange-correlation contribution to the Fock matrix has been evaluated by numerical integration over the molecular volume. Radial and angular points for the integration grid are generated through Gauss-Legendre radial quadrature and Lebedev two-dimensional angular point distributions. The default pruned grid



XLGRID with 75,974 points (75 radial and 974 angular points) has been increased to a very dense XXLGRID with 991,454 points (99 radial and 1454 angular points), whose accuracy can be measured by comparing the integrated charge density considered  $N_i = 393.9996$  electrons, with the total number of 394 electrons in the molecule. The dispersion interactions are evaluated using the "Grimme" D3 scheme method (Grimme *et al.*, 2016).

The classical dispersion energy is the sum of the DFT energy using a weight function that avoids double counting of the short-range interactions. The electron 3D spatial extension of the electron and spin densities have been calculated to integrate the wave function obtained from SCF calculations in a dense spatial point. All dimerization energies have been reported without considering the counterpoise correction (CC), usually employed to evaluate the basis set superposition error (BSSE). The BSSE energy corrections span from +7 to +8 kcal mol<sup>-1</sup> (as will be reported successively), but they do not change the trends of the dimerization energies. The approach used is not the most accurate if applied to small or medium-size molecules, but it allows performing agile and reliable calculations on moderately large models, as are those investigated in this work, and it is easily extendable to molecules with one thousand atoms and more.

To estimate our results' quality, a specific benchmark, involving small aromatic dimers, has been performed.

B3LYP-D3 method has been applied to a set of dimers of tiny aromatic molecules, to compare the results with very accurate methods. The basis set adopted is 6-31G (d,p) and def2-TZVP. DLPNO-Coupled Cluster Method with Single, Double, and a perturbative estimation of triples excitations have been chosen as reference calculations. In DLPNO-CCSD(T), we have adopted a triple zeta basis set with only one set of polarization functions: def2-TZVPD. The geometries of the dimers were optimized at the B3LYP-D3 level. All the optimized geometries show graphite-like shifts. The results are reported in the following Table 4.2.

Table 4.2. Benchmark for B3LYP-D3 method: stacking interaction energies of dimers in kcal/mol.

	B3LYP-D3/6-31g(d,p)	B3LYP-D3/def2-TZVPD	DLPNO-CCSD(T)/def2-TZVPD
Benzene	-4.36	-3.24	-3.78
Naphthalene	-9.20	-7.38	-8.78
Anthracene	-14.27	-11.71	-14.78

The smaller basis set tends to overestimate the energy interaction, while, to the contrary, the larger basis set yields an equivalent underestimation. Both results are well distributed around the reference method. Based on this benchmark, the obtained data remain confident about the study's semi-quantitative results, where van der Waals interactions are predominant and well represented by the D3 correction. These calculations confirm the excellent calibration of the D3 method for treating dispersion interactions in a cheap but accurate way for DFT methods.

The domain-based local pair natural orbital coupled-cluster method with a single, double, and perturbative estimation of triples excitations -DLPNO-CCSD(T)- has been chosen as a reference method, employing ORCA 4.2.1 software (Neese, 2018). In DLPNO-CCSD(T) calculation, a triple  $\zeta$  basis set with two sets of polarization functions def2-TZVPP has been adopted (P. Pritchard *et al.*, 2019).

#### 4.4.1 MULLIKEN POPULATION ANALYSIS

For extensive and complex molecular systems, clear discrimination between the two types of radicals, i.e.,  $\sigma$  and  $\pi$  radical, may not be a trivial task. In these cases, a helpful way to differentiate between the two kinds of radicals is to use the Mulliken population analysis (MPAN) of the spin density, i.e., the electron density of the free electrons (Mulliken, 1955). MPAN investigates the distribution of electronic spin within a system. To this end, the spin-up ( $\alpha$ ) and spin down ( $\beta$ ) electronic populations are analyzed separately, and their sums ( $\alpha+\beta$ ) and differences ( $\alpha-\beta$ ) are evaluated to yield the charges and net spins of the system, respectively. Such analysis is constructive in providing where the unpaired electron is located for an assigned molecular structure. Although the MPAN

determination of the spin density suffers from some degree of inaccuracy that arises from the equal division of the off-diagonal terms in the matrices ( $P \cdot S$ ), it offers acceptable results for a comparison perspective, especially in these covalent systems. In  $\sigma$ -aromatic radical, the spin population is concentrated almost totally, more than 92%, on the carbon atom close to the dangling bond (an atom with an unsatisfied valence). For the  $\pi$ -aromatic radical, the spin population is distributed over the carbon rings (in alternate topology), and the maximum localization over single carbon atoms does not exceed 35–40%.

## CHAPTER 5: RESULTS

In this chapter, the main results obtained in this PhD-thesis work will be reported. Five paragraphs will compose the chapter; each of them deals with a different experimental approach.

### 5.1 STUDY OF CARBON NANOPARTICLES EVOLUTION IN A LAMINAR PREMIXED FLAME. THE ROLE OF RADICALS IN CARBON CLUSTERING AND SOOT INCEPTION.

A first experimental approach of this PhD thesis work involved the study of flame carbon nanoparticles evolution with residence time.

Notably, great attention has been focused on the radicals present in the flame. The investigation involved a study on radicals and their behaviour in the flame at different residence times. This study has been performed by EPR and Raman measurements of particles collected in an ethylene-rich premixed flame at various residence times during nucleation. Combined analysis of these experimental results, together with the measurement of the particle size distribution (PSD) by a differential mobility analyzer, sheds light on radicals' role in particle nucleation and rearrangement of aromatic molecules in just-nucleated particles.

As written in the Experimental section, in Chapter 3, the evolution of carbon nanoparticles was investigated in a premixed laminar ethylene–air flame stabilized on a water-cooled sintered bronze McKenna burner; ethylene was chosen as fuel because it is one of the main decomposition products of any hydrocarbon. The cold gas stream velocity was 9.8 cm/s, and the carbon-to-oxygen atomic ratio ( $C/O$ ) was set to 0.67, which corresponds to a flame equivalence ratio ( $\Phi$ ) of 2.01. The maximum flame temperature of  $1715 \pm 50$  K was determined by rapid-insertion thermocouple measurements and reached at a distance from the burner approximately 3 mm.

The flame products were sampled using a horizontal the tubular probe with a downward orifice with an inner diameter = 0.2 mm for the DMA analysis and another probe with an inner diameter = 0.3 mm for collecting particles on filters for Raman and EPR characterization. The sampled flow entering the probe was immediately mixed to a turbulent  $N_2$  diluent flow.

For the DMA analysis the probe was thoroughly cleaned before each run, although, under the selected flame conditions, the probe orifice was not very clogged by material soot deposit.

The same sampling system was used to convey particles on-line to both an electrical mobility spectrometer and a quartz filter (Whatman QM-A Quartz Microfiber Filters, with a diameter of 47 mm) in a filter holder.

### 5.1.1 SIZE DISTRIBUTION

Figure 5.1 shows the PSDs measured along with the flame at increasing HAB and normalized to the total detected particles. In the early zone of the post-flame region, i.e., HAB = 7 mm, most particle sizes, expressed in terms of the mobility diameter, are less than 4 nm, and the number concentration of particles is monomodal, with a modal value between 2 and 3 nm. This mode, named Mode I, produces the first detectable particles and is usually referred to as the nucleation mode (Maricq, 2004; Sgro *et al.*, 2009; Commодо, De Falco, *et al.*, 2015; De Falco *et al.*, 2015; Carbone, Attoui and Gomez, 2016; Desgroux *et al.*, 2017).

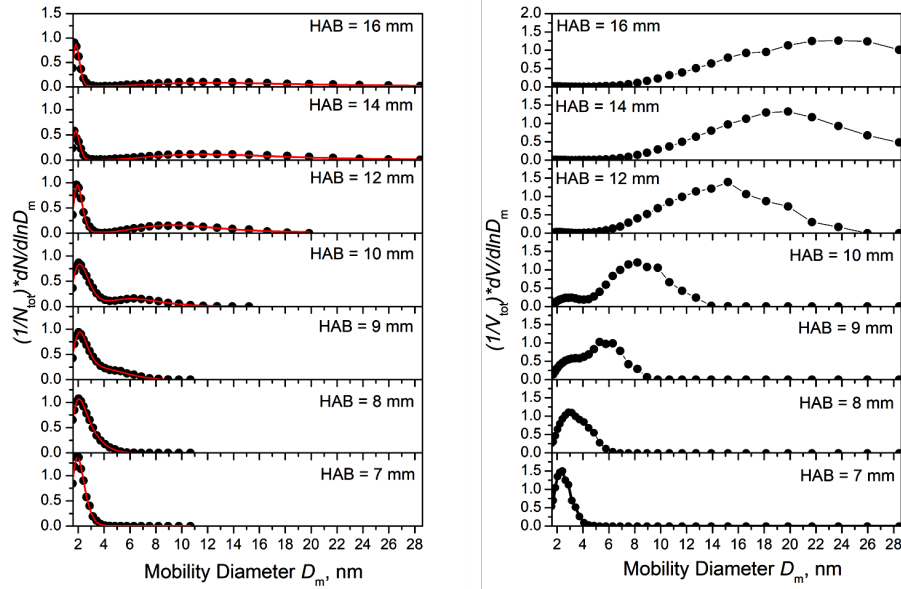


Figure 5.1: Evolution of PSD as a function of HAB. Left: normalized number PSD ( $1/N_{tot} * dN/d\log D$ ); right: normalized volume PSD ( $1/V_{tot} * dV/d\log D$ ). Red lines are fits to data using a bi-lognormal distribution function.

At 8 mm, i.e., just a few milliseconds later (corresponding approximately to 2 ms per each millimetre in this flame condition) a second mode, named Mode II, start to become evident especially in volume PSD on the right side of Figure 5.1. Their presence is evident at 9 mm, where the bimodal number and volume PSDs are measured.

The number PSDs were fitted with a bi-lognormal distribution function, from which the mean diameters and percentage contributions of the two-particle modes were calculated. As shown in Figure 5.2.a, the mean diameter of Mode I particles remains roughly constant along with the flame, whereas the mean diameter of Mode II particles is approximately 4 nm when they first appear and increases to approximately 15 nm as particles are collected at high HABs. Figure 5.2.b shows Mode I and Mode II's evolution regarding volume percentages concerning the total volume of collected particles. At a HAB of approximately 9 mm, Mode II's contribution starts to dominate. At higher flame heights, most of the carbon material consists of Mode II particles.

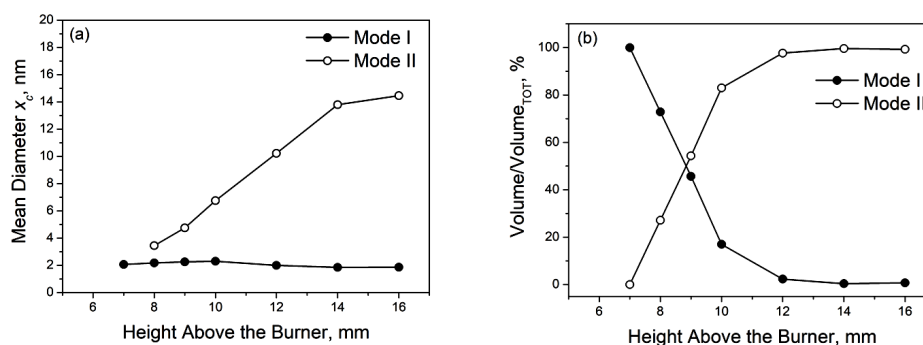


Figure 5.2: Mean mobility diameters of Mode I and Mode II obtained from the bi-lognormal distribution functions used to fit the number PSD (a) and percentage ratio of the two modes' particle volume concerning the total particle volume (b).

### 5.1.2 EPR AND RAMAN SPECTROSCOPY

Particles collected on the quartz microfiber filter were characterized off-line by EPR and Raman spectroscopy. The total sampling time for each quartz filter was about seven hours. During that sampling time, the dilution condition, flame stability, cooling temperature, and gas flow rates were carefully controlled.

EPR analysis were performed in collaboration with Dr. Giuseppe Vitiello of the “Dipartimento di Ingegneria Chimica, dei Materiali e della Produzione Industriale”, Università degli Studi Di Napoli Federico II”.

EPR spectroscopy of the sampled material was performed using an X-band (9 GHz) Bruker Elexsys E-500 spectrometer (Rheinstetten, Germany) equipped with an ultrasensitive probe head. A defined section (1 cm × 0.5 cm) of the quartz filter was co-axially inserted into a standard 8 mm quartz sample EPR tube to record measurements at 25 °C. The instrumental settings were as follows: sweep width, 100 G; resolution, 1024 points; modulation frequency, 100 kHz; modulation amplitude, 1.0 G. EPR spectra were recorded at an attenuation value of 20 dB, and 128 scans were accumulated to improve the signal-to-noise ratio. Power saturation curves were also recorded by varying the microwave power from 0.004 to 128 mW. For each sample, 12 spectra obtained at different incident powers were collected.

In some cases, at low powers, the signal intensity was too weak to be distinguished from the spectral noise. The *g*-factor and spin-density values were evaluated using an internal standard consisting of Mg<sup>2+</sup>/MnO powder (Yordanov and Lubenova, 2000), inserted in quartz tube co-axially with the analyzed samples. The EPR spectra were quantitatively analyzed by determining the signal line width,  $\Delta B$ , measured as the peak-to-peak distance of the first-derivative signal (instrumental output), and the Gaussian and Lorentzian contributions to the line shape were determined by estimating the  $\Delta B_{1/2}/\Delta B$  ratio, where  $\Delta B_{1/2}$  is the half-height width of the EPR absorption signal. In all the cases examined in this work, the line shape features were estimated and reported as percentages of the Lorentzian peaks (Requejo *et al.*, 1992).

Figure 5.3 shows EPR spectra and Table 5.1 reports and the corresponding spectral parameters. All the spectra show a single peak at *g* factors of 2.0025–2.0028 ( $\pm 0.0003$ ).

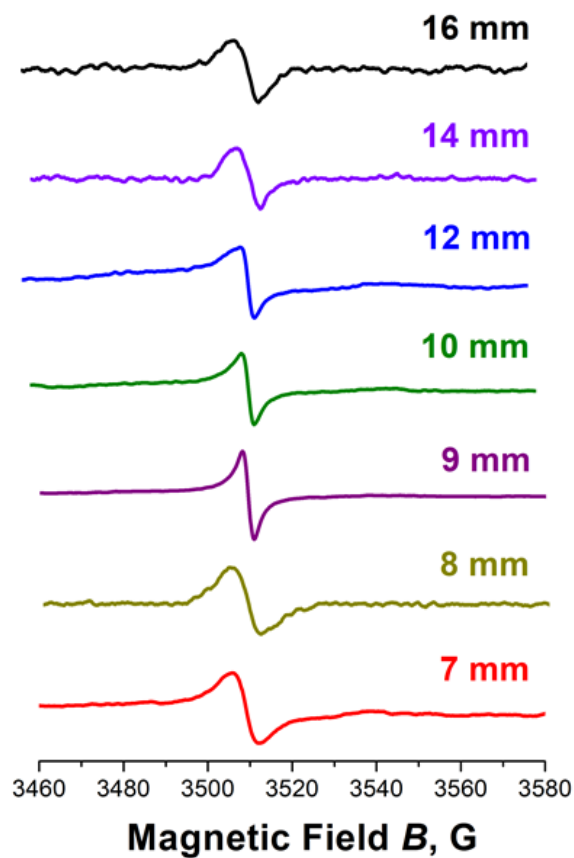


Figure 5.3: EPR spectra of flame-formed nanoparticles at the different mean diameter of particles

Table 5.1: EPR spectral parameters of flame-formed nanoparticles. The standard deviation of three measurements of each sample is  $\pm 0.0003$  for the  $g$  factor,  $\pm 10\%$  for the spin density,  $\pm 0.2$  G for  $\Delta B$ , and  $\pm 5\%$  for the line shape analysis values.

HAB (mm)	spin density (spin/g)	$g$ factor	$\Delta B$ (G)	% Lorentzian
7	$1.8 \times 10^{18}$	2.0028	6.5	15
8	$4.5 \times 10^{16}$	2.0027	7.6	38
9	$4.5 \times 10^{18}$	2.0025	2.8	95
10	$9.2 \times 10^{18}$	2.0025	3.1	94
12	$1.8 \times 10^{18}$	2.0026	3.6	92
14	$3.8 \times 10^{17}$	2.0027	6.2	28
16	$2.2 \times 10^{17}$	2.0025	6.5	15



The  $g$  factor reflects the interaction between the spin motion and orbital motion of electrons in the paramagnetic centre. It is determined by the chemical environments of unpaired electrons and is used to characterize interior molecular structures. The values obtained for all the samples, which are slightly higher than the typical  $g$  factors of free electrons (2.0023), are typical of persistent carbon-centred aromatic radicals (Valavanidis *et al.*, 2008).

Interestingly, the EPR spectra in Figure 5.3 exhibit different line widths depending on the HAB (Table 5.1), suggesting a change in the paramagnetic signal along with the flame.

At lower heights, HAB = 7 and 8 mm, EPR reveals significantly broader signals with a lower signal/noise ratio than those recorded at HABs between 9 and 12 mm. At higher HABs, the signal broadens again. The line width of EPR peaks generally reflects the relaxation time of spinning electrons and is affected primarily by the unresolved hyperfine interaction between unpaired electrons with neighbouring atoms (Buszman *et al.*, 2006).

The presence and superposition of multiple paramagnetic species in the particles generate a broad line shape (Valavanidis *et al.*, 2008; de Boer, 2010; Herring *et al.*, 2013).

Conversely, a narrow line shape is associated with the presence of stronger electron-electron interactions (Ingram, 1961) and can be associated with a more locally ordered organization of the aromatic structures hosting unpaired electrons. Such exchange narrowing interactions are produced by the increased overlap of the wave functions and can result from greater delocalization of unpaired electrons or the stacking tendency of aromatic functional groups hosting free radicals.

The signals of samples with an increase in incident microwave power were recorded to extend the EPR analysis. The obtained power saturation curves are shown in Figure 5.4, where the peak amplitude normalized for the spin concentration,  $A$ , is plotted as a function of the square root of the microwave power,  $P$ . A decrease in amplitude at higher microwave powers is expected if free radicals with long relaxation times are homogeneously distributed in the sample (de Boer, 2010). This behaviour is not observed in the profiles shown in Figure 5.4, which instead show a monotonic increase, indicating that the free radical spins do not all exhibit the same relaxation behaviour. This finding indicates that the radical centres have an inhomogeneous distribution, which may be both chemical and spatial, depending on the presence of different aromatic moieties containing unpaired electrons and a non-uniform supramolecular organization the aromatic molecules forming the particles, respectively. Because the spins do not interact,

they saturate independently, and the saturation curve does not show a maximum. The power saturation curves of the samples at lower (7 mm) and higher (10 and 14 mm) HABs show behaviour typical of extensive inhomogeneous saturation (Eaton *et al.*, 2010). However, a different profile is observed for the sample at 9 mm, which shows a quasilinear tendency, indicating less saturation. This evidence suggests peculiar behaviour of the aromatic structures bearing unpaired electrons at this burner height, implying reduced inhomogeneity in the spin system (Joly *et al.*, 2010).

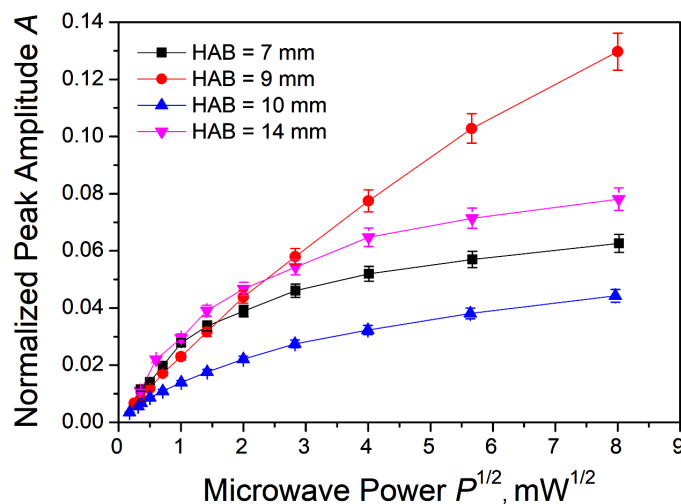


Figure 5.4: Power saturation profiles at different HABs. Error bars show the estimated error of the amplitude values of approximately  $\pm 5\%$ .

More in-depth insight into the factors influencing the EPR signal's narrowing in Figure 5.4 and the power saturation profile is obtained by determining the Lorentzian and Gaussian contributions to the recorded spectra's line shape. Specifically, the relative intensity (percentage) of a narrow Lorentzian concerning the total intensity of the EPR spectrum is listed in Table 5.1.

The Gaussian line shape prevails for samples at lower (7 and 8 mm) HABs, showing a broader line shape (see values of  $\Delta B$  in Table 5.1). These findings indicate that various non-interacting spin systems are present in the polyaromatic structures. Indeed, the Gaussian line shape and high  $\Delta B$  are consistent with attribution of these EPR signals to exchange interactions of edge-localized nonbonding  $\pi$ -electrons, as observed in a recent EPR investigation of graphene fragments (Ćirić *et al.*, 2009).

A high Lorentzian contribution, associated with a low  $\Delta B$  value, characterizes the samples' signals at 9–12 mm. These properties are consistent with the presence of delocalized  $\pi$ -electrons, as indicated by EPR (Singer *et al.*, 1987; Pilawa *et al.*, 2005). Another possible contribution to the narrowing of the line shape could be related to stacking interactions between flat conjugated structures hosting unpaired electrons, as observed in asphaltenes (Requejo *et al.*, 1992; Calemme *et al.*, 1995). Indeed, stacking would cause overlapping of adjacent radicals' electronic wave functions, promoting electron exchange, which would lead to line narrowing (Binet *et al.*, 2002).

A more in-depth analysis of Figure 5.3 reveals that the EPR spectrum at HAB = 12 mm shows a superposition of two signals due to the coexistence of a narrower peak (like that observed at 9 and 10 mm) with a broader one, as indicated by the flaring of the semi-peak at low field values. At higher HABs (>12 mm), in flame zones where particles larger than 10 nm are predominant in terms of mass, the line shape of the EPR signal becomes very broad, as confirmed by the increase in  $\Delta B$ , showing slight asymmetry and a predominantly Gaussian nature. In this case, this new source of inhomogeneous line broadening is probably associated with the different structural organization, which affects the paramagnetic centres' interaction. This effect might be due to the new spatial distribution of spin centres produced by particle-particle aggregation and the persistent nucleation of new particles with highly localized nonbonding  $\pi$ -electrons.

The spin density was calculated using the total mass of particles collected on the filter, which was evaluated in terms of the particle concentration in the flame measured by the DMA, the N<sub>2</sub> diluent flow rate and dilution ratio, the total sampling time, and the size of the filter section inserted in the EPR tube. A simpler procedure would have been to weigh the filters before and after sampling, but unfortunately the material sampled on the filter fell within the error of the analytical balance and therefore not very reliable.

Higher spin-density values are obtained for the samples with higher Lorentzian contributions and lower  $\Delta B$  values (9–12 mm), indicating the enhanced formation of radical centres during the early stages of Mode II particle formation. This evidence supports the hypothesis that delocalized  $\pi$ -radicals may play a role in forming Mode II particles.

Raman spectra of all the samples were measured to clarify the structural changes in the particles that are responsible for the trend in the EPR signal.

Figure 5.5 shows Raman spectra acquired using two different wavelengths, i.e.,  $\lambda = 532$  nm and  $\lambda = 785$  nm, and Figure 5.6 shows the spectra at 1000–3500

$\text{cm}^{-1}$ , reported only those acquired at  $\lambda = 532$ . All the spectra were baseline corrected, by subtracting the background using a linear interpolation, and normalized to the maximum of the G peak.

Between 1000 and 2000  $\text{cm}^{-1}$ , the spectra consist of the typical D and G bands of carbon materials centred at approximately 1350 and 1600  $\text{cm}^{-1}$ , respectively. At 2300–3300  $\text{cm}^{-1}$ , the spectrum consists of second-order and combination bands.

Activation of the Raman D mode, at  $\sim 1350 \text{ cm}^{-1}$ , is due to defects in the  $\text{sp}^2$  aromatic network, prohibited in the perfect hexagonal lattice (Ferrari and Basko, 2013). Conversely, at  $\sim 1600 \text{ cm}^{-1}$ , the G band is due to every  $\text{sp}^2$  bond and is mostly insensitive to defects. These bands change in width and position of the maximum as a function of the different carbon structures. It is worth noticing that spectra show other Raman features as weak shoulders of D and G bands. The spectra's significant differences consist of changes in the D and G peaks' relative intensity and the band's position.

About relative intensity, at  $\lambda = 785 \text{ nm}$ , the D band intensity is more significant than G band one. The dependence of the  $I(\text{D})/I(\text{G})$  ratio on the photon energy of the excitation beam is caused by a deviation of the D band intensity from the dependence predicted by the Raman scattering. Unlike G, the D band is susceptible to the resonance Raman effect, and the transition probability shows a significant dependence on laser excitation energy.

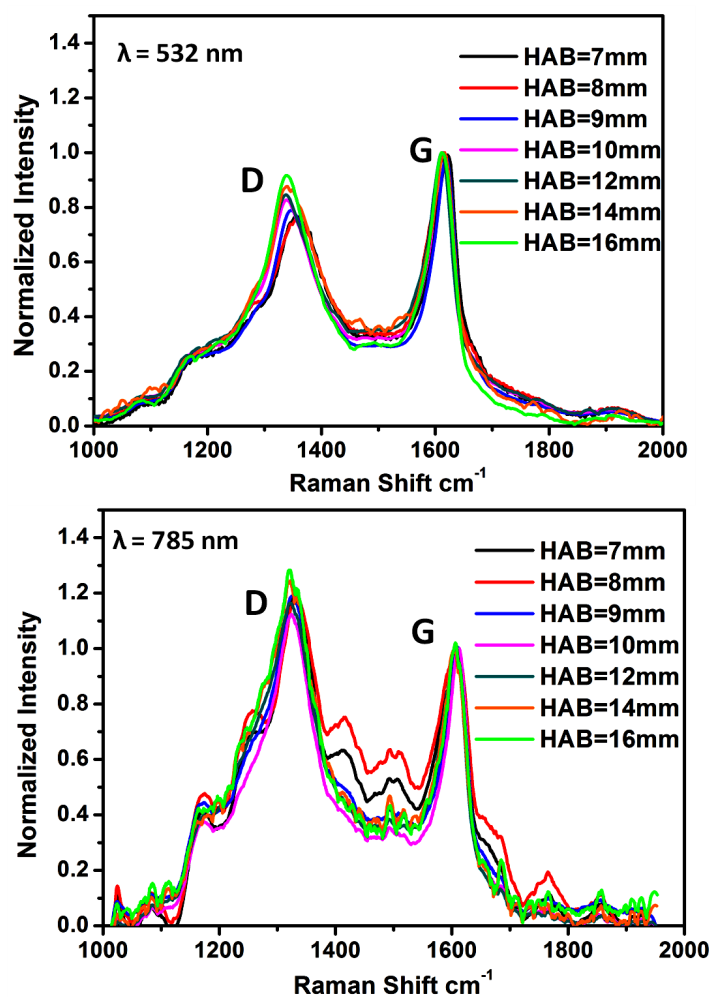


Figure 5.5: Raman spectra at several heights above the burner. On the top, collected spectra at  $\lambda=532 \text{ nm}$ ; on the bottom, collected spectra at  $\lambda=785 \text{ nm}$ . The Raman spectra have been normalized on the G peak after subtracting the photoluminescence background

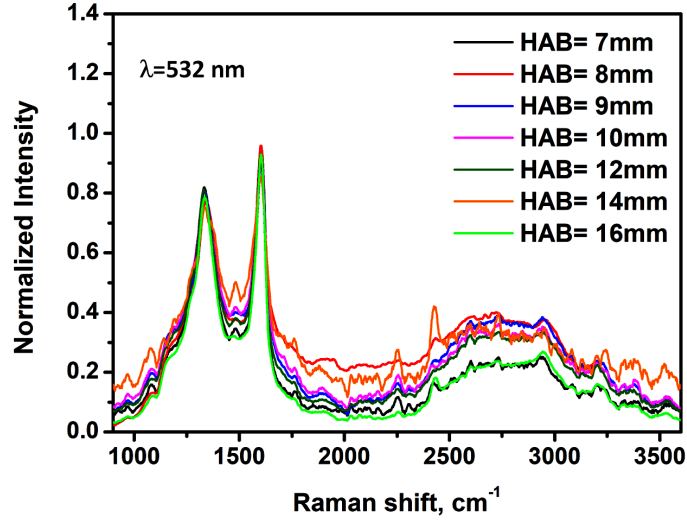


Figure 5.6: Raman spectra, including the second-order, normalized to the G peak at different HABs.

It is well known that the  $I(D)/I(G)$  ratio is related to the average size of the aromatic units or clusters forming the carbon materials,  $L_a$  (Ferrari and Robertson, 2001). For graphite and nano-graphite, the intensity ratio  $I(D)/I(G)$  is inversely proportional to  $L_a$  (Tuinstra and Koenig, 1970). Such functional dependence has been successively verified up to a minimum  $L_a$ , of about 2-3 nm, where  $I(D)/I(G)$  reaches a maximum value (Ferrari and Robertson, 2001). When  $L_a$  further decreases,  $I(D)/I(G)$  decreases to zero. For flame-generated soot particles, the low- $L_a$  regime, i.e.,  $L_a < 2-3$  nm, usually applies, for which the following empirical expression has been found to correlate  $L_a$  with the relative intensity of the Raman bands (Ferrari and Basko, 2013):

$$L_a^2(\text{nm}^2) = 5.4 \cdot 10^{-2} \cdot E_L^4(\text{eV}^4) \frac{I(D)}{I(G)} \quad (5.1)$$

Where  $E_L$  is the energy of the incident photon.

It is relevant to note that using excitation wavelength in the visible, about 532 nm, the dependency of  $I(D)/I(G)$  on  $L_a$  (Eq. 1) has been validated for a large variety of disordered carbon by many investigations (Ferrari and Basko, 2013) and the evaluation of  $L_a$  can be considered reliable. The results obtained for the different

soot particles, reported in Figure 5.7, show a slight increase of  $L_a$  as a function of HAB. This trend is an indication of larger aromatic islands inside particles at increasing residence time.  $L_a$  is approximately 1.1 nm for particles lower in the flame and increases slightly at HABs above 9 mm, reaching 1.2 nm.

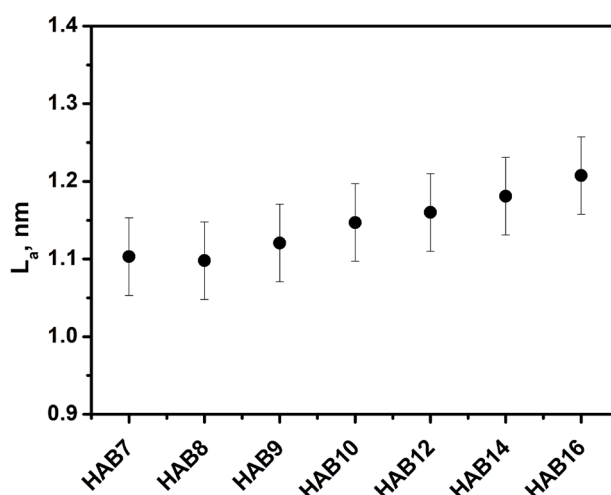


Figure 5.7:  $L_a$  from the Raman spectra of particles collected at several HABs

These aromatic molecules making up the particles can be viewed as small nanographene sheets containing both zigzag and armchair edges. The zigzag edge region's presence is exciting because it is a source of localized edge-state spins (Joly *et al.*, 2010) even in structures with edge shapes having small zigzag sequences fragmented by armchair sites (Nakada *et al.*, 1996). These two types of edges can be monitored by Raman spectroscopy because the D band is resonantly activated by armchair edges and not by zigzag edges, whereas both types of edges can activate the D' band, which appears at approximately  $1620\text{ cm}^{-1}$  (Cançado *et al.*, 2004).

In the analyzed spectra, owing to a line broadening of all the Raman features, the D' band (not visible in Figure 5.5) is superimposed on the G band, and a single peak appears at  $1600\text{ cm}^{-1}$ . As reported in detail elsewhere (Minutolo *et al.*, 2014), to separate all the bands' contributions, the first-order Raman spectra were fitted with Lorentzian and Gaussian's superposition functions using a procedure similar to that employed by Sadezky *et al.* (Sadezky *et al.*, 2005). Specifically, three Lorentzian curves were used to fit the D, G, and D' peaks; two additional Lorentzian lines were used to fit the features at  $1100\text{--}1300\text{ cm}^{-1}$ : a peak at  $1220$

$\text{cm}^{-1}$  due to finite-crystal-size effects and defects (Sadezky *et al.*, 2005) and an extra peak at approximately  $1175 \text{ cm}^{-1}$  attributed to olefinic C=C bonds, which have higher vibration frequencies than aromatic ones (Ferrari and Robertson, 2001a). A Gaussian line shape was chosen for the band at approximately  $1530 \text{ cm}^{-1}$ , between the D and G bands (Jawhari, Roid and Casado, 1995; Sadezky *et al.*, 2005).

Figure 5.8 shows the ratio between the areas of the D and D' peaks,  $A(D)/A(D')$ , as a function of the HAB. According to the above discussion, this quantity can indicate armchair edges' fractional composition concerning the armchair's total number and zigzag edges. The low ratio measured in the flame's initial zone indicates more zigzag edges in the compounds in this flame zone. Zigzag edges are a source of localized edge-state spins and can be one of the EPR signal sources measured at low HAB.

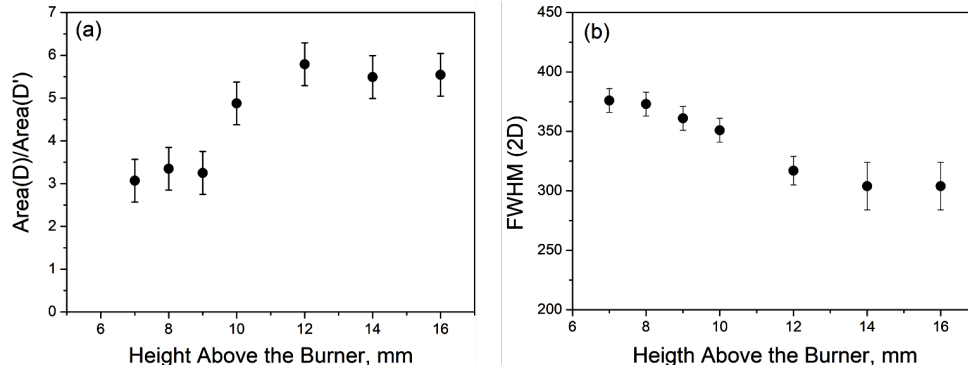


Figure 5.8: (a) Ratio between the areas of the D and D' peaks and (b) full width at half-maximum (FWHM) of the 2D peak as a function of HAB.

Another exciting feature in the Raman spectra is the bandwidth of the 2D line, which is the bump at approximately  $2700 \text{ cm}^{-1}$  in Figure 5.6. Several studies have shown that as the number of layers increases from graphene to multilayer graphene, the 2D band changes from a single line to multiple (Ferrari *et al.*, 2006; Cançado *et al.*, 2008). Besides, a single line, which becomes broader with an increase in interlayer spacing, is measured for a turbostratic arrangement of graphitic layers (Lespade *et al.*, 1984). A correlation between the broadening of the 2D band and the  $d_{002}$  interlayer distance measured by X-ray techniques was, indeed, reported by Lespade *et al.* (Lespade *et al.*, 1984), who therefore identified the full width at half-maximum of this band, FWHM (2D), as a helpful index of three-dimensional graphitization (ordering) of carbons. FWHM (2D) was



determined by fitting the Raman spectra's second-order features at different HABs with a superposition of four Lorentzian peak functions, as described in detail elsewhere (Sadezky *et al.*, 2005; Minutolo *et al.*, 2014). Specifically, the D band's second-order features and the peak at  $1220\text{ cm}^{-1}$  are located at approximately  $2450$  and  $2700\text{ cm}^{-1}$ , respectively, and two different lines at approximately  $2950$  and  $3200\text{ cm}^{-1}$  are produced by overtones and combinations of the D, G, and D' bands. FWHM (2D) is reported as a function of the HAB in Figure 5.8 b. Although all the values are larger than those reported for graphitized materials by Lespade *et al.* (Lespade *et al.*, 1984), the reduction of FWHM (2D) indicates an increase in the interlayer interaction at HABs larger than  $8\text{ mm}$ , and hence an increase in the three-dimensional/stacking order of the aromatic planes.

As discussed previously, the formation of stacks of aromatic components and three-dimensional-network-generated spin-spin interactions between stacked aromatic planes (Joly *et al.*, 2010) may explain the narrowing of the EPR signal observed at HAB =  $9$  and  $10\text{ mm}$  and the predominance of the Lorentzian line shape. The trend observed here is very similar to the evolution from two-dimensional nanographene to a three-dimensional nano graphite system described by Enoki (Enoki, 2012).

At HABs of  $12\text{ mm}$  and larger, where most of condensed phase material is in the form of particles larger than  $10\text{ nm}$ , the Raman spectra are characterized by a shift in the line centres, as shown in Figure 5.9. The shift is more significant for the D and 2D bands (not shown), but the G band also exhibits a slight shift. As suggested by studies of strained graphene (Popov and Lambin, 2013), this effect can be attributed to strain and deformation in the graphitic lattice, possibly owing to interactions between nano graphite domains in particles. The increase in structural disorder within particles is also demonstrated by the extensive line shape of all the Raman peaks and the entire second-order Raman spectrum's reduced intensity.

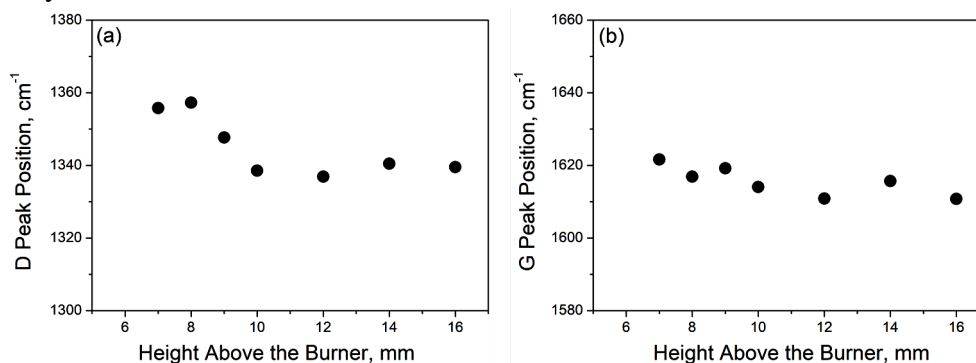


Figure 5.9: Positions of (a) the D peak and (b) the G peak as a HAB function.

## 5.2 SOOT INCEPTION: A DFT STUDY OF $\sigma$ AND $\pi$ DIMERIZATION OF RESONANTLY STABILIZED AROMATIC RADICALS

Research on nucleation and radicals' role within the formation and evolution of soot in the flame has progressed with a theoretical study.

In this second paragraph, Density Functional Theory (DFT) calculation, in collaboration with Dr Francesco Silvio Gentile and Prof. Causà of “Dipartimento di Scienze Chimiche - Università degli Studi di Napoli Federico II,” was performed.

The results of DFT calculation on two molecules visualized from a previous study of Professor D’Anna research group at HR- AFM (Commodo *et al.*, 2019; Schulz *et al.*, 2019) are reported.

Specifically, the image showed several PAHs, including some radical ones. From the visualized PAHs, two of them have been chosen to be studied. As mentioned in chapter 3, the investigation aimed to highlight different types of radicals  $\sigma$  or  $\pi$  their formation based on specific structural elements.

It is well known that in the nucleation phase, the most stable individual molecules are organized in peri-condensed systems. In addition to the purely benzenoid PAHs, five-member rings are also present, and they seem to have a controlling role in the formation and growth of aromatic. These five-membered rings together with a remarkable number of PAHs containing pentagonal rings or even six-membered rings with methylene groups were detected by the use of high-resolution atomic force microscopy (HR-AFM) (Commodo *et al.*, 2019; Schulz *et al.*, 2019).

Radicals can be classified as  $\pi$  or  $\sigma$ , according to whether the spin-bearing orbital is of  $\pi$  or  $\sigma$  type.  $\pi$  Radicals, particularly those with a comprehensive  $\pi$  system, are thermodynamically more stable than their  $\sigma$  counterparts, and so most studied radicals are  $\pi$ . However, more relevant to radicals' lifetime than their thermodynamic stability is their kinetic stability (or persistence). Persistent radicals (Griller and Ingold, 1976) are often sterically protected so that dimerization and other reactions with paramagnetic or diamagnetic molecules are impeded.

The presence of different structural elements leads to the formation of a different type of radical, as shown in Figure 5.10, which occurs in different paths of the formation process.

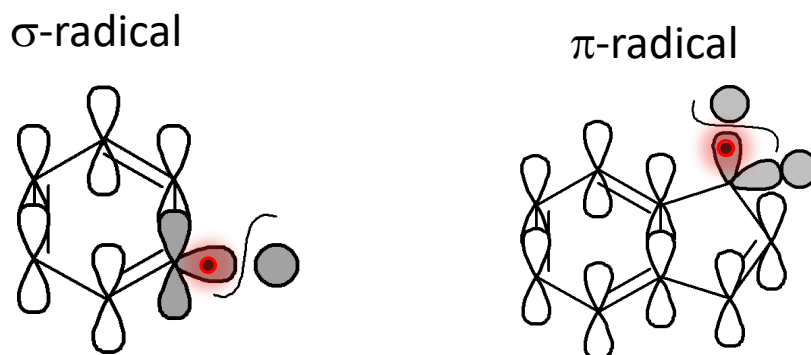


Figure 5.10. Representation of  $\sigma$ -radical and  $\pi$ -radical. The black dot in the red circle illustrates the unpaired electron.  $\sigma$ -radicals present the electron in orbital in the molecule plane;  $\pi$ -radical shows the electron in the orbital perpendicular to the molecule.

As previously written, H atom abstraction to  $-\text{CH}_2-$  of the partially protonated rim-based pentagonal rings or H atom addition to acenaphthylene-type cyclopenta rings form delocalized  $\pi$  radicals. Indeed, if an H atom is removed from the aromatic molecule composed of purely benzenoid rings, the unpaired electron occupies an orbital lying in the local molecular framework plane, forming a  $\sigma$  radical. Conversely, if an H atom is removed from an  $\text{sp}^3$  hybridized carbon at the periphery of an aromatic molecule, such as a  $-\text{CH}_2-$  group in a five-membered or six-membered ring of a PAH, or an H atom is added to an unsaturated ring, the unpaired electron occupies an orbital perpendicular to the local molecular framework, thus forming a  $\pi$  radical which delocalizes over the entire molecule (Howard, 1991).

Unpaired electrons in orbitals lying in the plane ( $\sigma$  radicals) cannot be delocalized on the aromatic system: it is the case of phenyl radical. These  $\sigma$  radicals undergo sequential reactions of acetylene addition, leading to more aromatics (Frenklach, Schuetz and Ping, 2005). The self-combination of these types of radicals forms bi-phenyl-like, cross-linked compounds (D'Anna et al., 2001).

An unpaired electron located in an orbital perpendicular to the plane,  $\pi$  radical, can be delocalized through the entire molecule and stabilizes by resonance. Besides, to be critical for forming the first aromatic ring (Miller and Melius, 1992), the resonantly stabilized  $\pi$  radicals have long been considered essential species in promoting soot nucleation and growth (Homann and Wagner, 1967; Keller, Kovacs and Homann, 2000).

Therefore, it has been speculated that resonantly stabilized  $\pi$  radicals, mainly due to partially protonated rim-based pentagonal rings, might be involved in the nucleation/clustering of aromatics, promoting bridging reactions (Martin *et al.*, 2019b; Frenklach and Mebel, 2020), to form three-dimensional carbon structures. The role of resonantly stabilized radicals in aromatic growth and soot inception was already hypothesized by D'Anna *et al.* (D'Anna *et al.*, 2000).

Aromatic radicals are known to play a fundamental role in numerous branches of organic chemistry; one of the most investigated aromatic  $\pi$  radical compound, the phenalenyl radical, has been found to form a  $\pi$ -stacking intermolecular attraction, sometimes referred to as "pancake bond" or "multi-electron/multi-centre (me/mc)" consisting on an unusual delocalized covalent-like bond (Gao *et al.*, 2016; Kertesz, 2019).

In this section of this thesis work, the dimerization process of chosen PAH molecules and radicals has been studied.

As written in the experimental chapters DFT-D3 calculations have been carried with hybrid functional and localized Gaussian basis set (B3LYP/6-31G\*\*), to study the interactions of the two  $\pi$ -PAH radicals visualized by HR-AFM (Commodo *et al.*, 2019), named in the following R1 and R2 (IS1 and IS13 in Ref. (Commodo *et al.*, 2019)).

The study aims to calculate the DFT-D3 structures of single radicals and their dimers to assess radical aggregation's role in the inception of soot particles. The Mulliken population analysis (MPAN) of the spin density (Mulliken, 1955) has been used to understand the effect of radical delocalization on different dimerization pathways. An analysis of the two different dimerization processes, in terms of binding energy and spectroscopic behaviours (bandgap), has been performed.

### 5.2.1 PHENALENYL RADICAL

Examples of highly persistent neutral hydrocarbon radicals without protecting groups are phenalenyl and its derivatives. The phenalenyl radical, which can be detected in pyrolysis products of petrol fractions ("Proceedings of the Chemical Society. April 1961," 1961), can be formed merely by exposing a solution of phenalene in tetrachloromethane to air, whereby an H atom is abstracted by dioxygen (Figure 5.11) (Sogo, Nakazaki and Calvin, 1957).

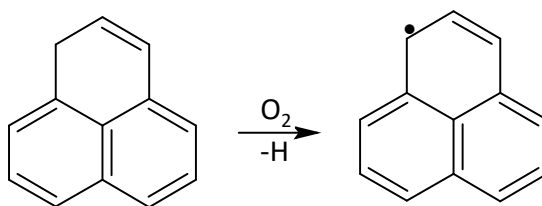


Figure 5.11: Production of Phenalenyl radical. (Sogo, Nakazaki and Calvin, 1957)

Because of their low stability and high reactivity,  $\sigma$  radicals are less easy to detect; however, a few simple, essential species, whose pictures in Figure 5.12, have to be mentioned. These are vinyl, generated from liquid ethane by 2.8 MeV electrons (Fessenden and Schuler, 1963) or by photolysis of HI in acetylene (Adrian, Cochran and Bowers, 1972); phenyl, obtained from stable iodide in a matrix by reaction with sodium (Bennett, Mile and Thomas, 1965) or photolysis (Kasai, Hedaya and Whipple, 1969) or from bromide by 2.8 MeV electrons in aqueous solution (Zemel and Fessenden, 1975); and formyl, first produced by photolysis of HI in solid CO (Cochran, Adrian and Bowers, 1962) or by photolysis of solid formaldehyde (Brivati, Keen and Symons, 1962).

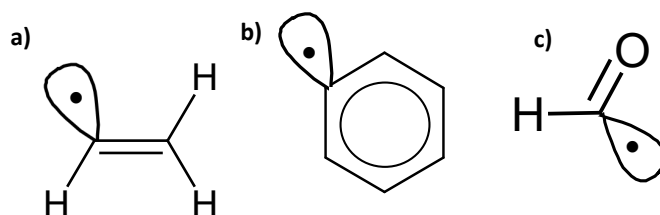


Figure 5.12: Picture of a) vinyl radical(Fessenden and Schuler, 1963); b) phenyl radical (Bennett, Mile and Thomas, 1965); c) formyl radical (Adrian, Cochran and Bowers, 1972)l.

Therefore the first step in conducting this research was to perform preliminary calculations on the phenalenyl radical self-combination, a mechanism that has mainly been studied in the literature. These preliminary calculations are performed to test the used approach's capability to reproduce previous theoretical and experimental studies.

Phenalenyl, sketched in Figure 5.13, is a  $\pi$  radical and confirmed by spin MPAN: 31% of spin density on the equivalent peripheral carbon atoms; 15% on the semi-peripheral Carbon atoms; 7% at the central site.

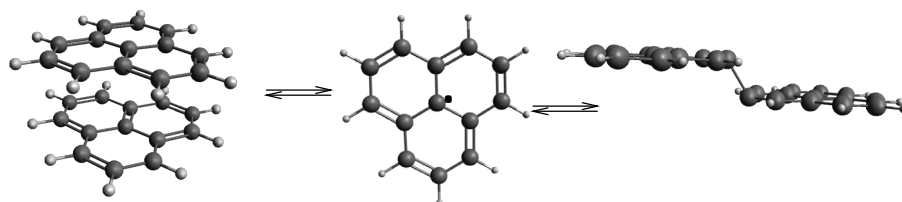


Figure 5.13. Scheme of phenalenyl radical dimerization.

This radical's peculiarity lies in its self-combination capability by forming two types of dimers:  $\sigma$ - and  $\pi$ -dimer. The  $\sigma$ -dimer shows a single C-C bond between the two radicals' peripheral carbon atoms; the two molecules do not overlap, as shown in Figure 5.13 (right side). The dimerization energy is 12.9 kcal mol<sup>-1</sup>, calculated concerning the two separated phenalenyl radicals in reasonable agreement with literature data, 10 kcal mol<sup>-1</sup> (Small *et al.*, 2005). The  $\pi$ -dimer has two different configurations: in the first one, the two radicals exactly overlap whereas, in the second configuration, shown in Figure 5.13 left side, the two radicals present an inversion centre (head-tail configuration) and a shift of the polycyclic aromatic rings giving a staggered "graphite" like structure. Our calculations show the perfectly overlapped stacking dimer to be 13.6 kcal mol<sup>-1</sup> more stable than the monomers in unrestricted open-shell singlet electronic configuration and 9.7 kcal mol<sup>-1</sup> in the triplet state. The  $\pi$ -dimer in the head-tail graphite-like configuration is more stable than the  $\sigma$ -dimer; its interaction energy is 22.3 kcal mol<sup>-1</sup>, a value higher than that calculated coupled-cluster level (Kertesz, 2019).

## 5.2.2 PAHs RADICAL: ENERGY AND DIMERIZATION

Based on this test-case, the computational effort has been extended to larger molecular models based on the molecular constituent's experimental observations of incipient soot (Commodo *et al.*, 2019). Therefore, the two radical PAHs, named R1 and R2, and sketched in Figure 5.14, are examined in this session.

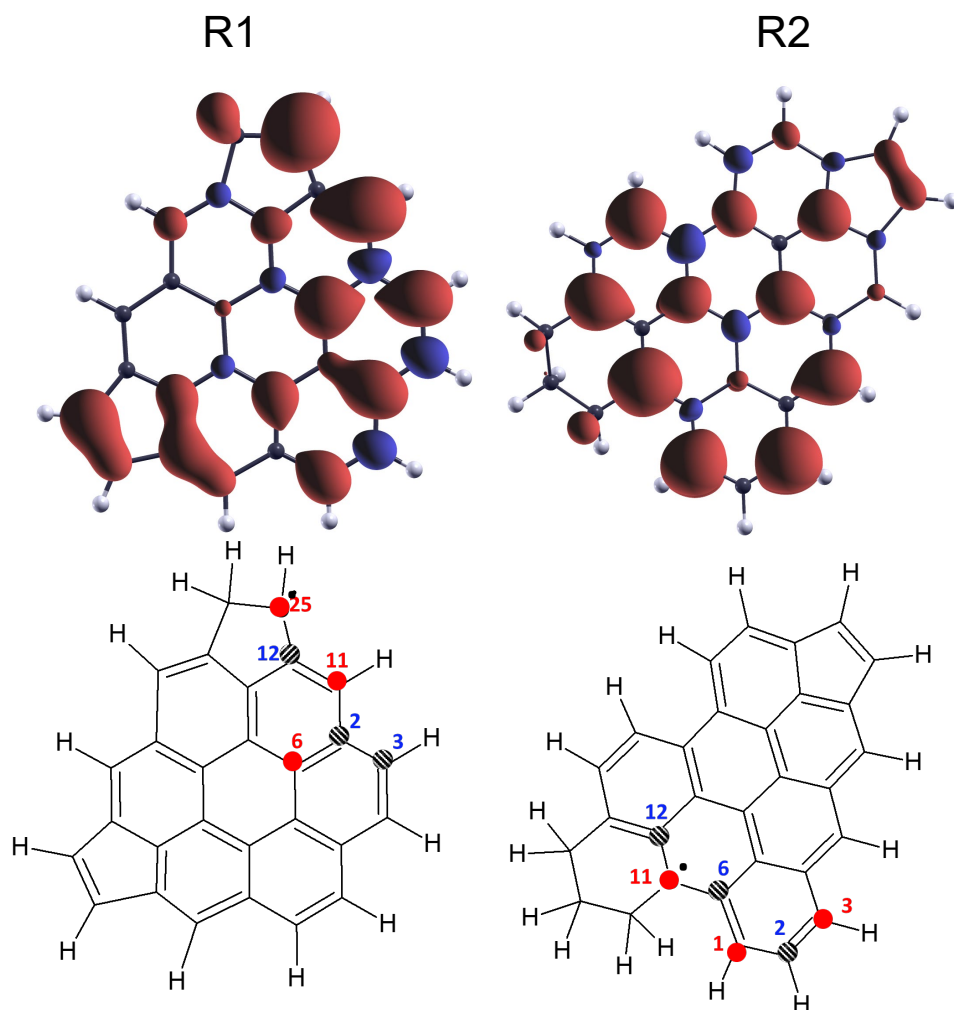


Figure 5.14 Investigated R1 and R2 radicals; Top panel: the spin isodensity surface projected only over the SOMO orbital. The surface ranges are evaluated at  $0.001 |e|/(a_0)^3$  isodensity. The red surface represents positive values, while the blue are negatives; the Lower panel: the molecular sketch, in which the small black dot is one of the possible resonance representations of the unsaturated site (carbon dangling bond). The circles (with atomic label) indicate the carbon atoms with the higher (positive) values of the MPAN of spin distribution. The striped circles indicate the carbon atoms with the lower (negative) values of the MPAN (values reported in Table 5.2).

The radicals have been preliminary studied as individual structures. In principle, these molecules are  $\pi$  radicals since the dangling bond's electron is not univocally localized in one specific atom site on the molecular plane. Thus the

unpaired electron is hosted by molecular orbitals belonging to the  $\pi$  system. Figure 5.14 (top panel) reports the calculated 0.001 electrons/bohr<sup>3</sup> iso-level of the electronic density, projected in the singly occupied molecular orbital (SOMO) range energy, in R1 and R2, respectively. It provides a topological representation of the magnetic behaviour of the molecules. Note that, this classical representation does not correspond to the physical position of the unpaired electron. Indeed, this latter is provided by MPAN that gives, in a first approach, the formal charges and spin densities, whose results are reported in Table 5.2 and also shown in Figure 5.13 (lower panel) as coloured dots highlighting the carbons with higher (red-label) and lower (blue-label) spin-orbital contribution.

Table 5.2. MPAN: Atomic net charge,  $\rho$ , and spin population,  $\mu$ , values for R1 and R2 radicals. All charges are expressed in electron fractions  $|e|$ .

C Atom (R1)	$\rho(R1)$	$\mu(R1)$	C Atom (R2)	$\rho(R2)$	$\mu(R2)$
2	0.13	-0.13	1	-0.17	0.33
3	-0.14	-0.08	2	-0.08	-0.15
6	0.06	0.18	3	-0.16	0.31
11	-0.23	0.41	6	0.09	-0.17
12	0.21	-0.21	11	0.00	0.42
25	-0.19	0.67	12	0.04	-0.14

R1 radical has a hybrid behaviour, due to its peculiar topology, showing a low delocalization of the unpaired electron. The carbon atom belonging to the non-aromatic ring (C25) shows a spin population  $\mu = 0.67 |e|$  (see Table 5.2), thus indicating a noticeable localization of the unpaired electron. It is also possible to find a second localization site, namely C11 (in alternate position concerning C25), which has a spin population  $\mu = 0.41 |e|$  (Figure 5.14 and Table 5.2). We could define this type of radical as a partially localized  $\pi$ -radical, whose role in the aggregation/clustering, through an enhanced binding in PAHs clusters, was formerly postulated by Wang(Wang, 2011), and in a recent DFT study thoroughly discussed by Martin et al.(Martin *et al.*, 2019a).

By contrast, the R2 radical can be considered as a pure  $\pi$  radical; indeed, the maximum localization does not exceed a spin population value of 0.42  $|e|$  over a single site (C11) while the other two with the largest spin population are equally



spanned among other two sites (C1 and C3, see Figure 5.14 and Table 5.2). The delocalization of the unpaired electron, specifically the spin population, was higher on peripheral carbon sites than the central ones.

The different delocalization of unpaired electrons in R1 and R2 radicals produces a substantial difference in dimer formation. Dimers of R1 radicals,  $D_{R1}$ , form a single bond between the carbon atoms, hosting the localized unpaired electron. The bond length is 1.603 Å, while the two poly-aromatic structures are slightly bent, as shown in the dimer equilibrium geometry reported in Figure 5.15, in which the calculated 0.001 electrons/bohr<sup>3</sup> iso level of the electronic density in  $D_{R1}$  and R2 dimers,  $D_{R2}$ , in both spin multiplicity, are reported.

To study the energetic contribution of the open-shell configuration in aromatic dimerization, we compared the calculated interaction energy of the  $D_{R1}$  and the corresponding closed-shell M1 molecule sketched in Figure 5.16. Indeed,  $D_{R1}$  can be formed by H atom abstraction from the partially protonated rim-based pentagonal ring of molecule M1 (backward reaction in Figure 5.16 upper panel).

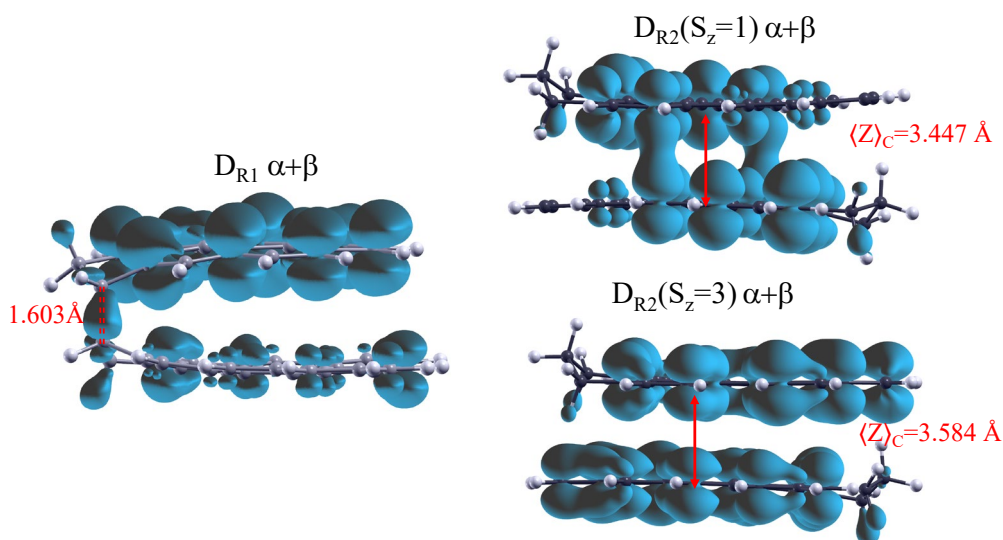
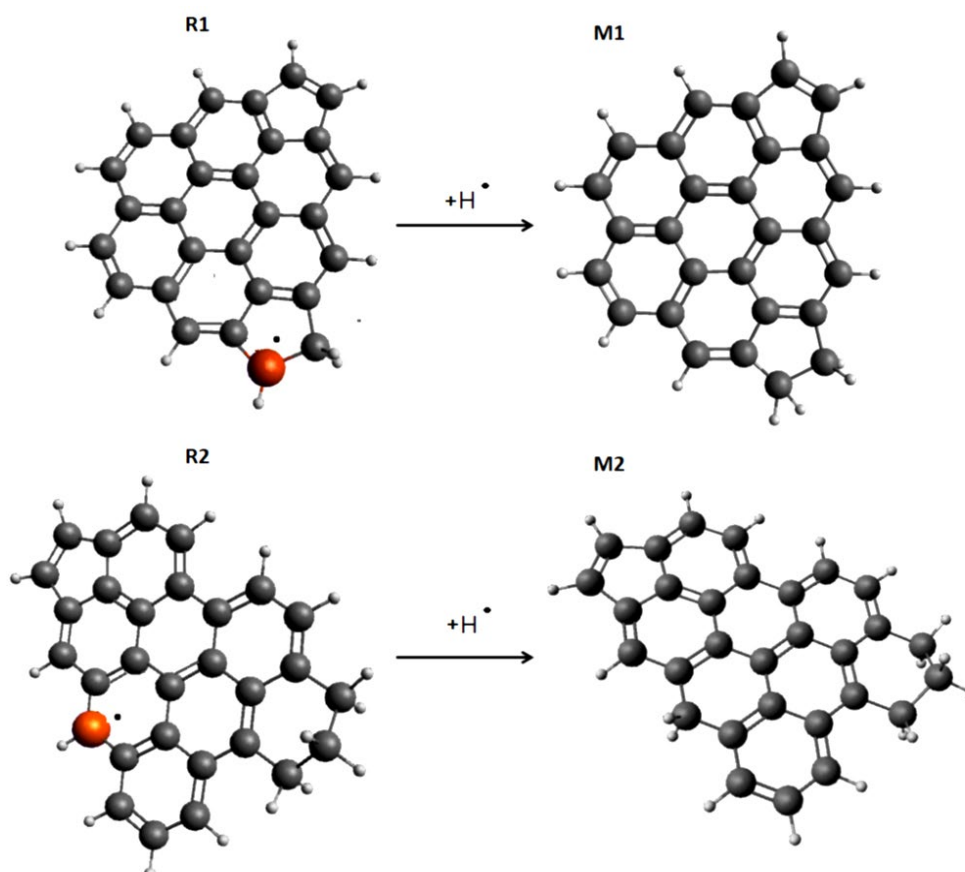


Figure 5.15. Calculated 0.001 electrons/bohr<sup>3</sup> iso level of the electronic density in  $D_{R1}$  and  $D_{R2}$  dimers.  $\langle Z \rangle_c$  is the average distance between the top and bottom carbon atoms  $z$ -coordinates.  $D_{R1}$  (left): the dashed line shows the distance of the C-C covalent bond; the two bonded C-atoms are  $sp^3$  hybridized  $D_{R2}$  (right): the  $D_{R2}$  head-tail structures, representing the more stable energetic configurational isomer in a singlet (top) and triplet state (bottom).

The calculated interaction energy for M1 dimer,  $D_{M1}$ , is about 30 kcal mol<sup>-1</sup>. We can assume that this value is representative of purely van der Waals interactions. The interaction energy in  $D_{R1}$  is 71.7 kcal mol<sup>-1</sup>. Therefore, assuming that the van der Waals interactions account for the same energy value for both  $D_{R1}$  and  $D_{M1}$  dimers, we can estimate that the  $\sigma$  bond contributes about 40 kcal mol<sup>-1</sup>, corresponding to a weak single C-C bond.



*Figure 5.16. Equilibrium molecular structures of M1 and M2 closed-shell molecules, derived from the R1 and R2 radicals. Radicals are formed by H atom abstraction from the partially protonated rim-based pentagonal ring of the molecules. The largest red spheres indicate the original radical's carbon atom where the hydrogen atom has been added*

For  $D_{R2}$ , different geometries, and spin multiplicities need to be considered. Significantly, three geometries have been explored, as reported in Figure 5.17:

- radicals perfectly overlapped;
- radicals shifted in graphite staggered like structure;
- radicals in the head-tail configuration.

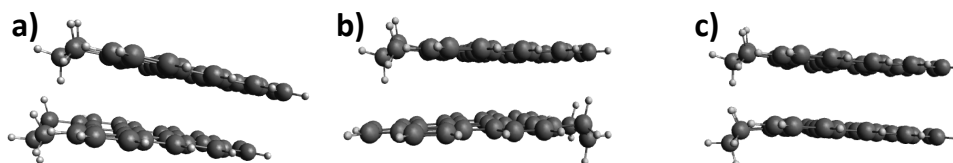


Figure 5.17. a)  $D_{R2}$  Staggered geometry; b)  $D_{R2}$  Head-tail geometry; c)  $D_{R2}$  Overlapped geometry.

Table 5.3 the interaction energies for  $D_{R2}$  in the three geometries and singlet and triplet multiplicity states.

Table 5.3 *Interaction energies and distances between molecules for three geometries and two multiplicity state of  $D_{R2}$ . All energies are reported without taking into account the BSSE corrections. The BSSE evaluation increases the interaction energies in a range from +7 to +8 kcal mol<sup>-1</sup>*

<b><math>D_{R2}</math> configurations</b>	<b>Sz=1 interaction energy [kcal mol<sup>-1</sup>]</b>	<b>Sz=3 interaction energy [kcal mol<sup>-1</sup>]</b>	<b>Sz=1 Distance [Å]</b>	<b>Sz=3 Distance [Å]</b>
Overlapped	-28.6	---	3.379	
Staggered	-31.1	-33.5	3.450	3.674
Head-tail	-33.7	-36.8	3.512	3.495

It is worth noticing that  $D_{R2}$  triplet multiplicity does not present the overlapped equilibrium geometry due to electronic repulsion. In  $D_{R2}$ , the  $\pi$  electronic densities tend to overlap, as shown in Figure 5.15; with a distance between the two stacked molecules that ranges from 3.40 to 3.60 Å, considering both the singlet and triplet state, with an average distance of 3.45 Å for the stack in singlet state and an average distance of 3.58 Å for the stack in the triplet state. Calculated distances are reported in detail in Table 5.3.

As for  $D_{R1}$ , we compare the interaction energy of the most stable  $D_{R2}$ , i.e., the head-tail configuration in the triplet state, to the interaction energy of the dimer of closed-shell M2 molecule,  $D_{M2}$ . A value of  $-35.8 \text{ kcal mol}^{-1}$  was calculated for the  $D_{M2}$ ; it is assumed that the interaction is purely due to van der Waals forces. Therefore, the interaction energy of the most stable  $D_{R2}$  is just a few  $\text{kcal mol}^{-1}$  ( $2\text{--}4 \text{ kcal mol}^{-1}$ ) larger than the interaction energy of the  $D_{M2}$  indicating a weak multi-centre  $\pi$ - $\pi$  orbital interaction.

The above analysis about the two radical dimers' interaction energy and the equilibrium geometry allows concluding that polycyclic aromatic radicals may form  $\pi$  stacking if the unpaired electron is sufficiently delocalized, which gives a slight overbinding in the cluster interaction concerning pure van der Waals interactions. When the molecule's topology causes some spin localization, like in the R1 case, a C-C covalent bond is formed among the localization sites.

### 5.2.3 ELECTRONIC BANDGAP CALCULATIONS

The electronic bandgap is an essential quantity to characterize semiconductors, and it is widely used for nanostructured materials investigations. However, the measured band gap strongly depends on the experimental method. For instance, optical, electrochemical, electrical bandgap may show slight differences since they monitor different processes (Bredas, 2014). Theoretically, the bandgap is the difference between the highest occupied molecular orbital (HOMO) and the lowest unoccupied molecular orbital (LUMO). Although B3LYP has been shown to over predict the measured optical band gap (Menon *et al.*, 2019), the HOMO-LUMO gap ( $E_g$ ) resulting from our model gives correct trends for gaps calculated at higher theory levels, and the method applies to large polycyclic aromatic models. The literature has recently reported a correlation between PAHs characteristics and their optical band gap, OBG (Chen and Wang, 2019; Liu *et al.*, 2019). PAH size, structural symmetry, cross-linking, curvature due to pentagonal-ring, radical presence, all these characteristics cause a variation on the OBG of PAHs (Menon *et al.*, 2019). In light of this, one of the main objectives of the present study is to deepen the analysis of the effect of the supramolecular assemblies of the polycyclic aromatic molecules and radicals on the HOMO-LUMO gap. To this aim, the energy gap between occupied and unoccupied electronic states has been evaluated for both open and closed-shell investigated dimers.

This computational investigation is aimed to shed light on some experimental observations indicating a typical value of the energy gap for just-nucleated soot particles which is of the order of 1.5-2 eV (34.6-46 kcal mol<sup>-1</sup>) (Commodo, De Falco, *et al.*, 2015), thus significantly lower than the typical energy gap of the constituent aromatic molecules.

The results of the DFT-D3 calculation in terms of the energy gap are reported in Figure 5.18. M1 molecule has a HOMO-LUMO gap of approximately 3.3 eV (76.1 kcal mol<sup>-1</sup>) that decreases when considering the corresponding R1 radical's SOMO-LUMO gap, i.e., 2.5 eV (57.65 kcal mol<sup>-1</sup>). A similar trend is also obtained for the corresponding dimers, D<sub>M1</sub>: the molecular dimer presents an energy gap of 3.2 eV (73.79 kcal mol<sup>-1</sup>) while the radical dimer, i.e., the  $\sigma$ -bonded D<sub>R1</sub>, has a gap of 3.03 eV (69.87 kcal mol<sup>-1</sup>).

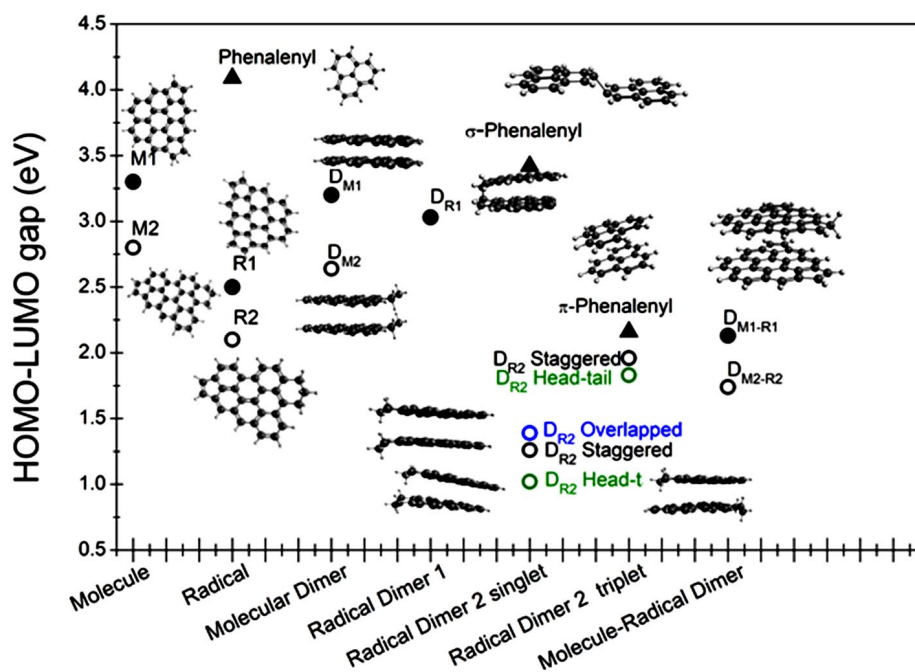


Figure 5.18: Calculated HOMO-LUMO gaps.

The M2 molecule has a gap of 2.8 eV (64.57 kcal mol<sup>-1</sup>), while the corresponding R2 radical gap is 2.1 eV (48.43 kcal mol<sup>-1</sup>). The stack constituted by two M2 molecules, i.e., D<sub>M2</sub> has a 2.6 eV (59.96 kcal mol<sup>-1</sup>) gap, slightly lower than the M2 molecule alone. In the dimer configuration of D<sub>R2</sub>, the orientation of the stacks might further affect the HOMO-LUMO gaps. Indeed, the triplet

electronic structures have higher gaps than the singlet ones. Specifically, the  $D_{R2}$  in overlapped geometry has an energy gap of 1.39 eV (32.05 kcal mol<sup>-1</sup>); the  $D_{R2}$  in staggered geometry has an energy gap of 1.26 eV (29.06 kcal mol<sup>-1</sup>) for singlet multiplicity state and 1.96 eV (45.20 kcal mol<sup>-1</sup>) for the triplet one;  $D_{R2}$  for head-tail configuration has an energy gap of 1.02 eV (23.52 kcal mol<sup>-1</sup>) for singlet and 1.83 eV (42.20 kcal mol<sup>-1</sup>) for triplet. The parallel spin electron repulsion explains this behaviour due to the exchange interaction in triplet configuration that decreases the coulombic repulsion causing stabilization of the HOMO and a consequent increase of the bandgap. It is evident from our calculations that the presence of delocalized  $\pi$  unpaired electrons sensibly decreases the HOMO-LUMO gap. Therefore, polycyclic aromatic radicals' stacking decreases the HOMO-LUMO gap by a quantity dependent on aggregation geometry and spin multiplicity.

### 5.3 CHARACTERIZATION OF INCIPIENT SOOT PARTICLES BY NUCLEAR MAGNETIC RESONANCE SPECTROSCOPY

As written in the previous paragraph, the DFT study has made it possible to theorize structural elements and functional groups responsible for generating the two different radicals. Then, from the presence of these elements, it is also possible to theorize the possible paths in the mechanism of formation .

It becomes clear that the need to prove the presence of these elements experimentally has become increasingly necessary.

The technique designated for this investigation was the NMR, specifically the  $^1\text{H}$ -NMR.

$^1\text{H}$ -NMR study was performed in collaboration with Professor Marina della Greca, SCF (Sintesi Caratterizzazione Fotochimica) group, Dipartimento di Scienze Chimiche - Università degli Studi di Napoli Federico II.

NMR is a technique utilized to characterize hydrocarbon fuels, solvent-soluble coal fractions, and asphaltenes (Calemma *et al.*, 1995; Guillén, Díaz and Blanco, 1998; Lee and Glavincevski, 1999; Durand *et al.*, 2010; Manoj *et al.*, 2012; Burger *et al.*, 2015; Dutta Majumdar *et al.*, 2017) but it is not very usual to find the characterization of flame carbon particles by  $^1\text{H}$ -NMR, especially in a premixed flame. Indeed,  $^1\text{H}$ -NMR spectroscopy has two significant drawbacks. First, in a spectrum of complex mixtures, such as those of flame samples, the peaks overlap could represent a factor because of the small chemical shift range. Second, some structural moieties do not have a defined number of hydrogen atoms. For example, for a polyaromatic molecule, the number of aromatic hydrogen atoms depends on the number of alkyl side-chains and the number of bridgehead carbons (Burger *et al.*, 2015).

In the literature, there are works and experiments carried out on C-NMR, later surpassed by C-NMR in solid-state (Pugmire *et al.*, no date; Solum *et al.*, 2001; Brown, 2012; Dutta Majumdar *et al.*, 2016, 2017). Unfortunately, it was not possible in this thesis work to perform a  $^{13}\text{C}$ -NMR analysis.

Earlier utilization of  $^1\text{H}$  NMR for soot analysis was made by Santamaria and coauthors who investigated the chemical functional groups of carbonaceous products from ethylene and ethylene/ethanol inverse diffusion flame (Santamaría *et al.*, 2006, 2007; Santamaría, Eddings and Mondragón, 2007; Salamanca *et al.*, 2012b).

But why the choice of NMR? The technique allows discerning the different types of protons to differentiate a proton bonded to a C hybridized  $sp^3$ ,  $sp^2$ , or  $sp$ . Moreover, NMR can distinguish a  $Csp^2$  of an aromatic or an aliphatic and identify an H atom bound to an O, N, or other heteroatoms. Hence NMR can confirm or deny H atoms' presence bonded in methylene ( $CH_2$ ) groups, for example, common motifs among the pool of molecules visualized at the HR-AFM experiments (Commodo *et al.*, 2019; Schulz *et al.*, 2019). The same molecules consistent with a radical propagation mechanism initiated the previous paragraph's hypotheses with the DFT calculations. The presence of a specific H that by homolytic cleavage leads to the formation of an  $\sigma$  or  $\pi$  radical.

Based on the experimental data that showed the presence of elements such as, methylene, methyl, vinyl groups, aliphatic chains linked to PAHs, presence of internal and external Penta-rings and motivated by the fact the molecular constituents of incipient soot are rich in hydrogens, particles collected at a residence time corresponding to inception or nucleation step were analyzed.

The flame and the experimental approach are described in chapter 4, i.e., a laminar premixed ethylene-air flame stabilized on a McKenna burner, cold gas stream velocity set 9.8 cm/s, and the carbon-to-oxygen atomic ratio (C/O) was set to 0.67. The flame products were sampled using a horizontal tubular probe (stainless steel tube, 1 cm outer diameter) with a downward orifice (inner diameter = 2.5 mm, thickness = 0.5 mm) positioned at the sampling point in the flame. Compared to the earlier studies dilution was lowered to collect enough material for the NMR analysis. The quartz filters, dissolved, extracted and redissolved in deuterated chloroform ( $CDCl_3$ ) were placed into an NMR cuvette. The NMR analysis was carried out with a *Bruker Ascend<sup>TM</sup>* operating at the  $^1H$  frequency of 400.130 MHz in  $CDCl_3$ .  $^1H$  spectra were obtained using the following parameters: 128 transients, 65 K data points.

The HAB was set at 8 mm, assumed to be the onset point of soot particle formation (Commodo, De Falco, *et al.*, 2015; Commodo *et al.*, 2019; Schulz *et al.*, 2019), corresponding to a monomodal particle size distribution with maximum positioned at a mobility diameter of 2.4 nm, as it is possible to notice in Figure 5.1 of this chapter.

Figures 5.19 and 5.20 show the  $^1H$  NMR spectra, in the chemical shift range between 0-5 and 5-10 ppm, of the chloroform-soluble fraction of the incipient soot. These two regions could be defined approximately as the aliphatic and the aromatic regions.



Some signals in the aromatic region and aliphatic region could appear more shielded because of the aromatic ring current and probably stacked geometry (Dutta Majumdar *et al.*, 2017).

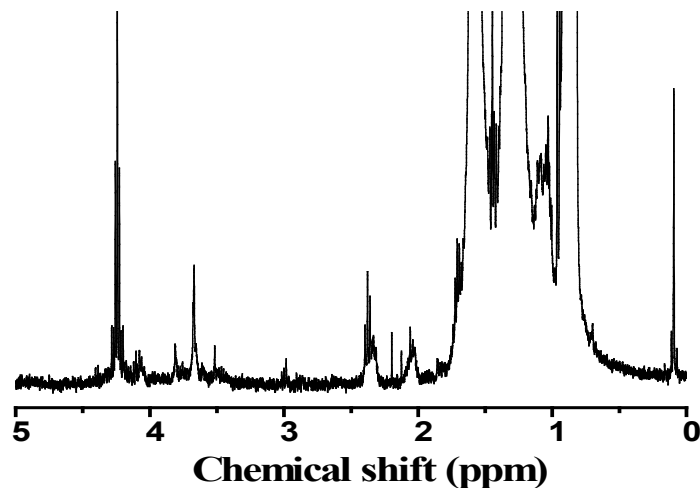


Figure 5.19: NMR spectrum in 0-5 ppm range in the "aliphatic region."

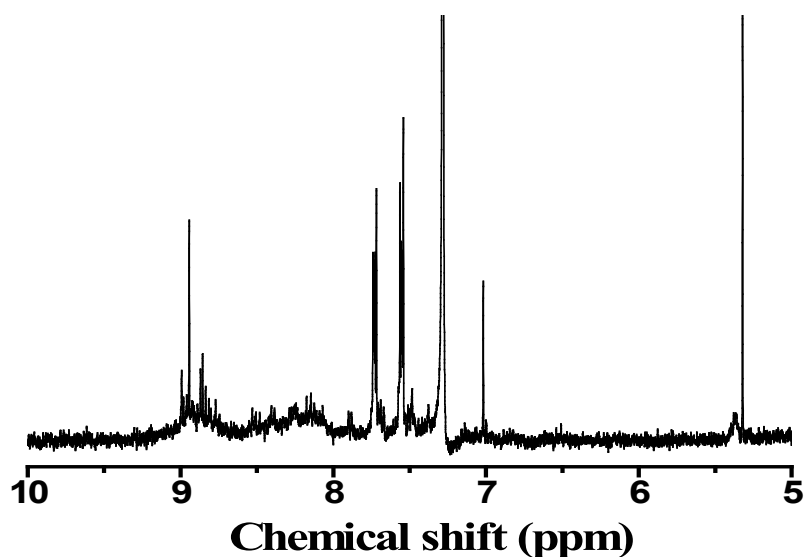
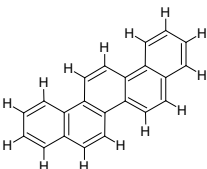
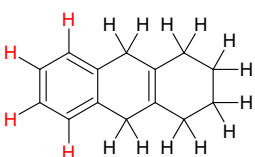
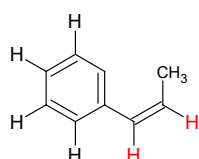
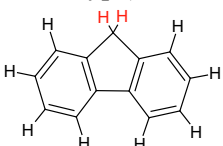


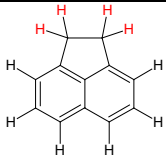
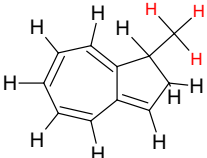
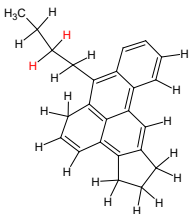
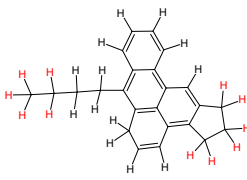
Figure 5.20: NMR spectrum in the 5-10 ppm range in the "aromatic region."

However, it should be specified that, within the two large macro-areas defined above, there are sub-classifications of protons. The assignment of the peaks of the spectrum can be performed according to the classification of the chemical shifts of protons schematized in table 5.4 (Calemma *et al.*, 1995; Decesari *et al.*, 2000;

Yang *et al.*, 2003; Santamaría *et al.*, 2006, 2007; Santamaría, Eddings and Mondragón, 2007; Durand *et al.*, 2010; Burger *et al.*, 2015).

*Table 5.4. Assignments of the proton chemical shifts in  $^1\text{H}$  NMR spectra. IN the pictured structure, the Hydrogens responsible for the corresponding chemical shift are highlighted in red*

Hydrogens	Description	Chemical shift, $\delta$ (ppm)
$\text{H}_{\text{a}2}$	Aromatic hydrogens (polyaromatic) 	7.5–10.5
$\text{H}_{\text{a}1}$	Aromatic hydrogens (monoaromatic) 	6.5–7.5
$\text{H}_{\text{o}}$	Olefin hydrogens (vynilic CH and $\text{CH}_2$ ) 	5.0–6.5
$\text{H}_{\alpha 2}$	<ul style="list-style-type: none"> <li>Aliphatic hydrogens in methylene (<math>\text{CH}_2</math>) groups <math>\alpha</math> to two aromatic rings (fluorene type) </li> <li>Aliphatic hydrogens in methylene (<math>\text{CH}_2</math>) groups <math>\alpha</math> to an aromatic ring and <math>\beta</math> position to another (acenaphthene type)</li> </ul>	2.5–5.0

		
$H_{\alpha 1}$	<p>Aliphatic hydrogens in methyl (<math>CH_3</math>) groups <math>\alpha</math> to an aromatic ring</p> 	2.0–2.5
$H_{\beta}$	<p>Aliphatic hydrogens in methylene (<math>CH_2</math>) groups in <math>\beta</math> position to an aromatic ring (paraffinic <math>CH_2</math>)</p> 	1.0–2.0
$H_{\gamma}$	<p>Aliphatic hydrogens in methyl (<math>CH_3</math>) groups <math>\gamma</math> or further to an aromatic ring (paraffinic <math>CH_3</math>), alkanes, cycloalkanes. Naphthenic rings</p> 	0.5–1.0

As shown in Figure 5.19 and Figure 5.20, the spectra show a very intricate shape, the peaks are vast, and all this is caused by the complexity of the material analyzed. The spectrum of incipient carbon nanoparticles displays several peaks in the regions schematized in the table.

The magnitude or intensity of NMR resonance signals is proportional to the molar concentration of the sample. Thus, a small or dilute sample will give a weak

signal, and doubling or tripling the sample concentration increases the signal strength proportionally. If we take the NMR spectrum of equal molar amounts of benzene and cyclohexane in a suitable solvent, such as carbon tetrachloride solution, the resonance signal from cyclohexane will be twice as intense as that from benzene because cyclohexane has twice as many hydrogens per molecule. This relationship is very significant when samples incorporating different sets of hydrogen atoms are examined since it allows the ratio of hydrogen atoms in each distinct set to be determined.

In Figure 5.21, the spectrum in the 0-2.5 ppm range is shown. The spectrum shows the TMS peak, the internal standard, and very intense aliphatic CH<sub>2</sub> and CH<sub>3</sub> peaks, probably caused by long saturated chains.

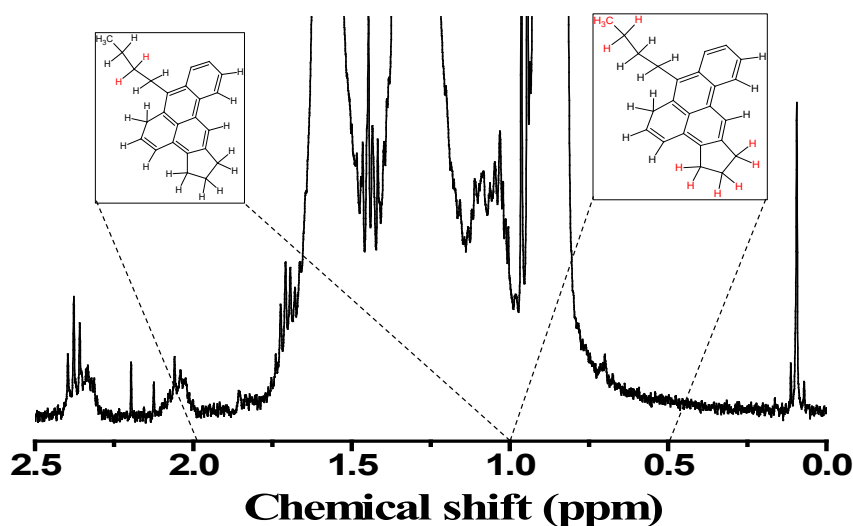


Figure 5.21: NMR spectrum in 0-2.5 ppm range

In Figure 5.22, a closer look at the spectrum area between 2 and 2.5 ppm displays the presence of two peaks, corresponding to methyl groups on aromatics (H<sub>α1</sub>).

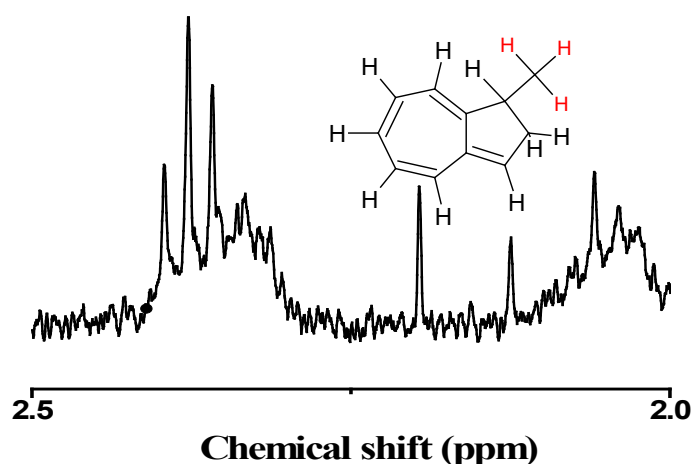


Figure 5.22: Zoom in the 2-2.5 ppm area.

Figure 5.23 illustrates the spectral range between 2.5-5.0 ppm.

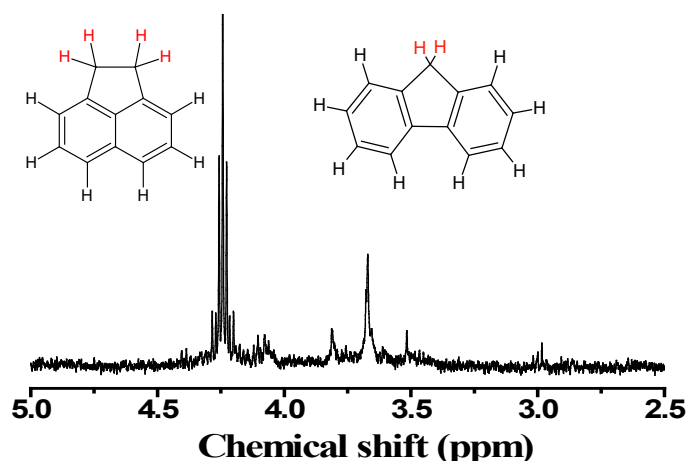


Figure 5.23: 2.5-5.0 ppm spectral range.

In this area, corresponding to schematized  $H_{\alpha 2}$  in table 5.4, several peaks are present. These peaks could be attributed to the hydrogens in methylene groups ( $CH_2$ ) of fluorene and acenaphthene type configuration. The presence of protons as those of fluorene and acenaphthene type configurations in the analyzed incipient carbon particles analyzed is fascinating. These data could confirm the theory on a generation of resonantly stabilize radicals (RSRs) and localized  $\pi$ -radicals, that are recognized as critical species in the soot nucleation/formation process (Johansson *et al.*, 2018; Martin *et al.*, 2019a). It is noted that peaks in this region may also originate from oxygen functionalities, such as the hydroxyl group

–OH. However, in the same flame conditions, X-ray photoelectron spectroscopy and HR-AFM revealed ethereal and hydroxyl oxygen (Johansson *et al.*, 2016; Commodo *et al.*, 2017, 2019; Schulz *et al.*, 2019). Besides, the radical nature of the analysed sample molecules should be considered, which would lead to the probability of quenching by oxygen during the sampling and storage procedure.

Nevertheless, the quantity detected would suggest being in quantities such as to be considered negligible compared to the carbonaceous matrix. Therefore the resonant protons in this zone are attributable with a high probability to  $H_{\alpha 2}$  protons.

The second macro-area is the aromatic one. The range between 5-7.5 ppm showed in Figure 5.24 displays the prominent peak at 7.24, due to solvent residue. The other small peak could be associated with  $H_o$  due to finding protons linked to unsaturated carbons.

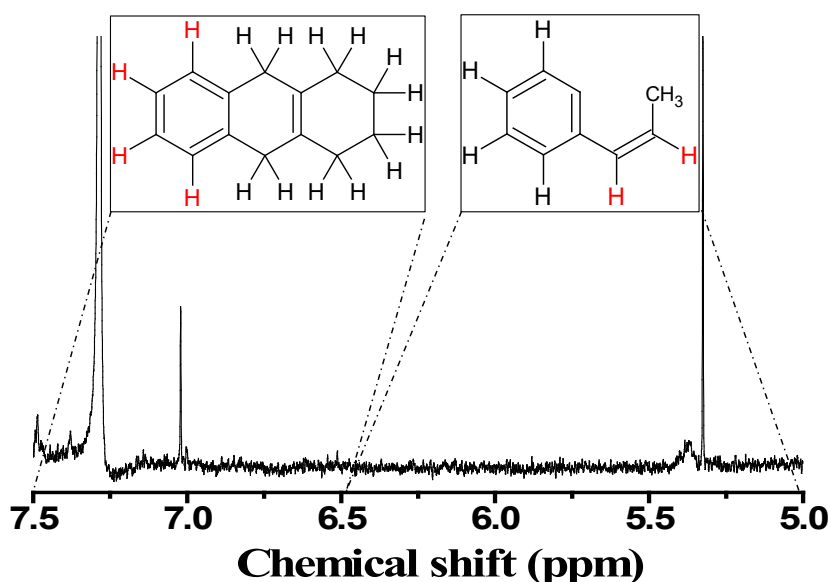
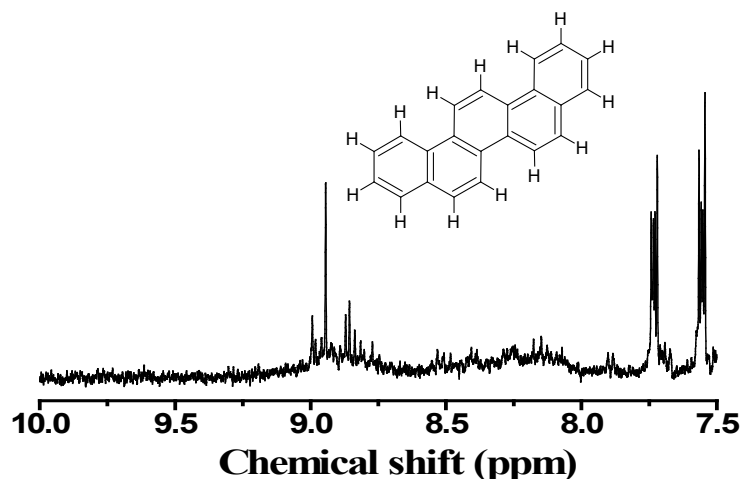


Figure 5.24 Spectral area between 5 and 7 ppm.

In the last section of the spectrum, ranging from 7.5 to 10 ppm, Figure 5.25, the aromatic zone is shown; the one arising from protons bound to carbons in polyaromatic structures. In Table 5.4, such protons have been defined as  $H_{a2}$ . It is possible to notice the presence of more or less defined signals. Between 8 and 9 ppm we notice mostly bands. Although the aromatic hydrogen would seem less significant, this does not mean that these structures are absent but could be caused by highly condensed structures with large numbers of fused carbons that cannot

visualize. Also, the relaxation of spin precessions of the aromatic proton nuclei back to their thermodynamic states results in a vast decrease in the  $^1\text{H}$ -NMR peak heights for interacting assemblies, accompanied by considerable line broadening.

The shift towards lower ranges can be attributed to several factors. The effect of an extended aromatic structure such as PAHs should be mentioned, the larger it is, the more complex and shifted/deshielded the peaks will appear because of  $\pi$ -the electron ring current. It should be considered that the analysis has been carried out on complex material, characterized by components that "interfere" the symmetry, such as penta-rings,  $\text{sp}^3\text{C}$ , and therefore the equivalence of protons that are shifted. In the last analysis, the interaction of molecules, aggregation, and the possibility of the formation of stacking should be taken into account, all factors that provide a more significant amount of complexity.



*Figure 5.25: Last examined range in the aromatic zone. The area between 7.5 and 10 ppm*

Thus through the NMR spectroscopy in this thesis work, it was possible to carry out an exploratory investigation of the incipient carbonaceous particles, investigating the presence of protons characteristic for the deployment of the soot formation process in flame. It is to be hoped that this preliminary investigation could lay the groundwork and pave the way for a more 'in-depth application on the subject, combining the  $^{13}\text{C}$ -NMR and allowing for ranging in the field of NMR in solid-state.

## 5.4 RADICALS IN NASCENT SOOT FROM LAMINAR PREMIXED ETHYLENE AND ETHYLENE-BENZENE FLAMES

In this last paragraph, data related to the study of carbon particles produced in a premixed ethylene-air flame and premixed ethylene-benzene-air flame are shown. Analysis and characterization study has featured an in-depth study of the nature of the chemical-structural changes along the flames. On the other hand, however, we have focused on the radical nature of the process, the differently formed radicals at the time of nucleation, their role and influence in the various forms of larger and larger particles inside the flame.

The generation of stable aromatics is of fundamental importance to the entire soot formation mechanism. The formation of aromatic radicals might be strongly related to the fuel chemical structure and to the environment in which the fuel reacts. It is the case of aromatic hydrocarbons, which during oxidation can be more effective in forming resonantly stabilized  $\pi$ -radicals, e.g., cyclopentadienyl, benzyl, or indenyl radicals in comparison with aliphatic hydrocarbon. The formation of such radicals promotes molecular growth, and indeed, soot formation in aromatic fuel flames occurs across the flame front, in an environment still rich in oxidizing species (Minutolo, Gambi and D'Alessio, 1996; Tregrossi, Ciajolo and Barbella, 1999).

It is precisely the different propensity of aromatic fuels compared to aliphatic fuels to form resonantly stabilized radicals already at the flame front that has motivated this experimental research campaign to understand further the role of radicals in the formation subsequent growth of nascent soot particles.

As described earlier in section 4.5.1, EPR spectroscopy is specific in studying paramagnetic centres such as free unpaired electrons, located in conducting bands or in localized edge states (Ingram, 1961). For this reason, it has long provided a valuable probe of the electronic properties for carbon-based materials with extended  $\pi$ -electron systems, inquiring both the chemical and structural basis of carbon soot particles. Indeed, EPR spectral features (i.e. g-factor, signal linewidth, and spin-density) would also reflect the influence of the environment on the magnetic properties of unpaired electrons, rendering the latter useful probes of the chemical nature and amount of radical species within soot particles, the presence of  $\pi$ -conjugation and finally for the supramolecular organization of aromatic molecules into particles (Rhodes, 2011).



To this end, two sets of laminar premixed ethylene air flames have been investigated. The two flames, in each set, were characterized by the same equivalence ratio, temperature, and unburned gas velocity, in which 30% of ethylene carbon was replaced by benzene. To follow the comparison between the two kinds of fuel the particles collected have been analyzed to determine their size by electrical mobility measurements, chemical/structural characteristics by Raman spectroscopy, and radical amount and characterization through the electron spin density measurement EPR spectroscopy.

The two flames will be designated as Et and Et-30%B for the Ethylene/Air flame and the Ethylene/Benzene/Air flame, respectively.

A summary of the experimental conditions is reported in Table 5.5. The cold gas velocity was set to 10 cm/s (NTP) for all flames and the equivalence ratio,  $\Phi$ , was fixed at 1.89 for the first set of ethylene and ethylene/benzene flames and 2.01 for the second set of flames, thus keeping the total carbon flow rate fixed at 32.43 and 33.56 mg/s, respectively. In the Ethylene/Benzene/Air flame, 30% of the total carbon flow rate was obtained by adding pre-vaporized benzene instead of ethylene. Finally, a nitrogen flow was added to the Ethylene/Benzene/Air flame to keep both the two flames' cold gas velocity and equivalence ratio. Both air and nitrogen fluxes were heated to 100 °C to avoid benzene condensation in the benzene-doped flame and to ensure equal inlet conditions to the two flames in each set.

*Table 5.5. Experimental conditions: flows and flame characteristics*

Flame		Flow, l/min (STP)				Cold gas velocity, cm/s	Equivalence ratio ( $\Phi$ )	Maximum temperature, K
		C <sub>2</sub> H <sub>4</sub>	C <sub>6</sub> H <sub>6</sub>	Air	N <sub>2</sub>			
Ethylene/Air	Et	1.982	0	14.981	0	10	1.89	1820±50
Ethylene/Benzene/Air	Et-30%B	1.387	0.198	14.232	1.145	10	1.89	1830±50
Ethylene/Air	Et	2.051	0	14.577	0	10	2.01	1810±50
Ethylene/Benzene/Air	Et-30%B	1.436	0.205	13.848	1.139	10	2.01	1825±50

Different soot samples were collected at various heights above the burner distances to sample particles with different size distributions representative of the initial stages of soot formation. To compare the data between the flames and different sampling conditions, the characterization was performed using DMA, Raman, and EPR. The instrumentations and the procedure used for the online and off-line characterization have already described previously in the experimental chapter.

The size distribution of particle volume, PSDs, measured at a different height above the burner, in both sets of flames are reported in Figure 5.26 normalized to the total particle volume.

Particles sampled at the lowest HAB, in each flame, correspond to nucleation particles and the size distribution is mostly below 5 nm. Increasing the HAB, the PSD changes to larger sizes, and a more extensive mode of particles, i.e., more prominent than 7 nm, occurs. The typical trough between the nucleation and growth modes, as observed in previous investigations (Commodo *et al.*, 2019; Giuseppe Vitiello *et al.*, 2019), is now not observed and it can be ascribed to the higher temperature of the present flames caused by the preheating of the fuel/air mixture necessary to avoid benzene condensation in the feeding line (Abid *et al.*, 2008).

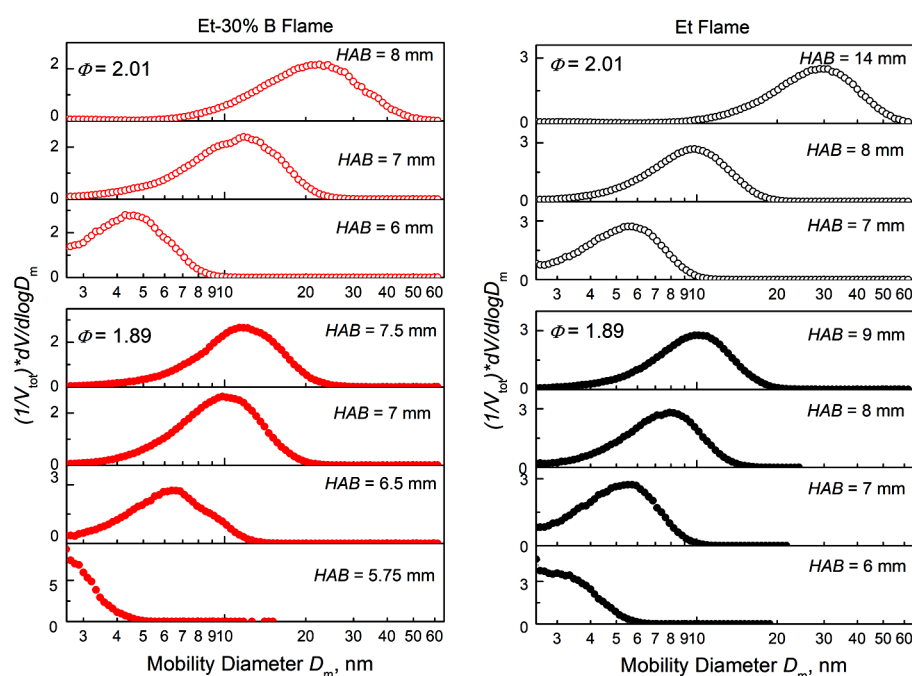


Figure 5.26. Volume PSDs normalized to the total particle volume measured at different HAB for the ethylene flames (left column) and the ethylene/benzene flames (right column).

For each of the selected flame conditions, particles were analyzed by EPR to measure the amount and nature of persistent radicals.

EPR analysis were performed in collaboration with Dr. Giuseppe Vitiello of the “Dipartimento di Ingegneria Chimica, dei Materiali e della Produzione Industriale”, Università degli Studi Di Napoli Federico II”.

EPR spectra are reported in Figure 5.27 and 5.28, while the corresponding spectral parameters are listed in Table 5.6. All spectra show a single peak at the Landé  $g$ -factor ranging between 2.0023-2.0026 ( $\pm 0.0003$ ). The measured  $g$ -value, which is very close to the value for free electrons, indicates that all the samples contain carbon-centred aromatic radicals for which the unpaired electron has a minimal orbital contribution to the magnetic moment (Yordanov and Lubenova, 2000).

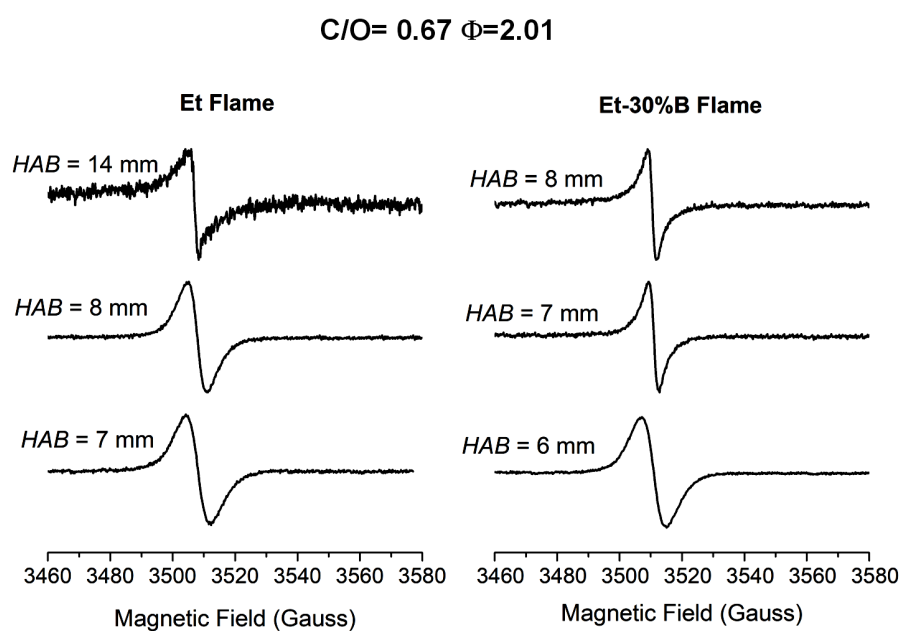


Figure 5.27 EPR spectra of sampled particles at different heights above the burner for the pure ethylene flame (left column) and ethylene/30%Benzene flame (right column). For flames having equivalence ratio  $\Phi = 2.01$ .

C/O= 0.63  $\Phi=1.89$

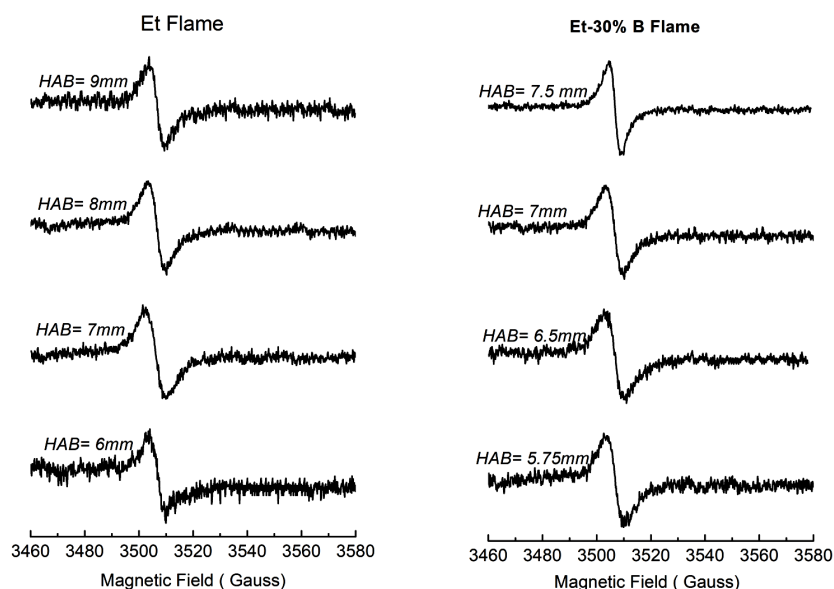


Figure 5.28 EPR spectra of sampled particles at different heights above the burner for the pure ethylene flame (left column) and ethylene/30% Benzene flame (right column). For flames having equivalence ratio  $\Phi = 1.89$ .

A detailed analysis of line-shape and broadening shows an evolution of the paramagnetic signal along the flames. Generally, a broad and Gaussian line-shape is associated with multiple paramagnetic species and superposition into the particles (Valavanidis *et al.*, 2008; Herring *et al.*, 2013). The line-shape narrows when electron-electron interactions become more potent (Ingram, 1961) such as when there is a greater delocalization of unpaired electrons, and there is a more significant formation of stacks of aromatic functional groups hosting free radicals. From the results of EPR spectroscopy, reported in Table 5.6 and Table 5.7, it appears that narrowing occurs soon after the first appearance of particles, in correspondence to initial particle growth and also the line-shape changes progressively from being prevalently Gaussian to a combination of Gaussian and Lorentzian.

Table 5.6. EPR spectral parameters of the sampled soot particles collected in Et-Flames. Note: errors in parenthesis refer to the standard deviation of three measurements for each sample.

Et Flame						
$\phi$	HAB (mm)	$\langle D_{m,v} \rangle$ (nm)	g-factor ( $\pm 3E-4$ )	$F_v$ ( $cm^3/cm^3$ )	$\Delta B$ ( $\pm 0.2$ )	% Lorentz ( $\pm 5\%$ )
2.01	7	5.3	2.0024	$2.7e^{-8}$	8.0	24
	8	9.3	2.0023	$3.2e^{-8}$	6.4	31
	14	27.7	2.0023	$7.7e^{-8}$	5.0	35
1.89	6	3.5	2.0026	$7.1e^{-9}$	6.2	19
	7	5.1	2.0025	$1.9e^{-8}$	7.8	16
	8	7.4	2.0026	$4.1e^{-8}$	6.7	25
	9	9.4	2.0025	$6.8e^{-8}$	6.3	30

Table 5.7. EPR spectral parameters of the sampled soot particles collected in Et-30%B Flames. Note: errors in parenthesis refer to the standard deviation of three measurements for each sample

Et-30%B Flame						
$\phi$	HAB (mm)	$\langle D_{m,v} \rangle$ (nm)	g-factor ( $\pm 3E-4$ )	$F_v$ ( $cm^3/cm^3$ )	$\Delta B$ ( $\pm 0.2$ )	% Lorentz ( $\pm 5\%$ )
2.01	6	4.5	2.0025	$1.9e^{-8}$	8.1	25
	7	10.9	2.0025	$4.7e^{-8}$	3.2	51
	8	21.4	2.0023	$8.7e^{-8}$	3.0	55
1.89	5.75	3.3	2.0024	$2.4e^{-9}$	7.8	18
	6.5	6.3	2.0026	$2.5e^{-8}$	7.5	23
	7	9.7	2.0025	$7.4e^{-8}$	5.6	28
	7.5	11.5	2.0023	$8.9e^{-8}$	4.7	44

Another exciting result of the EPR analysis is the inverse dependence with a particle size of the electron spin density measured in the different soot samples, shown in Figure 5.29; a similar lowering of the radical populations is observed during the particle growing process, regardless of the flame equivalence ratio and the addition of benzene to the fuel mixture.

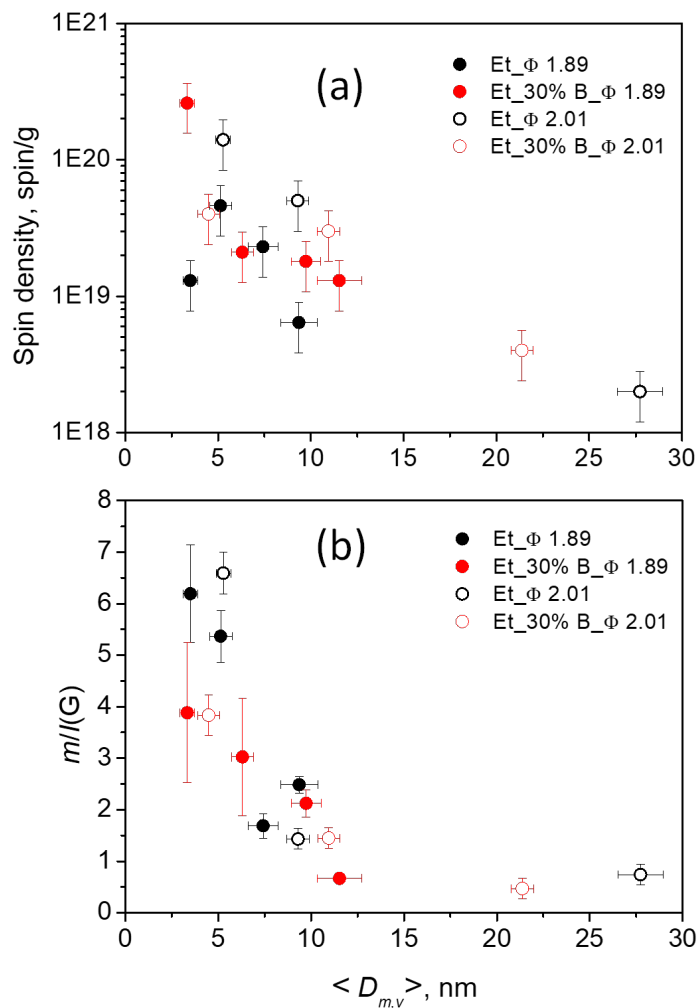


Figure 5.29 Trends as a function of the average volumetric particle size,  $\langle D_{m,v} \rangle$ , of spin density values as obtained by EPR measurements (a) and photoluminescence intensity reported as  $m/I(G)$  ratio (b).

A Raman spectroscopy analysis of the soot particles has been performed to investigate the effects of carbon nanostructure on the EPR observations.

The first-order Raman spectrum, i.e., 1000–2000  $\text{cm}^{-1}$ , of particle collected in two sets of flames are reported in Figure 5.30. The two prominent bands appear, one centred at about 1600  $\text{cm}^{-1}$ , G band, the most influential band measured in graphite and due to all  $sp^2$  bonds, the other one, the D band, centred at about 1350  $\text{cm}^{-1}$ .

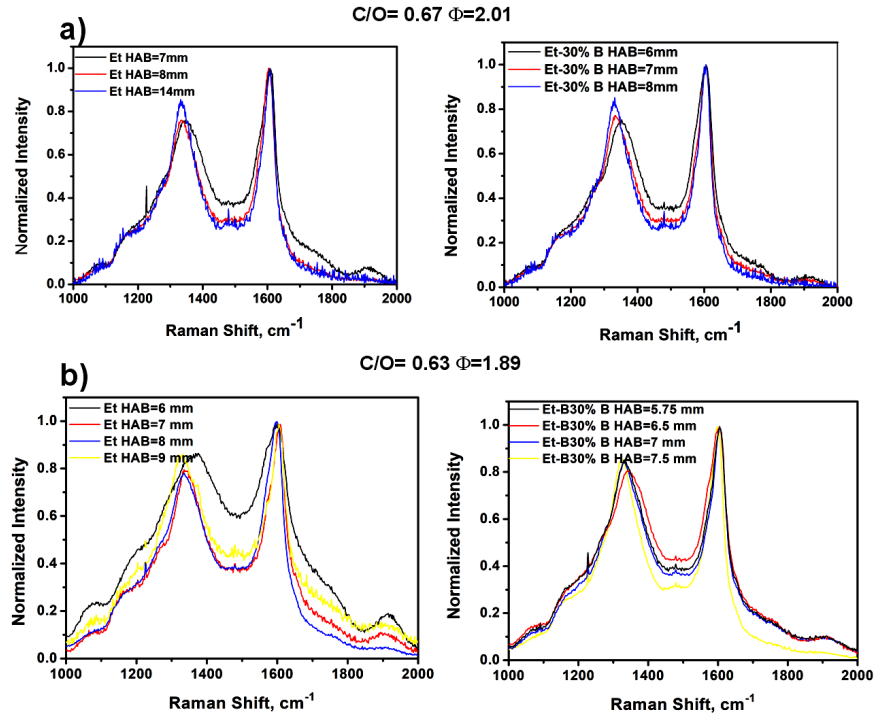


Figure 5.30: Raman spectra of particles collected in the Et and Et-30%B flame: a) Set flame with  $C/O=0.67$ ; b) Set flame with  $C/O=0.63$ .

The D band is prohibited in the perfect hexagonal lattice of graphite and is activated by defects in the  $sp^2$  aromatic network, such as the edges in the graphitic planes (Ferrari and Basko, 2013). For soot and any disordered carbon, other defect bands can be detected at 1200  $\text{cm}^{-1}$ , 1500  $\text{cm}^{-1}$ , and 1620  $\text{cm}^{-1}$ . Since the exact attribution of these defect bands is under debated yet, the various fitting procedure is reported in the literature to deconvolute the Raman spectrum in terms of the different contributions (Calemma *et al.*, 1995; Ferrari and Basko, 2013; Seong and Boehman, 2013; Minutolo *et al.*, 2014; Bonpua *et al.*, 2019; Le *et al.*, 2019) and there is not yet a widely accepted approach. Instead, it is widely accepted that a correlation exists between the relative intensity of the two major bands, D and G, with the average size of aromatic islands,  $L_a$ , in the carbon matrix. For highly disordered materials with the tiny size of the graphite crystallites, that is the case

for soot particles (Seong and Boehman, 2013; Minutolo *et al.*, 2014; Bonpua *et al.*, 2019; G. Vitiello *et al.*, 2019; Le *et al.*, 2019; Martin *et al.*, 2019a), the intensity ratio between the D and G peak is proportional to  $L_a^2$  (Ferrari and Basko, 2013) although the exact determination of  $L_a$  depends on the deconvolution method used. Regardless of the procedure used to determine band intensity and area, for the conditions examined in this work the ratio  $I(D)/I(G)$  is relatively constant so that  $L_a$  does not change sensibly among the various examined flame conditions. In light of this, the EPR line-shape narrowing cannot be ascribed to a greater delocalization of unpaired electrons in larger  $L_a$  domains. As observed for other carbonaceous materials, such as asphaltenes (Calemma *et al.*, 1995), and as observed for the EPR results in chapter 4.1, another plausible contribution to the line shape's narrowing could be related to stacking interactions between flat conjugated structures hosting unpaired electrons. Indeed, leading to an overlapping of the electronic wave functions, and thus promoting electron interaction, the stacking of adjacent radicals would explain the observed line narrowing at increased particle size.

In addition to the Raman bands, the Raman spectra of particles often present a photoluminescence background (PL), as shown in Figure 5.31. PL background has also been reported for hydrogenated carbon, attributed to the radiative recombination of electrons and holes in the localized states created by  $sp^2$  clusters (Casiraghi *et al.*, 2005).

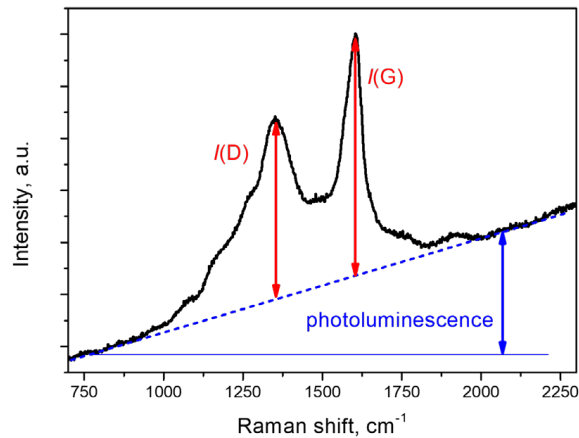


Figure 5.31. Raman spectrum of soot particles collected in the Et-30%B Flame at  $Z = 6$  mm and  $\Phi = 2.01$ , highlighting the photoluminescence (PL) background.



Such background can be due to radiative emission from the aromatic constituents of the soot particles. Following the procedure reported by Casiraghi *et al.* (Casiraghi *et al.*, 2005) the PL intensity was measured by evaluating the slope of the PL linear background,  $m$ , divided by the intensity of the G band,  $I(G)$  which is due to the total  $sp^2$  carbon in the sample. Therefore, such a method provides the amount of fluorescing component concerning the total  $sp^2$  carbon present in the analyzed sample. In Figure 5.32, this quantity is plotted as a function of  $\langle D_{mv} \rangle$  for all the samples.

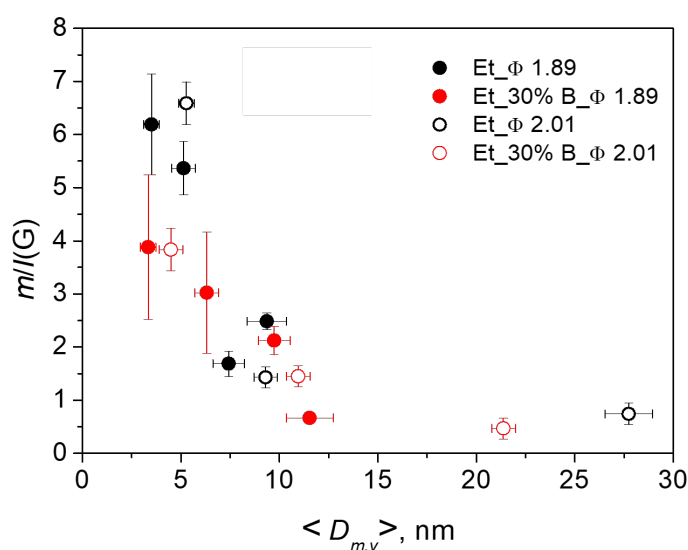


Figure 5.32 Trends as a function photoluminescence intensity reported as  $m/I(G)$  ratio.

For this analysis, we have evaluated the G band intensity considering only the D and G bands' contributions to the spectrum to be consistent with the Casiraghi work (Casiraghi *et al.*, 2005). Interestingly, particles produced in all the Et and Et-30%B flames seem to follow a single trend inversely proportional to particle size. This behaviour suggests that the detected radiative emission originates from a molecular constituent at the particles' surface. Previous works on ethylene flames, have shown that the small incipient particles are made of a similar molecular constituent as the larger primary particles (Commodo *et al.*, 2019; Schulz *et al.*, 2019), and the fluorescence spectra of such particles suspended in a solvent are also very similar (De Falco *et al.*, 2020). The main difference consists in the interactions among the molecular constituents, which become stronger as particles grow. The decrease of  $m/I(G)$  as particles grow can be explained by the more substantial radiative quenching and self-absorption of the fluorescence emitted by

molecules in the particles' interior. Because of this, the detected fluorescence derives prevalently from molecular constituents of the particles at the surface. Therefore it can be considered as a surface property of the soot particles.

The inverse dependence with particle size is also followed by the electron spin density measured in the samples. The similar trends for both  $m/I(G)$  and spin density for both flames might indicate that the major contributor to the measured spin density derives from paramagnetic centres localized at the particle surface. Since EPR is a volume sensitive technique, this result is not due to the measurement method but is a property of the particles.

It is interesting to note that as evidenced by Casiraghi in the investigation of hydrogenated amorphous carbon, the logarithm of  $m/I(G)$  quantity is linearly correlated to the hydrogen atomic percentage through the following empirical equation, valid for  $m/I(G)$  expressed in  $\mu\text{m}$  (Casiraghi *et al.*, 2005):

$$H[\text{at. \%}] = 21.7 + 16.6 * \log\left\{\frac{m}{I(G)}\right\} \quad (2)$$

Using this equation and evaluating the slope  $m$  in the spectral range of  $750 - 2150 \text{ cm}^{-1}$ , as indicated in Figure 5.31, the spin density trend can be reported as a function of  $H/C$ , as shown in Figure 5.33. This plot indicates that paramagnetic centres are dependent on the number of hydrogenated sites on the particle. It is worth to mention that the linearity evidenced by Casiraghi among the percentage of hydrogen and  $\log(m/I(G))$  has also been confirmed by other researchers although observing different values of the slope and intercept of the line (Buijnsters *et al.*, 2009; Pardanaud *et al.*, 2013). The use of the linear equations suggested by Buijnsters *et al.* (Buijnsters *et al.*, 2009) or by Pardanaud *et al.* (Pardanaud *et al.*, 2013) changes the absolute values slightly for  $H/C$ , but the trend among spin density and  $H/C$  is preserved.

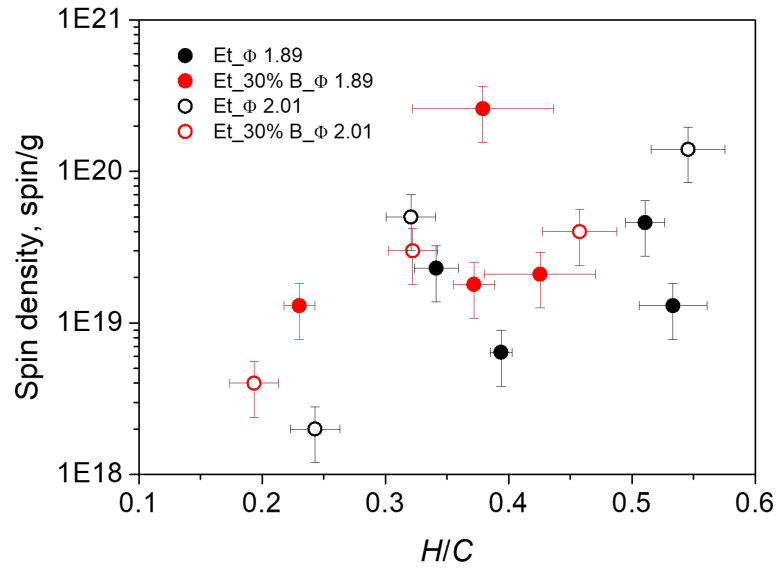


Figure 5.33. Measured spin density by EPR spectroscopy as a function of the  $H/C$  obtained by Raman spectroscopy using the eq. (2).

Within the experimental conditions performed in this study, our measurements show that electron spin density of particles produced by different fuels, i.e., pure ethylene and a mixture of benzene and ethylene, is independent of the mechanism of fuel oxidation. However, it is mainly related to the number of H-atoms available on the particle surface. The chemistry of fuel oxidation and pyrolysis controls the rate at which particles are formed: in the benzene-doped flame the formation of resonantly  $\pi$ -radicals at the flame front, quickens the inception of the particles that rapidly grow to larger sizes in a short residence time. The formation process is only slowed in the pure ethylene flames; nevertheless, particles retain the same surface properties that seem to depend only on particle size.

## CHAPTER 6: CONCLUSIONS

This PhD thesis work dealt with the synthesis and characterization of flame-formed carbon nanoparticles. Specifically, this work focused on the mechanism that leads to onset and early growth of particles in the flame.

The condensed-phase material was collected in an ethylene-rich premixed flame at various residence times during soot particles nucleation and early growth.

A first experimental approach combined the PSD with EPR and Raman spectroscopy of the sampled particles identifying three regimes of particle inception and growth. As the residence time in flame increases, the PSD changes from unimodal to bimodal. In addition to the particle size, the evolution in flame also includes chemical/structural modifications. At lower flame residence times, in the flame region of  $HAB = 7\text{--}8$  mm, the PSD is monomodal, and the particle sizes are less than 4 nm. These particles are made of aromatic components with an average dimension of approximately 1.1 nm and contain an ensemble of weakly interacting paramagnetic species typical of persistent carbon-centred aromatic radicals. These PAHs particles are characterized by zigzag edges that could originate the radicals, explaining both EPR and Raman results. As particle evolution proceeds along the flame, a second particle mode appears, with particles of 4–6 nm in size. The EPR signal becomes stronger and narrower, showing a Lorentzian line shape and the most remarkable propensity to saturate indicated by a quasilinear trend in the corresponding power saturation profile. Raman spectroscopy indicates that the aromatic islands in Mode-II particles are slightly larger than those in Mode-I particles. Both techniques consistently suggest that facing aromatic islands start to interact with each other, resulting in the early formation of stacks and three-dimensional structural organization. In this stacked/clustered structure, among the aromatic molecules a type of bond, called a multicenter covalent-like bond, is possible to be formed. This type of bond is intermediate between a pure covalent bond and a van der Waals interaction. In addition, the radical characteristics of zigzag edges originating from localized  $\pi$ -electrons could also promote clustering between aromatics through  $\pi$ -electron interactions over a stacked structure, as previously suggested by Wang (Wang, 2011). The nucleation and coagulation of Mode-I particles may be enhanced by forming covalent-like bonds among  $\pi$ -radicals, which causes a three-dimensional network to form. Inclusion of these types of interactions in the soot formation mechanism might help identify the elusive and still unresolved steps of carbon

clustering and transformation in a solid particle with a higher three-dimensional structural order.

The last step in particle growth, production of particles larger than 10 nm, is accompanied by a reduction in the paramagnetic spin density. This is consistent with Homann and Wagner's reports, who, using EPR/electron spin resonance spectroscopy, observed a lower radical character of old soot particles than young particles (Homann and Wagner, 1967). These findings may be a consequence of spin interactions produced by the three-dimensional stacking arrangement and a different type of supraparticle organization produced by aggregation of smaller particles and mass addition through surface reactions and persistent nucleation.

Therefore in this first experimental exploration, some information, that improves the understanding of the most critical steps in current soot inception and growth models, has been performed. Besides, the ability to control the underlying physicochemical processes leading to particle clustering/growth is crucial to influencing the order/disorder transformations and thus tailor the magnetic and conductive properties of carbonaceous particles. These results are valid for a deeper understanding of flame formed carbon nanoparticles in producing these materials as an engineered nanomaterial in various fields.

Following this first exploration among the chemical/structural and radical characterization of the particles along the flame, a more in-depth study of the dimerization and aggregation ability of the radical PAHs, found in a flame, has been performed. Specifically, a plausible explanation of stack formation has been theorized. These stacks would then form the three-dimensional structures discussed earlier in the EPR analysis of particles in flame.

Therefore, the thesis work progressed with a theoretical study. DFT-D3 calculations of the self-association of two  $\pi$ -radicals and the corresponding molecules have been performed. The radicals differ for a different level of delocalization of the unpaired electron over the aromatic framework. This difference is crucial in determining the dimerization process, the binding energy, and energy band gap characteristic of the clustering of two various molecular radicals.

Based on MPAN calculations, the results show that  $\pi$  radicals with a partial localization tend to form a  $\sigma$ -dimer. The  $\sigma$ -dimer is characterized by longer length and weaker energy bond than a standard  $\sigma$ -bond. On the other hand, our calculations showed that  $\pi$  radicals with a greater delocalization of the unpaired electron lead to the  $\pi$ -stacking formation. The interaction energy of this dimer resulted prevalently due to Van der Waals contributions. However, additional

interaction energy, attributed to multi-electron/multi-centre bond, has been estimated.

Another relevant result of the computational work is evaluating the effects of the unpaired electron's delocalization and the type of dimerization process on the HOMO-LUMO gap.

The main conclusion has been to assert that the formation of a radical leads to lowering the optical bandgap. The HOMO-LUMO gap further decreases as they form dimers. The obtained gap values are different based on the molecular geometry of the stacked structures and their spin-multiplicity. Nevertheless, the formation of  $\pi$ -stacking induced by delocalized  $\pi$ -radicals could, in part explain some spectroscopic shreds of evidence observed during soot nucleation (Minutolo *et al.*, 2011; Sirignano *et al.*, 2012; Commодо, De Falco, *et al.*, 2015; Commодо, Tessitore, *et al.*, 2015; Mercier *et al.*, 2019).

According to the experiments, flame particles are composed by an ensemble of PAH whose typical size is of the order of ovalene, 1 nm. However, the optical band gap measured for nascent soot particles is commonly much lower than the corresponding cluster of pure ovalene and other characteristic aromatic molecules (Adkins, Giaccari and Miller, 2017; Chen and Wang, 2019; Liu *et al.*, 2019). In this regard, radicals and their dimers into a soot particle may explain such discrepancies.

Therefore, it is clear that radicals have a crucial role in the mechanism of particle formation. Arrived at this point, it is also clear that there are two different types of radicals, and it is equally clear that various structural elements generate the two types of radicals; in this line of research falls the  $^1\text{H}$ -NMR study, carried out in this thesis work.

$^1\text{H}$ - NMR is the most suitable technique to detect and analyze different hydrogens of molecular constituents. The obtained results confirm the presence and the existence of aliphatic moieties and methylene hydrogen ( $-\text{CH}_2$ ), in agreement to the recent experimental observations. Moreover,  $^1\text{H}$ -NMR results confirm the presences of hydrogens atoms that, by an homolytic cleavage/addition, lead to formation of radicals, which in turn differentiate the different path in the nucleation step.

The formation of radicals might be strongly related to the fuel chemical structure and to the environment in which the fuel reacts. For instance, aromatic hydrocarbons fuel during oxidation can be more effective in forming resonantly stabilized  $\pi$ -radicals, e.g., cyclopentadienyl, benzyl or indenyl radicals, in comparison with aliphatic hydrocarbons.

The different propensity of aromatic fuels as compared to aliphatic fuels, in forming such resonantly stabilized radicals, already at the flame front, has motivated the study of benzene as additive to fuel, with the aim to investigate the effects of resonantly stabilized radicals and structures as penta-rings in the formation and subsequent growth of nascent soot particles.

The choice could not fall on a molecule different from benzene, being a field full of aromatics and benzene the first formed aromatic ring.

Therefore, a comparative analysis of radicals in soot particles was performed in two sets of flames; one consists of pure laminar premixed ethylene flame, the other consists of an ethylene/benzene mixture. The comparison was performed at inception and initial growth by EPR and Raman spectroscopy measurements.

By PSD measurements, first detected particles are smaller than 5 nm and grow to larger sizes as residence time increases. In the flame conditions herein investigated the typical trough between the nucleation and growth modes of the size distribution were not observed probably because of the present flames' higher temperature.

Soon after the first appearance of particles, in correspondence to initial particle growth, a narrowing of the ERP spectra occurs, while the spectral line-shape changes from Gaussian to a combination of Gaussian and Lorentzian. This behaviour indicates that electron-electron interactions become stronger as particles grow. Also, as Raman spectroscopy indicates, the aromatic domains' size does not sensibly change along with the flame. Therefore, the EPR line-shape narrowing cannot be ascribed to a greater delocalization of unpaired electrons in larger aromatic domains but has to be ascribed to the formation of stacks of aromatic functional groups hosting free radicals.

Electron spin density shows an inverse dependence on particle size due to a lower radical population during the particle growth process. These findings support the view that both particle inception and the initial growth see the occurrence of covalently stabilized dimers/trimers formation.

A unique inverse proportionality with particle size is observed for the particles' spin density, regardless of the flame equivalence ratio and the addition of benzene to the fuel mixture. Moreover, a correlation is found between spin density and particle  $H/C$ , indicating that paramagnetic centres are dependent on the number of hydrogenated sites on the particle surface, also in this case, regardless of the flame conditions and fuels used.

In conclusion, within the experimental conditions analyzed in this study, particles' electron spin density seems to be independent of the mechanism of fuel

oxidation. However, it is mainly related to the number of H-atoms available on the particle's surface. The chemistry of fuel oxidation and pyrolysis controls the rate at which resonantly  $\pi$ -radicals are formed and consequently the particle inception rate but has a minor effect in controlling the structure and the radical behaviours of the particles.

To conclude, this thesis work has dealt with the study and characterization of carbonaceous particles, focusing mainly on the nucleation process and radicals, determining its "fate". A small step towards a more precise understanding has been made even if the ocean of the uncertain is still immense.



## BIBLIOGRAPHY

- Abid, A. D. *et al.* (2008) 'On evolution of particle size distribution functions of incipient soot in premixed ethylene-oxygen-argon flames', *Combustion and Flame*. doi: 10.1016/j.combustflame.2008.06.009.
- Adkins, E. M., Giaccari, J. A. and Miller, J. H. (2017) 'Computed electronic structure of polynuclear aromatic hydrocarbon agglomerates', *Proceedings of the Combustion Institute*. Elsevier Inc., 36(1), pp. 957–964. doi: 10.1016/j.proci.2016.06.186.
- Adrian, F. J., Cochran, E. L. and Bowers, V. A. (1972) 'Electron spin resonance spectra of ClCO and ClOO', *The Journal of Chemical Physics*. doi: 10.1063/1.1677181.
- Agarwal, A. K. (2007) 'Biofuels (alcohols and biodiesel) applications as fuels for internal combustion engines', *Progress in Energy and Combustion Science*, 33(3), pp. 233–271. doi: 10.1016/j.peccs.2006.08.003.
- Al-Hakkani, M. F. (2020) 'Biogenic copper nanoparticles and their applications: A review', *SN Applied Sciences*. doi: 10.1007/s42452-020-2279-1.
- Alfè, M. *et al.* (2007) 'Similarities and dissimilarities in n-hexane and benzene sooting premixed flames', *Proceedings of the Combustion Institute*. doi: 10.1016/j.proci.2006.07.187.
- Amans, D. *et al.* (2009) 'Nanodiamond synthesis by pulsed laser ablation in liquids', *Diamond and Related Materials*. doi: 10.1016/j.diamond.2008.10.035.
- Amsharov, K. Y. and Jansen, M. (2008) 'A C78 fullerene precursor: Toward the direct synthesis of higher fullerenes', *Journal of Organic Chemistry*, 73(7), pp. 2931–2934. doi: 10.1021/jo7027008.
- Andrius, K. *et al.* (2013) 'Carbon-core silver-shell nanodots as sensitizers for phototherapy and radiotherapy', *Nanotechnology*, 24(32), p. 325103. doi: 10.1088/0957-4484/24/32/325103.
- Anilkumar, P. *et al.* (2012) 'Fullerenes for Applications in Biology and Medicine', *Current Medicinal Chemistry*. doi: 10.2174/092986711795656225.
- Antaris, A. L. *et al.* (2013) 'Ultra-low doses of chirality sorted (6,5) carbon nanotubes for simultaneous tumor imaging and photothermal therapy', *ACS Nano*. doi: 10.1021/nn4006472.
- Arul Dhas, N. and Gedanken, A. (1997) 'Sonochemical Synthesis of Molybdenum Oxide- and Molybdenum Carbide-Silica Nanocomposites', *Chemistry of Materials*, 9(12), pp. 3144–3154. doi: 10.1021/cm9704488.
- Avouris, P. (2010) 'Graphene: Electronic and photonic properties and devices', *Nano Letters*. doi: 10.1021/nl102824h.
- Badrossamay, M. R. *et al.* (2010) 'Nanofiber assembly by rotary jet-spinning', *Nano*

*Letters*. doi: 10.1021/nl101355x.

Baker, M. J., Hughes, C. S. and Hollywood, K. A. (2016) *Biophotonics: Vibrational spectroscopic diagnostics*, *Biophotonics: Vibrational Spectroscopic Diagnostics*. doi: 10.1088/978-1-6817-4071-3.

Baker, R. T. K. *et al.* (1972) 'Nucleation and growth of carbon deposits from the nickel catalyzed decomposition of acetylene', *Journal of Catalysis*. doi: 10.1016/0021-9517(72)90032-2.

Battin-Leclerc, F. (2008) 'Detailed chemical kinetic models for the low-temperature combustion of hydrocarbons with application to gasoline and diesel fuel surrogates', *Progress in Energy and Combustion Science*, 34(4), pp. 440–498. doi: 10.1016/j.pecs.2007.10.002.

Becke, A. D. (1993) 'A new mixing of Hartree-Fock and local density-functional theories', *The Journal of Chemical Physics*. doi: 10.1063/1.464304.

Bennett, B. A. V. *et al.* (2009) 'Computational and experimental study of the effects of adding dimethyl ether and ethanol to nonpremixed ethylene/air flames', *Combustion and Flame*. Elsevier Inc., 156(6), pp. 1289–1302. doi: 10.1016/j.combustflame.2009.01.020.

Bennett, J. E., Mile, B. and Thomas, A. (1965) 'Electron spin resonance spectrum of the phenyl radical prepared by chemical reaction at 77°K', *Chemical Communications (London)*, (12), pp. 265–267. doi: 10.1039/C19650000265.

Bergeron, D. E. *et al.* (2004) 'Stable Cluster Motifs for Nanoscale Chromium Oxide Materials', *Nano Letters*. doi: 10.1021/nl034997q.

Bhandari, J. *et al.* (2019) 'Extensive Soot Compaction by Cloud Processing from Laboratory and Field Observations', *Scientific Reports*. doi: 10.1038/s41598-019-48143-y.

Bhavaripudi, S. *et al.* (2010) 'Role of kinetic factors in chemical vapor deposition synthesis of uniform large area graphene using copper catalyst', *Nano Letters*, 10(10), pp. 4128–4133. doi: 10.1021/nl102355e.

Binet, L. *et al.* (2002) 'Heterogeneous distribution of paramagnetic radicals in insoluble organic matter from the Orgueil and Murchison meteorites', *Geochimica et Cosmochimica Acta*. doi: 10.1016/S0016-7037(02)00983-3.

Blanquart, G. and Pitsch, H. (2009) 'Analyzing the effects of temperature on soot formation with a joint volume-surface-hydrogen model', *Combustion and Flame*. doi: 10.1016/j.combustflame.2009.04.010.

Bockhorn, H. *et al.* (2007) *Combustion generated fine carbonaceous particles, Proceedings of an International Workshop held in Villa Orlandi, Anacapri*. doi: 10.5445/KSP/1000013744.

de Boer, E. (2010) 'Electron Paramagnetic Resonance. Elementary Theory and Practical Applications, J.A. Weil, J.R. Bolton and J.E. Wertz, John Wiley, U.S.A., 1994 xxi + 568 pp., £66.00, ISBN 0-471-57234-9', *Recueil des Travaux Chimiques des Pays-Bas*. doi: 10.1002/recl.19951140115.

- Bolszo, C. D. and McDonell, V. G. (2009) 'Emissions optimization of a biodiesel fired gas turbine', *Proceedings of the Combustion Institute*. The Combustion Institute, 32 II(2), pp. 2949–2956. doi: 10.1016/j.proci.2008.07.042.
- Bonaccorso, F. *et al.* (2010) 'Graphene photonics and optoelectronics', *Nature Photonics*. doi: 10.1038/nphoton.2010.186.
- Bond, T. C. *et al.* (2013) 'Bounding the role of black carbon in the climate system: A scientific assessment', *Journal of Geophysical Research Atmospheres*. doi: 10.1002/jgrd.50171.
- Bonpua, J. *et al.* (2019) 'Flame temperature effect on sp<sup>2</sup> bonds on nascent carbon nanoparticles formed in premixed flames (T<sub>f,max</sub> > 2100 K): A Raman spectroscopy and particle mobility sizing study', *Proceedings of the Combustion Institute*, 37(1), pp. 943–951. doi: 10.1016/j.proci.2018.06.124.
- Boorum, M. M. *et al.* (2001) 'Groundwork for a rational synthesis of C<sub>60</sub>: Cyclodehydrogenation of a C<sub>60</sub>H<sub>30</sub> polyarene', *Science*. doi: 10.1126/science.1064250.
- Borm, P. J. A. *et al.* (2006) *The potential risks of nanomaterials: A review carried out for ECETOC, Particle and Fibre Toxicology*. doi: 10.1186/1743-8977-3-11.
- Bosi, S. *et al.* (2003) 'Fullerene derivatives: An attractive tool for biological applications', *European Journal of Medicinal Chemistry*, 38(11–12), pp. 913–923. doi: 10.1016/j.ejmech.2003.09.005.
- Botero, M. L. *et al.* (2016) 'PAH structure analysis of soot in a non-premixed flame using high-resolution transmission electron microscopy and optical band gap analysis', *Combustion and Flame*. doi: 10.1016/j.combustflame.2015.11.022.
- Botero, M. L. *et al.* (2019) 'Internal structure of soot particles in a diffusion flame', *Carbon*. doi: 10.1016/j.carbon.2018.09.063.
- Bourlinos, A. B. *et al.* (2008) 'Surface functionalized carbogenic quantum dots', *Small*. doi: 10.1002/sml.200700578.
- Bowles, J. F. W. (1997) 'R.M. Cornell and U. Schwertmann The Iron Oxides: Structure, Properties Reactions Occurrence and Uses. Weinheim and New York (VCH Verlagsgesellschaft mbH). 1996, xxxi + 573 pp. Price DM 328.00. ISBN 3-527-28576-8.', in *Mineralogical Magazine*, p. 509. doi: 10.1180/minmag.1997.061.408.20.
- Brabec, C. J. *et al.* (2010) 'Polymer-fullerene bulk-heterojunction solar cells', *Advanced Materials*. doi: 10.1002/adma.200903697.
- Bredas, J. L. (2014) 'Mind the gap!', *Materials Horizons*, 1(1), pp. 17–19. doi: 10.1039/c3mh00098b.
- Brezinsky, K. (1996) 'Gas-phase combustion synthesis of materials', *Symposium (International) on Combustion*. doi: 10.1016/S0082-0784(96)80001-4.
- Briscoe, J. *et al.* (2015) 'Biomass-Derived Carbon Quantum Dot Sensitizers for Solid-State Nanostructured Solar Cells', *Angewandte Chemie - International Edition*, 54(15), pp. 4463–4468. doi: 10.1002/anie.201409290.

British Standards Institution (2017) 'BS EN ISO/IEC 27000:2017', *British Standards Online*, British Standards Institution.

Brivati, J. A., Keen, N. and Symons, M. C. R. (1962) '44. Unstable intermediates. Part XIV. The formyl radical', *Journal of the Chemical Society (Resumed)*. doi: 10.1039/jr9620000237.

Brown, S. P. (2012) 'Applications of high-resolution  $^1\text{H}$  solid-state NMR', *Solid State Nuclear Magnetic Resonance*. Elsevier, 41, pp. 1–27. doi: 10.1016/j.ssnmr.2011.11.006.

Buijnsters, J. G. *et al.* (2009) 'Hydrogen quantification in hydrogenated amorphous carbon films by infrared, Raman, and x-ray absorption near edge spectroscopies', *Journal of Applied Physics*. doi: 10.1063/1.3103326.

Bulat, F. A. *et al.* (2012) 'Hydrogenation and fluorination of graphene models: Analysis via the average local ionization energy', *Journal of Physical Chemistry A*. doi: 10.1021/jp3053604.

Burger, J. L. *et al.* (2015) ' $^1\text{H}$  and  $^{13}\text{C}$  NMR Analysis of Gas Turbine Fuels As Applied to the Advanced Distillation Curve Method', *Energy and Fuels*, 29(8), pp. 4874–4885. doi: 10.1021/acs.energyfuels.5b01035.

Buszman, E. *et al.* (2006) 'EPR examination of  $\text{Zn}^{2+}$  and  $\text{Cu}^{2+}$  binding by pigmented soil fungi *Cladosporium cladosporioides*', *Science of the Total Environment*. doi: 10.1016/j.scitotenv.2005.05.028.

Buzea, C., Pacheco, I. I. and Robbie, K. (2007) 'Nanomaterials and nanoparticles: Sources and toxicity', *Biointerphases*. doi: 10.1116/1.2815690.

Cain, J. *et al.* (2014) 'Molecular characterization of organic content of soot along the centerline of a coflow diffusion flame', *Physical Chemistry Chemical Physics*. doi: 10.1039/c4cp03330b.

Calcote, H. F. (1981) 'Mechanisms of soot nucleation in flames-A critical review', *Combustion and Flame*. doi: 10.1016/0010-2180(81)90159-0.

Calcote, H. F. and Felder, W. (1992) 'A new gas-phase combustion synthesis process for pure metals, alloys, and ceramics', *Symposium (International) on Combustion*. doi: 10.1016/S0082-0784(06)80219-5.

Calemma, V. *et al.* (1995) 'Structural Characterization of Asphaltenes of Different Origins', *Energy and Fuels*, 9(2), pp. 225–230. doi: 10.1021/ef00050a004.

Camenzind, A., Caseri, W. R. and Pratsinis, S. E. (2010) 'Flame-made nanoparticles for nanocomposites', *Nano Today*. doi: 10.1016/j.nantod.2009.12.007.

Cançado, L. G. *et al.* (2004) 'Influence of the atomic structure on the Raman spectra of graphite edges', *Physical Review Letters*. doi: 10.1103/PhysRevLett.93.247401.

Cançado, L. G. *et al.* (2008) 'Geometrical approach for the study of G' band in the Raman spectrum of monolayer graphene, bilayer graphene, and bulk graphite', *Physical Review B - Condensed Matter and Materials Physics*. doi: 10.1103/PhysRevB.77.245408.

Carbone, F., Attoui, M. and Gomez, A. (2016) 'Challenges of measuring nascent soot in

flames as evidenced by high-resolution differential mobility analysis', *Aerosol Science and Technology*. doi: 10.1080/02786826.2016.1179715.

Carotta, M. C. *et al.* (1999) 'Preparation and characterization of nanostructured titania thick films', *Advanced Materials*, 11(11), pp. 943–946. doi: 10.1002/(SICI)1521-4095(199908)11:11<943::AID-ADMA943>3.0.CO;2-L.

Casiraghi, C. *et al.* (2005) 'Bonding in hydrogenated diamond-like carbon by Raman spectroscopy', *Diamond and Related Materials*, 14(3–7), pp. 1098–1102. doi: 10.1016/j.diamond.2004.10.030.

Cassell, A. M. *et al.* (1999) 'Large Scale CVD Synthesis of Single-Walled Carbon Nanotubes', *Journal of Physical Chemistry B*. doi: 10.1021/jp990957s.

Chen, D. and Wang, H. (2019) 'HOMO-LUMO Gaps of Homogeneous Polycyclic Aromatic Hydrocarbon Clusters', *Journal of Physical Chemistry C*. doi: 10.1021/acs.jpcc.9b08300.

Chen, H., Shuai, S. J. and Wang, J. X. (2007) 'Study on combustion characteristics and PM emission of diesel engines using ester-ethanol-diesel blended fuels', *Proceedings of the Combustion Institute*, 31 II, pp. 2981–2989. doi: 10.1016/j.proci.2006.07.130.

Chen, Z. *et al.* (2007) 'High temperature ignition and combustion enhancement by dimethyl ether addition to methane-air mixtures', *Proceedings of the Combustion Institute*, 31 I(1), pp. 1215–1222. doi: 10.1016/j.proci.2006.07.177.

Choi, B. C. and Foster, D. E. (2006) 'Overview of the effect of catalyst formulation and exhaust gas compositions on soot oxidation in DPF', *Journal of Mechanical Science and Technology*. doi: 10.1007/BF02916194.

Chung, D. D. L. (2002) 'Review: Graphite', *Journal of Materials Science*. doi: 10.1023/A:1014915307738.

Chung, S. H. and Violi, A. (2010) 'Nucleation of fullerenes as a model for examining the formation of soot', *Journal of Chemical Physics*. doi: 10.1063/1.3345630.

Chung, S. H. and Violi, A. (2011) 'Peri-condensed aromatics with aliphatic chains as key intermediates for the nucleation of aromatic hydrocarbons', *Proceedings of the Combustion Institute*. doi: 10.1016/j.proci.2010.06.038.

Church, D. F. and Pryor, W. A. (1985) 'Free-radical chemistry of cigarette smoke and its toxicological implications', *Environmental Health Perspectives*. doi: 10.1289/ehp.8564111.

Ćirić, L. *et al.* (2009) 'Towards electron spin resonance of mechanically exfoliated graphene', *Physica Status Solidi (B) Basic Research*. doi: 10.1002/pssb.200982325.

Cochran, E. L., Adrian, F. J. and Bowers, V. A. (1962) 'ESR detection of the cyanogen and methylene imino free radicals', *The Journal of Chemical Physics*. doi: 10.1063/1.1701294.

Commodo, M., Tessitore, G., *et al.* (2015) 'Further details on particle inception and growth in premixed flames', *Proceedings of the Combustion Institute*. The Combustion

Institute, 35(2), pp. 1795–1802. doi: 10.1016/j.proci.2014.06.004.

Commodo, M., De Falco, G., *et al.* (2015) ‘Physicochemical evolution of nascent soot particles in a laminar premixed flame: From nucleation to early growth’, *Combustion and Flame*. Elsevier Ltd., 162(10), pp. 3854–3863. doi: 10.1016/j.combustflame.2015.07.022.

Commodo, M. *et al.* (2017) ‘Illuminating the earliest stages of the soot formation by photoemission and Raman spectroscopy’, *Combustion and Flame*. Elsevier Inc., 181, pp. 188–197. doi: 10.1016/j.combustflame.2017.03.020.

Commodo, M. *et al.* (2018) ‘Structure and size of soot nanoparticles in laminar premixed flames at different equivalence ratios’, *Fuel*. Elsevier, 216, pp. 456–462. doi: 10.1016/j.fuel.2017.12.032.

Commodo, M. *et al.* (2019) ‘On the early stages of soot formation: Molecular structure elucidation by high-resolution atomic force microscopy’, *Combustion and Flame*. Elsevier Inc., 205, pp. 154–164. doi: 10.1016/j.combustflame.2019.03.042.

Connor, E. E. *et al.* (2005) ‘Gold nanoparticles are taken up by human cells but do not cause acute cytotoxicity’, *Small*. doi: 10.1002/sml.200400093.

Cui, X. *et al.* (2011) ‘Liquid-phase exfoliation, functionalization and applications of graphene’, *Nanoscale*. doi: 10.1039/c1nr10127g.

D’Alessio, A. *et al.* (1992) ‘Precursor formation and soot inception in premixed ethylene flames’, *Symposium (International) on Combustion*. doi: 10.1016/S0082-0784(06)80115-3.

D’Alessio, A. *et al.* (2005) ‘Surface deposition and coagulation efficiency of combustion generated nanoparticles in the size range from 1 to 10 nm’, in *Proceedings of the Combustion Institute*. doi: 10.1016/j.proci.2004.08.267.

D’Anna, A. *et al.* (2001) ‘A reaction pathway for nanoparticle formation in rich premixed flames’, *Combustion and Flame*, 127(1–2), pp. 1995–2003. doi: 10.1016/S0010-2180(01)00303-0.

D’Anna, A. (2009) ‘Combustion-formed nanoparticles’, *Proceedings of the Combustion Institute*. Elsevier Inc., 32 I(1), pp. 593–613. doi: 10.1016/j.proci.2008.09.005.

D’Anna, A., Sirignano, M. and Kent, J. (2010) ‘A model of particle nucleation in premixed ethylene flames’, *Combustion and Flame*. The Combustion Institute., 157(11), pp. 2106–2115. doi: 10.1016/j.combustflame.2010.04.019.

D’Anna, A. and Violi, A. (2005) ‘Detailed modeling of the molecular growth process in aromatic and aliphatic premixed flames’, *Energy and Fuels*. doi: 10.1021/ef0499675.

D’Anna, A., Violi, A. and D’Alessio, A. (2000) ‘Modeling the rich combustion of aliphatic hydrocarbons’, *Combustion and Flame*. doi: 10.1016/S0010-2180(99)00163-7.

Decesari, S. *et al.* (2000) ‘Characterization of water-soluble organic compounds in atmospheric aerosol: A new approach’, *Journal of Geophysical Research Atmospheres*, 105(D1), pp. 1481–1489. doi: 10.1029/1999JD900950.

Demirbas, A. (2007) ‘Progress and recent trends in biofuels’, *Progress in Energy and*

- Combustion Science*, 33(1), pp. 1–18. doi: 10.1016/j.pecs.2006.06.001.
- Derfus, A. M., Chan, W. C. W. and Bhatia, S. N. (2004) ‘Probing the Cytotoxicity of Semiconductor Quantum Dots’, *Nano Letters*, 4(1), pp. 11–18. doi: 10.1021/nl0347334.
- Desgroux, P. *et al.* (2017) ‘Comparative study of the soot formation process in a “nucleation” and a “sooting” low pressure premixed methane flame’, *Combustion and Flame*. doi: 10.1016/j.combustflame.2017.05.034.
- Dhand, C. *et al.* (2015) ‘Methods and strategies for the synthesis of diverse nanoparticles and their applications: A comprehensive overview’, *RSC Advances*. Royal Society of Chemistry, 5(127), pp. 105003–105037. doi: 10.1039/c5ra19388e.
- Donaldson, K. *et al.* (2004) ‘Nanotoxicology’, *Occupational and Environmental Medicine*, 61(9), pp. 727–728. doi: 10.1136/oem.2004.013243.
- Donnet, J. B. *et al.* (2006) ‘Synthesis of large single crystal diamond using combustion-flame method’, *Carbon*, 44(2), pp. 374–380. doi: 10.1016/j.carbon.2005.06.041.
- Dovesi, R. *et al.* (2018) ‘Quantum-mechanical condensed matter simulations with CRYSTAL’, *Wiley Interdisciplinary Reviews: Computational Molecular Science*. doi: 10.1002/wcms.1360.
- Durand, E. *et al.* (2010) ‘Effect of chemical composition on asphaltenes aggregation’, *Energy and Fuels*, 24(2), pp. 1051–1062. doi: 10.1021/ef900599v.
- Dutta Majumdar, R. *et al.* (2013) ‘Validation of the Yen-Mullins model of athabasca oil-sands asphaltenes using solution-state <sup>1</sup>H NMR relaxation and 2D HSQC spectroscopy’, *Energy and Fuels*. doi: 10.1021/ef401412w.
- Dutta Majumdar, R. *et al.* (2016) ‘Single-Core PAHs in Petroleum- and Coal-Derived Asphaltene: Size and Distribution from Solid-State NMR Spectroscopy and Optical Absorption Measurements’, *Energy and Fuels*, 30(9), pp. 6892–6906. doi: 10.1021/acs.energyfuels.5b02815.
- Dutta Majumdar, R. *et al.* (2017) ‘Insights into asphaltene aggregate structure using ultrafast MAS solid-state <sup>1</sup>H NMR spectroscopy’, *Fuel*. Elsevier Ltd, 193, pp. 359–368. doi: 10.1016/j.fuel.2016.12.082.
- Eaton, G. R. *et al.* (2010) *Quantitative EPR*, *Quantitative EPR*. doi: 10.1007/978-3-211-92948-3.
- Echavarria, C. A. *et al.* (2011) ‘Evolution of soot size distribution in premixed ethylene/air and ethylene/benzene/air flames: Experimental and modeling study’, *Combustion and Flame*. The Combustion Institute., 158(1), pp. 98–104. doi: 10.1016/j.combustflame.2010.07.021.
- Eddings, E. G. *et al.* (2005) ‘Formulation of a surrogate for the simulation of Jet fuel pool fires’, *Combustion Science and Technology*, 177(4), pp. 715–739. doi: 10.1080/00102200590917248.
- Ehrman, S. H., Friedlander, S. K. and Zachariah, M. R. (1999) ‘Phase segregation in binary SiO<sub>2</sub>/TiO<sub>2</sub> and SiO<sub>2</sub>/Fe<sub>2</sub>O<sub>3</sub> nanoparticle aerosols formed in a premixed flame’,

Endo, M. and Kroto, H. W. (1992) 'Formation of carbon nanofibers', *Journal of Physical Chemistry*. doi: 10.1021/j100196a017.

Enoki, T. (2012) 'Role of edges in the electronic and magnetic structures of nanographene', *Physica Scripta*. doi: 10.1088/0031-8949/2012/T146/014008.

Environmental Protection Agency (EPA) (1999) 'Nitrogen oxides (NO<sub>x</sub>), why and how they are controlled', *Epa-456/F-99-006R*, (November), p. 48. doi: EPA 456/F-99-006R.

European Commission (2011) 'European Commission, 2011a. Commission recommendation of 18 october 2011 on the definition of nanomaterial (2011/696/EU). Off. J. Eur. Union L 275, 38–40. [https://ec.europa.eu/research/industrial\\_technologies/pdf/policy/commission-recommendation-on-the-](https://ec.europa.eu/research/industrial_technologies/pdf/policy/commission-recommendation-on-the-)', *Official Journal of the European Union*. doi: 10.2777/13162.

Faccinetto, A. *et al.* (2011) 'High-sensitivity detection of polycyclic aromatic hydrocarbons adsorbed onto soot particles using laser desorption/laser ionization/time-of-flight mass spectrometry: An approach to studying the soot inception process in low-pressure flames', *Combustion and Flame*. doi: 10.1016/j.combustflame.2010.08.012.

De Falco, G. *et al.* (2015) 'Flame-formed carbon nanoparticles: Morphology, interaction forces, and hamaker constant from AFM', *Aerosol Science and Technology*, 49(5), pp. 281–289. doi: 10.1080/02786826.2015.1022634.

De Falco, G. *et al.* (2017) 'The evolution of soot particles in premixed and diffusion flames by thermophoretic particle densitometry', *Proceedings of the Combustion Institute*. doi: 10.1016/j.proci.2016.07.108.

De Falco, G. *et al.* (2020) 'Probing soot structure and electronic properties by optical spectroscopy', *Fuel*, 259. doi: 10.1016/j.fuel.2019.116244.

Fang, T. and Lee, C. F. (2009) 'Bio-diesel effects on combustion processes in an HSDI diesel engine using advanced injection strategies', *Proceedings of the Combustion Institute*. The Combustion Institute, 32 II(2), pp. 2785–2792. doi: 10.1016/j.proci.2008.07.031.

Faraday, M. (1857) 'Experimental Relations of Gold (and other Metals) to Light.', *Phil. Trans. R. Soc.*

'FDA Guidance on NanotechnologyDOCUMENT: Guidance for Industry Considering Whether an FDA-Regulated Product Involves the Application of Nanotechnology' (2011) *Biotechnology Law Report*. doi: 10.1089/blr.2011.9787.

Feng, T. *et al.* (2016) 'Correction to Charge-Convertible Carbon Dots for Imaging-Guided Drug Delivery with Enhanced in Vivo Cancer Therapeutic Efficiency', *ACS Nano*, 10(5), p. 5587. doi: 10.1021/acsnano.6b02794.

Ferrari, A. C. *et al.* (2006) 'Raman spectrum of graphene and graphene layers', *Physical Review Letters*. doi: 10.1103/PhysRevLett.97.187401.

Ferrari, A. C. and Basko, D. M. (2013) 'Raman spectroscopy as a versatile tool for



- studying the properties of graphene', *Nature Nanotechnology*. Nature Publishing Group, 8(4), pp. 235–246. doi: 10.1038/nnano.2013.46.
- Ferrari, A. C. and Robertson, J. (2001a) 'Origin of the 1150 – cm<sup>-1</sup> Raman mode in nanocrystalline diamond', *Physical Review B - Condensed Matter and Materials Physics*. doi: 10.1103/PhysRevB.63.121405.
- Ferrari, A. C. and Robertson, J. (2001b) 'Resonant Raman spectroscopy of disordered, amorphous, and diamondlike carbon', *Physical Review B - Condensed Matter and Materials Physics*, 64(7), pp. 1–13. doi: 10.1103/PhysRevB.64.075414.
- Ferroni, M. *et al.* (1997) 'Gas-sensing applications of W-Ti-O-based nanosized thin films prepared by r.f. reactive sputtering', *Sensors and Actuators, B: Chemical*. doi: 10.1016/S0925-4005(97)00173-1.
- Fessenden, R. W. and Schuler, R. H. (1963) 'Electron spin resonance studies of transient alkyl radicals', *The Journal of Chemical Physics*. doi: 10.1063/1.1701415.
- Feynman, R. (1959) 'Conclusion : “ Plenty of Room at the Bottom ”', in *Engineering and Science*, pp. 22–36.
- Feynman, R. P. (2002) 'There's plenty of room at the bottom: An invitation to enter a new field of physics', in *Handbook of Nanoscience, Engineering, and Technology*.
- Frenklach, M. *et al.* (1985) 'Detailed kinetic modeling of soot formation in shock-tube pyrolysis of acetylene', *Symposium (International) on Combustion*. doi: 10.1016/S0082-0784(85)80578-6.
- Frenklach, M. (2002a) 'Reaction mechanism of soot formation in flames', *Physical Chemistry Chemical Physics*, 4(11), pp. 2028–2037. doi: 10.1039/b110045a.
- Frenklach, M. (2002b) 'Reaction mechanism of soot formation in flames', in *Physical Chemistry Chemical Physics*. doi: 10.1039/b110045a.
- Frenklach, M. *et al.* (2018) 'Detailed, sterically-resolved modeling of soot oxidation: Role of O atoms, interplay with particle nanostructure, and emergence of inner particle burning', *Combustion and Flame*. doi: 10.1016/j.combustflame.2017.10.012.
- Frenklach, M. and Mebel, A. M. (2020) 'On the mechanism of soot nucleation', *Physical Chemistry Chemical Physics*. doi: 10.1039/d0cp00116c.
- Frenklach, M., Schuetz, C. A. and Ping, J. (2005) 'Migration mechanism of aromatic-edge growth', *Proceedings of the Combustion Institute*. doi: 10.1016/j.proci.2004.07.048.
- Frenklach, M. and Wang, H. (1991) 'Detailed modeling of soot particle nucleation and growth', *Symposium (International) on Combustion*. doi: 10.1016/S0082-0784(06)80426-1.
- Frenklach, M. and Wang, H. (1994) *Detailed mechanism and modeling of soot particle formation*, *Springer Series in Chemical Physics*. doi: 10.1007/978-3-642-85167-4\_10.
- Galano, A. (2010) 'Carbon nanotubes: Promising agents against free radicals', *Nanoscale*. doi: 10.1039/b9nr00364a.

- Gao, F. W. *et al.* (2016) ‘Two-electron/24-center (2e/24c) bonding in novel diradical  $\pi$ -dimers’, *Physical Chemistry Chemical Physics*. Royal Society of Chemistry, 18(42), pp. 29041–29044. doi: 10.1039/c6cp05410b.
- Gao, W. and Li, Z. (2009) ‘Nanostructures of zinc oxide’, *International Journal of Nanotechnology*, 6(3–4), pp. 245–257. doi: 10.1504/IJNT.2009.022917.
- Geckeler, K. E. and Samal, S. (1999) ‘Syntheses and properties of macromolecular fullerenes, a review’, *Polymer International*. doi: 10.1002/(sici)1097-0126(199909)48:9<743::aid-pi246>3.3.co;2-w.
- Gentile, F. S. *et al.* (2020) ‘Soot inception: A DFT study of  $\sigma$  and  $\pi$  dimerization of resonantly stabilized aromatic radicals’, *Fuel*. Elsevier, 279(September 2019), p. 118491. doi: 10.1016/j.fuel.2020.118491.
- Gleiter, H. (2000) ‘Nanostructured materials: basic concepts and microstructure’, *Acta Materialia*, 48(1), pp. 1–29. doi: 10.1016/S1359-6454(99)00285-2.
- Goenka, S., Sant, V. and Sant, S. (2014) ‘Graphene-based nanomaterials for drug delivery and tissue engineering’, *Journal of Controlled Release*. doi: 10.1016/j.jconrel.2013.10.017.
- Gogotsi, Y. (2017) *Nanomaterials handbook, Second edition, Nanomaterials Handbook, Second Edition*. doi: 10.1201/9781315371795.
- Gokarna, A. *et al.* (2014) ‘Highly crystalline urchin-like structures made of ultra-thin zinc oxide nanowires’, *RSC Advances*. doi: 10.1039/c4ra06327a.
- Gomez, A., Sidebotham, G. and Glassman, I. (1984) ‘Sooting behavior in temperature-controlled laminar diffusion flames’, *Combustion and Flame*. doi: 10.1016/0010-2180(84)90077-4.
- Goodman, C. M. *et al.* (2004) ‘Toxicity of gold nanoparticles functionalized with cationic and anionic side chains’, *Bioconjugate Chemistry*, 15(4), pp. 897–900. doi: 10.1021/bc049951i.
- Gopinath, P. and Gore, J. (2007) ‘Chemical kinetic considerations for postflame synthesis of carbon nanotubes in premixed flames using a support catalyst’, *Combustion and Flame*. doi: 10.1016/j.combustflame.2006.05.004.
- Gore and Sane, A. (2011) ‘Flame Synthesis of Carbon Nanotubes’, in *Carbon Nanotubes - Synthesis, Characterization, Applications*. doi: 10.5772/21012.
- Graetz, J. *et al.* (2003) ‘Highly reversible lithium storage in nanostructured silicon’, *Electrochemical and Solid-State Letters*, 6(9), pp. 194–197. doi: 10.1149/1.1596917.
- Grätzel, M. (2003) ‘Dye-sensitized solar cells’, *Journal of Photochemistry and Photobiology C: Photochemistry Reviews*. doi: 10.1016/S1389-5567(03)00026-1.
- Griller, D. and Ingold, K. U. (1976) ‘Persistent Carbon-Centered Radicals’, *Accounts of Chemical Research*, 9(1), pp. 13–19. doi: 10.1021/ar50097a003.
- Grimme, S. *et al.* (2016) ‘Dispersion-Corrected Mean-Field Electronic Structure Methods’, *Chemical Reviews*. doi: 10.1021/acs.chemrev.5b00533.

- Grotheer, H. H., Wolf, K. and Hoffmann, K. (2011) 'Photoionization mass spectrometry for the investigation of combustion generated nascent nanoparticles and their relation to laser induced incandescence', in *Applied Physics B: Lasers and Optics*. doi: 10.1007/s00340-011-4403-9.
- Guillén, M. D., Díaz, C. and Blanco, C. G. (1998) 'Characterization of coal tar pitches with different softening points by  $^1\text{H}$  NMR: Role of the different kinds of protons in the thermal process', *Fuel Processing Technology*. doi: 10.1016/S0378-3820(98)00080-0.
- Guillén, M. D., Díaz, C. and Blanco, C. G. (1998) 'Characterization of coal tar pitches with different softening points by NMR', *Fuel Processing Technology*, 58(1), pp. 1–15. doi: 10.1016/S0378-3820(98)00080-0.
- Gulino, A. *et al.* (1996) 'Influence of metal-metal bonds on electron spectra of  $\text{MoO}_2$  and  $\text{WO}_2$ ', *Journal of the Chemical Society - Faraday Transactions*, 92(12), pp. 2137–2141. doi: 10.1039/FT9969202137.
- Han, Y. *et al.* (2015) 'Non-metal single/dual doped carbon quantum dots: A general flame synthetic method and electro-catalytic properties', *Nanoscale*. doi: 10.1039/c4nr07116f.
- Hansen, N. *et al.* (2011) 'Fuel-structure dependence of benzene formation processes in premixed flames fueled by  $\text{C}_6\text{H}_{12}$  isomers', *Proceedings of the Combustion Institute*. doi: 10.1016/j.proci.2010.05.056.
- Happold, J., Grotheer, H. H. and Aigner, M. (2007) 'Distinction of gaseous soot precursor molecules and soot precursor particles through photoionization mass spectrometry', *Rapid Communications in Mass Spectrometry*. doi: 10.1002/rcm.2955.
- Harris, S. J. and Weiner, A. M. (1985) 'Chemical Kinetics of Soot Particle Growth', *Annual Review of Physical Chemistry*. doi: 10.1146/annurev.pc.36.100185.000335.
- Haynes, B. S., Jander, H. and Wagner, H. G. (1980) 'Optical Studies of Soot-Formation Processes in Premixed Flames', *Berichte der Bunsengesellschaft für physikalische Chemie*. doi: 10.1002/bbpc.19800840613.
- Haynes, B. S. and Wagner, H. G. (1981) 'Soot formation', *Progress in Energy and Combustion Science*. doi: 10.1016/0360-1285(81)90001-0.
- Hebard, A. F. (1993) 'Buckminsterfullerene', *Annual Review of Materials Science*. doi: 10.1146/annurev.ms.23.080193.001111.
- Herdman, J. D. and Miller, J. H. (2008) 'Intermolecular potential calculations for polynuclear aromatic hydrocarbon clusters', *Journal of Physical Chemistry A*. doi: 10.1021/jp800483h.
- Herring, P. *et al.* (2013) 'Paramagnetic centers in particulate formed from the oxidative pyrolysis of 1-methylnaphthalene in the presence of  $\text{Fe(III)2O}_3$  nanoparticles', *Combustion and Flame*. doi: 10.1016/j.combustflame.2013.06.025.
- Hinds, W. C. (1982) 'Aerosol technology: properties, behaviour, and measurement of airborne particles.'
- Hirose, Y., Amanuma, S. and Komaki, K. (1990) 'The synthesis of high-quality diamond

in combustion flames', *Journal of Applied Physics*, 68(12), pp. 6401–6405. doi: 10.1063/1.346859.

Hirose, Y. and Terasawa, Y. (1986) 'Synthesis of diamond thin films by thermal cvd using organic compounds', *Japanese Journal of Applied Physics*. doi: 10.1143/JJAP.25.L519.

Hochella, M. F., Spencer, M. G. and Jones, K. L. (2015) 'Nanotechnology: Nature's gift or scientists' brainchild?', *Environmental Science: Nano*. Royal Society of Chemistry, 2(2), pp. 114–119. doi: 10.1039/c4en00145a.

Hola, K. *et al.* (2014) 'Photoluminescence effects of graphitic core size and surface functional groups in carbon dots: COO- induced red-shift emission', *Carbon*. doi: 10.1016/j.carbon.2014.01.008.

Homann, K. H. (1998) 'Fullerenes and soot formation - New pathways to large particles in flames', *Angewandte Chemie - International Edition*. doi: 10.1002/(SICI)1521-3773(19981002)37:18<2434::AID-ANIE2434>3.0.CO;2-L.

Homann, K. H. and Wagner, H. G. (1967) 'Some new aspects of the mechanism of carbon formation in premixed flames', *Symposium (International) on Combustion*, 11(1), pp. 371–379. doi: [https://doi.org/10.1016/S0082-0784\(67\)80161-9](https://doi.org/10.1016/S0082-0784(67)80161-9).

Hone, J. *et al.* (1999) 'Thermal conductivity of single-walled carbon nanotubes', *Physical Review B - Condensed Matter and Materials Physics*. doi: 10.1103/PhysRevB.59.R2514.

Hou, D. and You, X. (2017) 'Reaction kinetics of hydrogen abstraction from polycyclic aromatic hydrocarbons by H atoms', *Physical Chemistry Chemical Physics*. doi: 10.1039/c7cp04964a.

Houston Miller, J., Smyth, K. C. and Mallard, W. G. (1985) 'Calculations of the dimerization of aromatic hydrocarbons: Implications for soot formation', *Symposium (International) on Combustion*. doi: 10.1016/S0082-0784(85)80604-4.

Howard, J. B. (1991) 'Carbon addition and oxidation reactions in heterogeneous combustion and soot formation', *Symposium (International) on Combustion*. doi: 10.1016/S0082-0784(06)80371-1.

Howard, J. B. *et al.* (1992) 'Fullerenes synthesis in combustion', *Carbon*. doi: 10.1016/0008-6223(92)90061-Z.

Hu, S. *et al.* (2011) 'Laser synthesis and size tailor of carbon quantum dots', *Journal of Nanoparticle Research*. doi: 10.1007/s11051-011-0638-y.

Hu, S. L. *et al.* (2009) 'One-step synthesis of fluorescent carbon nanoparticles by laser irradiation', *Journal of Materials Chemistry*. doi: 10.1039/b812943f.

Huang, C. *et al.* (2009) 'Study of dimethyl ether homogeneous charge compression ignition combustion process using a multi-dimensional computational fluid dynamics model', *International Journal of Thermal Sciences*. Elsevier Ltd, 48(9), pp. 1814–1822. doi: 10.1016/j.ijthermalsci.2009.02.006.

Huang, S. Y. (1995) 'Rocking Chair Lithium Battery Based on Nanocrystalline TiO[sub 2] (Anatase)', *Journal of The Electrochemical Society*, 142(9), p. L142. doi:

10.1149/1.2048726.

Iavarone, S. *et al.* (2017) 'Molecular dynamics simulations of incipient carbonaceous nanoparticle formation at flame conditions', *Combustion Theory and Modelling*, 21(1). doi: 10.1080/13647830.2016.1242156.

Iijima, S. (1991) 'Helical microtubules of graphitic carbon', *Nature*. doi: 10.1038/354056a0.

Iijima, S. and Ichihashi, T. (1993) 'Single-shell carbon nanotubes of 1-nm diameter', *Nature*. doi: 10.1038/363603a0.

Inagaki, M. (2013) *Chapter 2.1 - Advanced Carbon Materials, Handbook of Advanced Ceramics*.

Ingram, von D. J. E. (1961) 'Free Radicals as Studied by Electron Spin Resonance', *Angewandte Chemie*. doi: 10.1002/ange.19610731020.

Irimiea, C. *et al.* (2019) 'Unveiling trends in soot nucleation and growth: When secondary ion mass spectrometry meets statistical analysis', *Carbon*. doi: 10.1016/j.carbon.2018.12.015.

James, T. L. (1998) 'Chapter 1 Fundamentals of NMR', *Control*.

Jawhari, T., Roid, A. and Casado, J. (1995) 'Raman spectroscopic characterization of some commercially available carbon black materials', *Carbon*. doi: 10.1016/0008-6223(95)00117-V.

Jeevanandam, J. *et al.* (2018) 'Review on nanoparticles and nanostructured materials: History, sources, toxicity and regulations', *Beilstein Journal of Nanotechnology*. doi: 10.3762/bjnano.9.98.

Johansson, K. O. *et al.* (2016) 'Formation and emission of large furans and oxygenated hydrocarbons from flames', *Proceedings of the National Academy of Sciences of the United States of America*. doi: 10.1073/pnas.1604772113.

Johansson, K. O. *et al.* (2017) 'Radical-radical reactions, pyrene nucleation, and incipient soot formation in combustion', *Proceedings of the Combustion Institute*. doi: 10.1016/j.proci.2016.07.130.

Johansson, K. O. *et al.* (2018) 'Resonance-stabilized hydrocarbon-radical chain reactions may explain soot inception and growth', *Science*. doi: 10.1126/science.aat3417.

Joly, V. L. J. *et al.* (2010) 'Effect of electron localization on the edge-state spins in a disordered network of nanographene sheets', *Physical Review B - Condensed Matter and Materials Physics*. doi: 10.1103/PhysRevB.81.115408.

Jones, C. C. *et al.* (2004) 'Effects of air/fuel combustion ratio on the polycyclic aromatic hydrocarbon content of carbonaceous soots from selected fuels', *Carbon*, 42(12–13), pp. 2471–2484. doi: 10.1016/j.carbon.2004.04.042.

Kammler, H. K., Mädler, L. and Pratsinis, S. E. (2001) 'Flame synthesis of nanoparticles', *Chemical Engineering and Technology*. doi: 10.1002/1521-4125(200106)24:6<583::AID-CEAT583>3.0.CO;2-H.

- Kasai, P. H., Hedaya, E. and Whipple, E. B. (1969) 'Electron spin resonance study of phenyl radicals isolated in an argon matrix at 4.deg.K', *Journal of the American Chemical Society*. American Chemical Society, 91(16), pp. 4364–4368. doi: 10.1021/ja01044a008.
- Kataura, H. *et al.* (2001) 'High-yield fullerene encapsulation in single-wall carbon nanotubes', *Synthetic Metals*. doi: 10.1016/S0379-6779(00)00707-4.
- Kay, A. and Grätzel, M. (1996) 'Low cost photovoltaic modules based on dye sensitized nanocrystalline titanium dioxide and carbon powder', *Solar Energy Materials and Solar Cells*, 44(1), pp. 99–117. doi: 10.1016/0927-0248(96)00063-3.
- Keller, A., Kovacs, R. and Homann, K. H. (2000) 'Large molecules, ions, radicals and small soot particles in fuel-rich hydrocarbon flames. Part IV. Large polycyclic aromatic hydrocarbons and their radicals in a fuel-rich benzene-oxygen flame', *Physical Chemistry Chemical Physics*. doi: 10.1039/a908190i.
- Kennedy, I. M. (1997) 'Models of soot formation and oxidation', *Progress in Energy and Combustion Science*. doi: 10.1016/S0360-1285(97)00007-5.
- Kennedy, I. M. (2007) 'The health effects of combustion-generated aerosols', *Proceedings of the Combustion Institute*. doi: 10.1016/j.proci.2006.08.116.
- Kertesz, M. (2019) 'Pancake Bonding: An Unusual Pi-Stacking Interaction', *Chemistry - A European Journal*, 25(2), pp. 400–416. doi: 10.1002/chem.201802385.
- Kharisov, B. I. *et al.* (2019) 'General Data on Carbon Allotropes', in *Carbon Allotropes: Metal-Complex Chemistry, Properties and Applications*. doi: 10.1007/978-3-030-03505-1\_1.
- Kholghy, M. R., Kelesidis, G. A. and Pratsinis, S. E. (2018) 'Reactive polycyclic aromatic hydrocarbon dimerization drives soot nucleation', *Physical Chemistry Chemical Physics*. doi: 10.1039/c7cp07803j.
- Kidambi, P. R. *et al.* (2012) 'The parameter space of graphene chemical vapor deposition on polycrystalline Cu', *Journal of Physical Chemistry C*. doi: 10.1021/jp303597m.
- Kim, D.-H. *et al.* (2007) 'Thermal Formation of Polycyclic Aromatic Hydrocarbons from Cyclopentadiene (CPD)', *Environmental Engineering Research*. doi: 10.4491/eer.2007.12.5.211.
- Kim, H. and Cho, J. (2008) 'Superior lithium electroactive mesoporous Si@Carbon core-shell nanowires for lithium battery anode material', *Nano Letters*, 8(11), pp. 3688–3691. doi: 10.1021/nl801853x.
- Kind, H. *et al.* (2002) 'Nanowire ultraviolet photodetectors and optical switches', *Advanced Materials*, 14(2), pp. 158–160. doi: 10.1002/1521-4095(20020116)14:2<158::AID-ADMA158>3.0.CO;2-W.
- Kittelson, D. B. (2001) 'Recent Measurements of Nanoparticle Emissions from Engines', *Current Research on Diesel Exhaust Particles Japan Association of Aerosol Science and Technology*.
- Klages, C.-P. (2008) 'Chemical Vapor Deposition of Diamond Films', in *Handbook of*

*Ceramic Hard Materials*. doi: 10.1002/9783527618217.ch13.

Klein-Douwel, R. J. H. *et al.* (2009) 'Soot and chemiluminescence in diesel combustion of bio-derived, oxygenated and reference fuels', *Proceedings of the Combustion Institute*. The Combustion Institute, 32 II(2), pp. 2817–2825. doi: 10.1016/j.proci.2008.06.140.

Kodu, M. *et al.* (2016) 'Highly sensitive NO<sub>2</sub> sensors by pulsed laser deposition on graphene', *Applied Physics Letters*. doi: 10.1063/1.4962959.

Konnov, A. A., Dyakov, I. V. and De Ruyck, J. (2006) 'Probe sampling measurements of NO in CH<sub>4</sub>+O<sub>2</sub>+N<sub>2</sub> flames doped with NH<sub>3</sub>', *Combustion Science and Technology*, 178(6), pp. 1143–1164. doi: 10.1080/00102200500296788.

Kroto, H. W. *et al.* (1985) 'C<sub>60</sub>: Buckminsterfullerene', *Nature*. doi: 10.1038/318162a0.

Kroto, H. W. (1992) 'Carbon onions introduce new flavour to fullerene studies', *Nature*. doi: 10.1038/359670a0.

Kubicki, J. D. (2006) 'Molecular simulations of benzene and PAH interactions with soot', *Environmental Science and Technology*. doi: 10.1021/es051083s.

Kusakabe, K. and Maruyama, M. (2003) 'Magnetic nanographite', *Physical Review B - Condensed Matter and Materials Physics*. doi: 10.1103/PhysRevB.67.092406.

Kwon, W. *et al.* (2014) 'Size-controlled soft-template synthesis of carbon nanodots toward versatile photoactive materials', *Small*, 10(3), pp. 506–513. doi: 10.1002/sml.201301770.

Kwon, W. *et al.* (2015) 'Control of Photoluminescence of Carbon Nanodots via Surface Functionalization using Para-substituted Anilines', *Scientific Reports*. doi: 10.1038/srep12604.

Lamprecht, A., Atakan, B. and Kohse-Höinghaus, K. (2000) 'Fuel-rich flame chemistry in low-pressure cyclopentene flames', *Proceedings of the Combustion Institute*. doi: 10.1016/S0082-0784(00)80584-6.

Lapuerta, M., Armas, O. and Rodríguez-Fernández, J. (2008) 'Effect of biodiesel fuels on diesel engine emissions', *Progress in Energy and Combustion Science*, 34(2), pp. 198–223. doi: 10.1016/j.pecs.2007.07.001.

Le, K. C. *et al.* (2019) 'Direct observation of aliphatic structures in soot particles produced in low-pressure premixed ethylene flames via online Raman spectroscopy', *Proceedings of the Combustion Institute*. doi: 10.1016/j.proci.2018.08.003.

Lee, S. H. *et al.* (2008) 'Reversible lithium-ion insertion in molybdenum oxide nanoparticles', *Advanced Materials*. doi: 10.1002/adma.200800999.

Lee, S. W. and Glavincevski, B. (1999) 'NMR method for determination of aromatics in middle distillate oils', *Fuel Processing Technology*, 60(1), pp. 81–86. doi: 10.1016/S0378-3820(99)00013-2.

Lespade, P. *et al.* (1984) 'Caracterisation de matériaux carbonés par microspectrométrie Raman', *Carbon*. doi: 10.1016/0008-6223(84)90009-5.

- Li, C., Adamcik, J. and Mezzenga, R. (2012) 'Biodegradable nanocomposites of amyloid fibrils and graphene with shape-memory and enzyme-sensing properties', *Nature Nanotechnology*. Nature Publishing Group, 7(7), pp. 421–427. doi: 10.1038/nnano.2012.62.
- Li, S. *et al.* (2016) 'Flame aerosol synthesis of nanostructured materials and functional devices: Processing, modeling, and diagnostics', *Progress in Energy and Combustion Science*. doi: 10.1016/j.pecs.2016.04.002.
- Linak, W. P., Miller, C. A. and Wendt, J. O. L. (2000) 'Comparison of particle size distributions and elemental partitioning from the combustion of pulverized coal and residual fuel oil', *Journal of the Air and Waste Management Association*, 50(8), pp. 1532–1544. doi: 10.1080/10473289.2000.10464171.
- Liu, C. *et al.* (2019) 'Flame-formed carbon nanoparticles exhibit quantum dot behaviors', *Proceedings of the National Academy of Sciences of the United States of America*, 116(26), pp. 12692–12697. doi: 10.1073/pnas.1900205116.
- Liu, H., Ye, T. and Mao, C. (2007) 'Fluorescent carbon nanoparticles derived from candle soot', *Angewandte Chemie - International Edition*. doi: 10.1002/anie.200701271.
- Liu, T. C. and Li, Y. Y. (2006) 'Synthesis of carbon nanocapsules and carbon nanotubes by an acetylene flame method', *Carbon*. doi: 10.1016/j.carbon.2006.01.032.
- Liu, Y. *et al.* (1996) 'Preparation of nano-sized amorphous molybdenum dioxide powders by use of  $\gamma$ -ray radiation method', *Materials Research Bulletin*. doi: 10.1016/S0025-5408(96)00082-7.
- Liu, Y. *et al.* (2014) 'One-step microwave-assisted polyol synthesis of green luminescent carbon dots as optical nanoprobe', *Carbon*. doi: 10.1016/j.carbon.2013.10.086.
- Lu, M. and Mulholland, J. A. (2001) 'Aromatic hydrocarbon growth from indene', *Chemosphere*. doi: 10.1016/S0045-6535(00)00236-8.
- M. Anpo, M. Kondo, Y. Kubokawa, C. Louis, M. C. (1988) 'Dynamic studies of the photoinduced metathesis of C<sub>3</sub>H<sub>6</sub> and photoreduction of Mo with CO on anchored and impregnated Mo/SiO<sub>2</sub> catalyst', *J. Chem. Soc. Faraday Trans.*
- Mädler, L. *et al.* (2002) 'Controlled synthesis of nanostructured particles by flame spray pyrolysis', *Journal of Aerosol Science*. doi: 10.1016/S0021-8502(01)00159-8.
- Mahmoudi, T., Wang, Y. and Hahn, Y. B. (2018) 'Graphene and its derivatives for solar cells application', *Nano Energy*. doi: 10.1016/j.nanoen.2018.02.047.
- Manoj, B. *et al.* (2012) 'Characterization of diesel soot from the combustion in engine by X-ray and spectroscopic techniques', *International Journal of Electrochemical Science*, 7(4), pp. 3215–3221.
- Mao, Q., van Duin, A. C. T. and Luo, K. H. (2017) 'Formation of incipient soot particles from polycyclic aromatic hydrocarbons: A ReaxFF molecular dynamics study', *Carbon*. doi: 10.1016/j.carbon.2017.06.009.
- Maricq, M. M. (2004) 'Size and charge of soot particles in rich premixed ethylene flames',



*Combustion and Flame*. doi: 10.1016/j.combustflame.2004.01.013.

Martin, J. W. *et al.* (2019a) 'Reactivity of polycyclic aromatic hydrocarbon radicals : implications for soot formation', *Journal of Physical Chemistry C*, (234). doi: 10.1021/acs.jpcc.9b07558.

Martin, J. W. *et al.* (2019b) 'Reactivity of Polycyclic Aromatic Hydrocarbon Soot Precursors: Implications of Localized Radicals on Rim-Based Pentagonal Rings', *Journal of Physical Chemistry C*. doi: 10.1021/acs.jpcc.9b07558.

Martin, P. M. *et al.* (2000) 'Piezoelectric films for 100-MHz ultrasonic transducers', *Thin Solid Films*, 379(1–2), pp. 253–258. doi: 10.1016/S0040-6090(00)01339-0.

Maser, W. K. *et al.* (1998) 'Production of high-density single-walled nanotube material by a simple laser-ablation method', *Chemical Physics Letters*. doi: 10.1016/S0009-2614(98)00776-3.

Matsugi, A. and Miyoshi, A. (2012) 'Computational study on the recombination reaction between benzyl and propargyl radicals', *International Journal of Chemical Kinetics*. doi: 10.1002/kin.20625.

Mattevi, C., Kim, H. and Chhowalla, M. (2011) 'A review of chemical vapour deposition of graphene on copper', *Journal of Materials Chemistry*. doi: 10.1039/c0jm02126a.

McEnally, C. S. and Pfefferle, L. D. (1998) 'Soot formation in methane/air nonpremixed flames doped with small quantities of C<sub>3</sub> hydrocarbons', *Combustion and Flame*, 112(4), pp. 545–558. doi: 10.1016/S0010-2180(97)00144-2.

McEnally, C. S. and Pfefferle, L. D. (2007) 'The effects of dimethyl ether and ethanol on benzene and soot formation in ethylene nonpremixed flames', *Proceedings of the Combustion Institute*, 31 I(1), pp. 603–610. doi: 10.1016/j.proci.2006.07.005.

Memon, N. K. *et al.* (2011) 'Flame synthesis of graphene films in open environments', *Carbon*. doi: 10.1016/j.carbon.2011.07.024.

Menon, A. *et al.* (2019) 'Optical band gap of cross-linked, curved, and radical polyaromatic hydrocarbons', *Physical Chemistry Chemical Physics*. doi: 10.1039/c9cp02363a.

Merchan-Merchan, W. *et al.* (2010) 'Combustion synthesis of carbon nanotubes and related nanostructures', *Progress in Energy and Combustion Science*. doi: 10.1016/j.pecs.2010.02.005.

Mercier, X. *et al.* (2019) 'Dimers of polycyclic aromatic hydrocarbons: The missing pieces in the soot formation process', *Physical Chemistry Chemical Physics*. Royal Society of Chemistry, 21(16), pp. 8285–8294. doi: 10.1039/c9cp00394k.

Messerer, A., Niessner, R. and Pöschl, U. (2006) 'Comprehensive kinetic characterization of the oxidation and gasification of model and real diesel soot by nitrogen oxides and oxygen under engine exhaust conditions: Measurement, Langmuir-Hinshelwood, and Arrhenius parameters', *Carbon*. doi: 10.1016/j.carbon.2005.07.017.

Meyyappan, M. (2009) 'A review of plasma enhanced chemical vapour deposition of

carbon nanotubes', *Journal of Physics D: Applied Physics*, 42(21), p. 213001. doi: 10.1088/0022-3727/42/21/213001.

Miller, J. A. and Melius, C. F. (1992) 'Kinetic and thermodynamic issues in the formation of aromatic compounds in flames of aliphatic fuels', *Combustion and Flame*. doi: 10.1016/0010-2180(92)90124-8.

Miller, J. H. (1991) 'The kinetics of polynuclear aromatic hydrocarbon agglomeration in flames', *Symposium (International) on Combustion*. doi: 10.1016/S0082-0784(06)80246-8.

Minutolo, P. *et al.* (2008) 'Emission of ultrafine particles from natural gas domestic burners', in *Environmental Engineering Science*. doi: 10.1089/ees.2007.0188.

Minutolo, P. *et al.* (2011) 'Surface enhanced Raman spectroscopy (SERS) of particles produced in premixed flame across soot threshold', *Proceedings of the Combustion Institute*. doi: 10.1016/j.proci.2010.07.077.

Minutolo, P. *et al.* (2014) 'Characterization of flame-generated 2-D carbon nano-disks', *Carbon*. Elsevier Ltd, 68, pp. 138–148. doi: 10.1016/j.carbon.2013.10.073.

Minutolo, P., Gambi, G. and D'Alessio, A. (1996) 'The optical band gap model in the interpretation of the UV-visible absorption spectra of rich premixed flames', *Symposium (International) on Combustion*. doi: 10.1016/S0082-0784(96)80307-9.

Monajjemi, M. (2017) 'Liquid-phase exfoliation (LPE) of graphite towards graphene: An ab initio study', *Journal of Molecular Liquids*. doi: 10.1016/j.molliq.2017.01.044.

Montellano López, A., Mateo-Alonso, A. and Prato, M. (2011) 'Materials chemistry of fullerene C60 derivatives', *Journal of Materials Chemistry*, 21(5), pp. 1305–1318. doi: 10.1039/c0jm02386h.

Mou, Z. *et al.* (2014) 'Evidence of  $\sigma$ - And  $\pi$ -dimerization in a series of Phenalenyls', *Journal of the American Chemical Society*, 136(52), pp. 18009–18022. doi: 10.1021/ja509243p.

Mulay, M. R. *et al.* (2019) 'Candle soot: Journey from a pollutant to a functional material', *Carbon*. doi: 10.1016/j.carbon.2018.12.083.

Mulliken, R. S. (1955) 'Electronic population analysis on LCAO-MO molecular wave functions. I', *The Journal of Chemical Physics*. doi: 10.1063/1.1740588.

Murayama, H. *et al.* (2004) 'Fullerene production in tons and more: From science to industry', *Fullerenes Nanotubes and Carbon Nanostructures*. doi: 10.1081/FST-120027125.

Nakada, K. *et al.* (1996) 'Edge state in graphene ribbons: Nanometer size effect and edge shape dependence', *Physical Review B - Condensed Matter and Materials Physics*. doi: 10.1103/PhysRevB.54.17954.

Nanot, S. *et al.* (2013) 'Single-walled carbon nanotubes', in *Springer Handbook of Nanomaterials*. doi: 10.1007/978-3-642-20595-8\_4.

*Nanotechnologies — Vocabulary — Part I: Core terms* (2015).

- Narayan, R. J., Boehm, R. D. and Sumant, A. V. (2011) 'Medical applications of diamond particles & surfaces', *Materials Today*. doi: 10.1016/S1369-7021(11)70087-6.
- Neese, F. (2018) 'Software update: the ORCA program system, version 4.0', *Wiley Interdisciplinary Reviews: Computational Molecular Science*. doi: 10.1002/wcms.1327.
- Nekoueiian, K. *et al.* (2019) 'Carbon-based quantum particles: An electroanalytical and biomedical perspective', *Chemical Society Reviews*, 48(15), pp. 4281–4316. doi: 10.1039/c8cs00445e.
- Nouailhat, A. (2010) *An introduction to nanoscience and nanotechnology, An Introduction to Nanoscience and Nanotechnology*. doi: 10.1002/9780470610954.
- Novoselov, K. S. *et al.* (2005) 'Two-dimensional gas of massless Dirac fermions in graphene', *Nature*. doi: 10.1038/nature04233.
- O'Regan, B. and Grätzel, M. (1991) 'A low-cost, high-efficiency solar cell based on dye-sensitized colloidal TiO<sub>2</sub> films', *Nature*. doi: 10.1038/353737a0.
- Oberdörster, G. *et al.* (2004) 'Translocation of inhaled ultrafine particles to the brain', in *Inhalation Toxicology*. doi: 10.1080/08958370490439597.
- Oberdörster, G., Oberdörster, E. and Oberdörster, J. (2005) 'Nanotoxicology: An emerging discipline evolving from studies of ultrafine particles', *Environmental Health Perspectives*, 113(7), pp. 823–839. doi: 10.1289/ehp.7339.
- P. Pritchard, B. *et al.* (2019) 'New Basis Set Exchange: An Open, Up-to-Date Resource for the Molecular Sciences Community', *Journal of Chemical Information and Modeling*. American Chemical Society, 59(11), pp. 4814–4820. doi: 10.1021/acs.jcim.9b00725.
- Pal, B. and Sharon, M. (2002) 'Enhanced photocatalytic activity of highly porous ZnO thin films prepared by sol-gel process', *Materials Chemistry and Physics*, 76(1), pp. 82–87. doi: 10.1016/S0254-0584(01)00514-4.
- Pan, D., Wang, Q. and An, L. (2009) 'Controlled synthesis of monodisperse nanocrystals by a two-phase approach without the separation of nucleation and growth processes', *Journal of Materials Chemistry*, 19(8), pp. 1063–1073. doi: 10.1039/b810972a.
- Pang, X. *et al.* (2008) 'Carbonyls emission from ethanol-blended gasoline and biodiesel-ethanol-diesel used in engines', *Atmospheric Environment*, 42(6), pp. 1349–1358. doi: 10.1016/j.atmosenv.2007.10.075.
- Pardanaud, C. *et al.* (2013) 'Raman spectroscopy investigation of the H content of heated hard amorphous carbon layers', *Diamond and Related Materials*. doi: 10.1016/j.diamond.2013.02.009.
- Paulo, S. *et al.* (2016) 'Carbon quantum dots as new hole transport material for perovskite solar cells', *Synthetic Metals*, 222, pp. 17–22. doi: 10.1016/j.synthmet.2016.04.025.
- Pedata, P. *et al.* (2015) "'Are we forgetting the smallest, sub 10 nm combustion generated particles?'"', *Particle and Fibre Toxicology*. doi: 10.1186/s12989-015-0107-3.
- Philippe, R. *et al.* (2007) 'Catalytic production of carbon nanotubes by fluidized-bed CVD', *Chemical Vapor Deposition*. doi: 10.1002/cvde.200600036.

- Pilawa, B. *et al.* (2005) 'Multi-component EPR spectra of coals with different carbon content', *Acta Physica Polonica A*. doi: 10.12693/APhysPolA.108.403.
- Piperel, A., Dagaut, P. and Montagne, X. (2009) 'Impact of acetaldehyde and NO addition on the 1-octene oxidation under simulated HCCI conditions', *Proceedings of the Combustion Institute*. The Combustion Institute, 32 II(2), pp. 2861–2868. doi: 10.1016/j.proci.2008.08.004.
- Pokropivny, V. V. and Skorokhod, V. V. (2007) 'Classification of nanostructures by dimensionality and concept of surface forms engineering in nanomaterial science', *Materials Science and Engineering C*. Elsevier B.V., 27(5-8 SPEC. ISS.), pp. 990–993. doi: 10.1016/j.msec.2006.09.023.
- Polizu, S. *et al.* (2006) 'Applications of carbon nanotubes-based biomaterials in biomedical nanotechnology', *Journal of Nanoscience and Nanotechnology*. doi: 10.1166/jnn.2006.197.
- Popov, V. N. and Lambin, P. (2013) 'Theoretical 2D Raman band of strained graphene', *Physical Review B - Condensed Matter and Materials Physics*. doi: 10.1103/PhysRevB.87.155425.
- Prasad, P. V. and Storey, P. (2008) 'Magnetic resonance imaging', in *Molecular Biomethods Handbook: Second Edition*. doi: 10.1007/978-1-60327-375-6\_53.
- Pratsinis, S. E. (1998) 'Flame aerosol synthesis of ceramic powders', *Progress in Energy and Combustion Science*. doi: 10.1016/S0360-1285(97)00028-2.
- Pratsinis, S. E. and Mastrangelo, V. R. (1989) 'Material synthesis in aerosol reactors', *Chemical Engineering Progress*.
- Prikhod'ko, N. G. *et al.* (2015) 'Flame synthesis of graphene layers at low pressure', *Russian Journal of Physical Chemistry B*, 9(5), pp. 743–747. doi: 10.1134/S1990793115050115.
- Prikhod'Ko, N. G. *et al.* (2014) 'Synthesis of graphene films in a flame', *Russian Journal of Physical Chemistry B*, 8(1), pp. 61–64. doi: 10.1134/S1990793114010059.
- 'Proceedings of the Chemical Society. April 1961' (1961) *Proceedings of the Chemical Society*. The Royal Society of Chemistry, (April), pp. 129–152. doi: 10.1039/PS9610000129.
- Pugmire, R. J. *et al.* (no date) 'Soot Formation Process', in.
- Qiao, Z. A. *et al.* (2010) 'Commercially activated carbon as the source for producing multicolor photoluminescent carbon dots by chemical oxidation', *Chemical Communications*. doi: 10.1039/c0cc02724c.
- Question about Nanotechnology* (2012).
- Radovic, L. R. and Bockrath, B. (2005) 'On the chemical nature of graphene edges: Origin of stability and potential for magnetism in carbon materials', *Journal of the American Chemical Society*. doi: 10.1021/ja050124h.
- Raman, C. V. and Krishnan, K. S. (1928) 'A new type of secondary radiation [11]',

*Nature*. doi: 10.1038/121501c0.

Rankin, N. J. *et al.* (2014) 'The emergence of proton nuclear magnetic resonance metabolomics in the cardiovascular arena as viewed from a clinical perspective', *Atherosclerosis*. Elsevier Ltd, 237(1), pp. 287–300. doi: 10.1016/j.atherosclerosis.2014.09.024.

Requejo, A. G. *et al.* (1992) 'Maturation of petroleum source rocks. 1. Changes in kerogen structure and composition associated with hydrocarbon generation', *Energy and Fuels*. doi: 10.1021/ef00032a015.

Rhodes, C. J. (2011) *Electron spin resonance. part two: A diagnostic method in the environmental sciences*, *Science Progress*. doi: 10.3184/003685011X13130481780217.

Richter, H. *et al.* (2005) 'Detailed modeling of PAH and soot formation in a laminar premixed benzene/oxygen/argon low-pressure flame', *Proceedings of the Combustion Institute*. doi: 10.1016/j.proci.2004.08.088.

Richter, H. *et al.* (2008) 'Large scale combustion synthesis of single-walled carbon nanotubes and their characterization', *Journal of Nanoscience and Nanotechnology*. doi: 10.1166/jnn.2008.SW07.

Richter, H. and Howard, J. B. (2000) 'Formation of polycyclic aromatic hydrocarbons and their growth to soot-a review of chemical reaction pathways', *Progress in Energy and Combustion Science*. doi: 10.1016/S0360-1285(00)00009-5.

Rogers, F. *et al.* (2005) 'Real-time measurements of jet aircraft engine exhaust', *Journal of the Air and Waste Management Association*, 55(5), pp. 583–593. doi: 10.1080/10473289.2005.10464651.

Rosner, D. E. (2005) 'Flame synthesis of valuable nanoparticles: Recent progress/current needs in areas of rate laws, population dynamics, and characterization', *Industrial and Engineering Chemistry Research*, 44(16), pp. 6045–6055. doi: 10.1021/ie0492092.

Rossi, M. J. (2008) 'Thermochemical properties from ab Initio calculations:  $\pi$  and  $\sigma$ -free radicals of importance in soot formation:  $\cdot\text{C}_3\text{H}_3$  (propargyl),  $\cdot\text{C}_4\text{H}_3$ ,  $\cdot\text{C}_{13}\text{H}_9$  (phenalenyl),  $\cdot\text{C}_6\text{H}_5$  (phenyl),  $\cdot\text{C}_{10}\text{H}_7$  (naphthyl),  $\cdot\text{C}_{14}\text{H}_{\dots}$ ', *International Journal of Chemical Kinetics*. doi: 10.1002/kin.20326.

Roth, P. (2007) 'Particle synthesis in flames', *Proceedings of the Combustion Institute*. doi: 10.1016/j.proci.2006.08.118.

Rüchardt, C. and Beckhaus, H.-D. (1980) 'Towards an Understanding of the Carbon-Carbon Bond', 19, pp. 429–440.

Rudrapati, R. (2020) 'Graphene: Fabrication Methods, Properties, and Applications in Modern Industries', in *Graphene Production and Application*. doi: 10.5772/intechopen.92258.

Sadat-Shojai, M. *et al.* (2010) 'Hydroxyapatite nanorods as novel fillers for improving the properties of dental adhesives: Synthesis and application', *Dental Materials*. The Academy of Dental Materials, 26(5), pp. 471–482. doi: 10.1016/j.dental.2010.01.005.

- Sadezky, A. *et al.* (2005) 'Raman microspectroscopy of soot and related carbonaceous materials: Spectral analysis and structural information', *Carbon*. doi: 10.1016/j.carbon.2005.02.018.
- Saito, K. *et al.* (1991) 'A Study of the Early History of Soot Formation in Various Hydrocarbon Diffusion Flames', *Combustion Science and Technology*. doi: 10.1080/00102209108951779.
- Salamanca, M. *et al.* (2012a) 'Variations of the soot precursors chemical composition induced by ethanol addition to fuel', in *Energy and Fuels*. doi: 10.1021/ef300926y.
- Salamanca, M. *et al.* (2012b) 'Variations of the soot precursors chemical composition induced by ethanol addition to fuel', *Energy and Fuels*, 26(11), pp. 6602–6611. doi: 10.1021/ef300926y.
- Santamaria, A. *et al.* (2010) 'Chemical and morphological characterization of soot and soot precursors generated in an inverse diffusion flame with aromatic and aliphatic fuels', *Combustion and Flame*. The Combustion Institute., 157(1), pp. 33–42. doi: 10.1016/j.combustflame.2009.09.016.
- Santamaria, A. *et al.* (2006) 'FT-IR and <sup>1</sup>H NMR characterization of the products of an ethylene inverse diffusion flame', *Combustion and Flame*, 146(1–2), pp. 52–62. doi: 10.1016/j.combustflame.2006.04.008.
- Santamaria, A. *et al.* (2007) 'Average structural analysis of the extractable material of young soot gathered in an ethylene inverse diffusion flame', *Fuel*, 86(12–13), pp. 1908–1917. doi: 10.1016/j.fuel.2006.12.002.
- Santamaria, A., Eddings, E. G. and Mondragón, F. (2007) 'Effect of ethanol on the chemical structure of the soot extractable material of an ethylene inverse diffusion flame', *Combustion and Flame*, 151(1–2), pp. 235–244. doi: 10.1016/j.combustflame.2007.06.004.
- Sattler, K. (1995) 'Scanning tunneling microscopy of carbon nanotubes and nanocones', *Carbon*. doi: 10.1016/0008-6223(95)00020-E.
- Savy, D. *et al.* (2017) 'Molecular Characterization of Extracts from Biorefinery Wastes and Evaluation of Their Plant Biostimulation', *ACS Sustainable Chemistry and Engineering*, 5(10), pp. 9023–9031. doi: 10.1021/acssuschemeng.7b01928.
- Sawabe, A. and Inuzuka, T. (1985) 'Growth of diamond thin films by electron assisted chemical vapor deposition', *Applied Physics Letters*. doi: 10.1063/1.95715.
- Schubert, D. *et al.* (2006) 'Cerium and yttrium oxide nanoparticles are neuroprotective', *Biochemical and Biophysical Research Communications*, 342(1), pp. 86–91. doi: 10.1016/j.bbrc.2006.01.129.
- Schuetz, C. A. and Frenklach, M. (2002) 'Nucleation of soot: Molecular dynamics simulations of pyrene dimerization', *Proceedings of the Combustion Institute*. doi: 10.1016/s1540-7489(02)80281-4.
- Schulz, F. *et al.* (2019) 'Insights into incipient soot formation by atomic force microscopy', *Proceedings of the Combustion Institute*. Elsevier Inc., 37(1), pp. 885–892.

doi: 10.1016/j.proci.2018.06.100.

Seipenbusch, M. *et al.* (2005) 'Catalytic soot oxidation in microscale experiments', *Applied Catalysis B: Environmental*. doi: 10.1016/j.apcatb.2004.07.007.

Semenikhin, A. S. *et al.* (2020) 'On the mechanism of soot nucleation. II. E-bridge formation at the PAH bay', *Physical Chemistry Chemical Physics*. Royal Society of Chemistry, 22(30), pp. 17196–17204. doi: 10.1039/d0cp02554b.

Seong, H. J. and Boehman, A. L. (2013) 'Evaluation of Raman parameters using visible Raman microscopy for soot oxidative reactivity', *Energy and Fuels*. doi: 10.1021/ef301520y.

Sgro, L. A. *et al.* (2007) 'Characterization of nanoparticles of organic carbon (NOC) produced in rich premixed flames by differential mobility analysis', *Proceedings of the Combustion Institute*. doi: 10.1016/j.proci.2006.08.026.

Sgro, L. A. *et al.* (2009) 'Measurement of nanoparticles of organic carbon in non-sooting flame conditions', *Proceedings of the Combustion Institute*. doi: 10.1016/j.proci.2008.06.216.

Shanbogh, P. P. and Sundaram, N. G. (2015) 'Fullerenes revisited', *Resonance*. doi: 10.1007/s12045-015-0160-0.

Sharma, V. K. *et al.* (2015) 'Natural inorganic nanoparticles-formation, fate, and toxicity in the environment', *Chemical Society Reviews*. Royal Society of Chemistry, 44(23), pp. 8410–8423. doi: 10.1039/c5cs00236b.

Shin, S. R. *et al.* (2016) 'Graphene-based materials for tissue engineering', *Advanced Drug Delivery Reviews*. doi: 10.1016/j.addr.2016.03.007.

Shmakov, A. G. *et al.* (2010) 'Formation and consumption of NO in H<sub>2</sub> + O<sub>2</sub> + N<sub>2</sub> flames doped with NO or NH<sub>3</sub> at atmospheric pressure', *Energy and Fuels*. Royal Society of Chemistry, 24(6), pp. 1143–1164. doi: 10.1039/c7cp08518d.

Sholl, D. S. and Steckel, J. A. (2009) *Density Functional Theory: A Practical Introduction*, *Density Functional Theory: A Practical Introduction*. doi: 10.1002/9780470447710.

Simmie, J. M. (2003) 'Detailed chemical kinetic models for the combustion of hydrocarbon fuels', *Progress in Energy and Combustion Science*, 29(6), pp. 599–634. doi: 10.1016/S0360-1285(03)00060-1.

Sinclair, R. C., Suter, J. L. and Coveney, P. V. (2019) 'Micromechanical exfoliation of graphene on the atomistic scale', *Physical Chemistry Chemical Physics*. doi: 10.1039/c8cp07796g.

Singer, L. S. *et al.* (1987) 'EPR characteristics of separated fractions of mesophase pitches', *Journal of Physical Chemistry*. doi: 10.1021/j100293a041.

Singh, S. K. and Chauhan, R. (2014) 'Study of Optical Properties of Transition Metal Oxides on the Basis of Energy Band and Energy State Analysis', *The International Journal Of Engineering And Science (IJES)*, 3(6), pp. 37–40.

- Sirignano, M. *et al.* (2012) 'Detection of aromatic hydrocarbons and incipient particles in an opposed-flow flame of ethylene by spectral and time-resolved laser induced emission spectroscopy', *Combustion and Flame*. doi: 10.1016/j.combustflame.2011.11.005.
- Sirignano, M., Kent, J. and D'Anna, A. (2010) 'Detailed modeling of size distribution functions and hydrogen content in combustion-formed particles', *Combustion and Flame*. doi: 10.1016/j.combustflame.2009.11.014.
- Small, D. *et al.* (2005) 'Characterizing the dimerizations of phenalenyl radicals by ab initio calculations and spectroscopy:  $\sigma$ -Bond formation versus resonance  $\pi$ -stabilization', *Journal of Physical Chemistry A*, 109(49), pp. 11261–11267. doi: 10.1021/jp054244n.
- Smoluchowski, M. (1916) 'Drei Vorträge über Diffusion, Brownsche Bewegung und Koagulation von Kolloidteilchen', *Z. Phys.*
- Sogo, P. B., Nakazaki, M. and Calvin, M. (1957) 'Free radical from perinaphthene', *The Journal of Chemical Physics*. doi: 10.1063/1.1743526.
- Solum, M. S. *et al.* (2001) ' $^{13}\text{C}$  NMR analysis of soot produced from model compounds and a coal', *Energy and Fuels*, 15(4), pp. 961–971. doi: 10.1021/ef0100294.
- Song, K. H. *et al.* (2003) 'Effects of oxygenated additives on aromatic species in fuel-rich, premixed ethane combustion: A modeling study', *Combustion and Flame*, 135(3), pp. 341–349. doi: 10.1016/S0010-2180(03)00180-9.
- Spitsyn, B. V., Bouilov, L. L. and Derjaguin, B. V. (1981) 'Vapor growth of diamond on diamond and other surfaces', *Journal of Crystal Growth*. doi: 10.1016/0022-0248(81)90197-4.
- Stauber, T., Guinea, F. and Vozmediano, M. A. H. (2005) 'Disorder and interaction effects in two-dimensional graphene sheets', *Physical Review B - Condensed Matter and Materials Physics*. doi: 10.1103/PhysRevB.71.041406.
- Stein, S. E. and Fahr, A. (1985) 'High-temperature stabilities of hydrocarbons', *Journal of Physical Chemistry*. doi: 10.1021/j100263a027.
- Strobel, R. and Pratsinis, S. E. (2007) 'Flame aerosol synthesis of smart nanostructured materials', *Journal of Materials Chemistry*. doi: 10.1039/b711652g.
- Subramoney, S. (1998) 'Novel nanocarbons - Structure, properties, and potential applications', *Advanced Materials*. doi: 10.1002/(SICI)1521-4095(199810)10:15<1157::AID-ADMA1157>3.0.CO;2-N.
- Sun, Y. P. *et al.* (2006) 'Quantum-sized carbon dots for bright and colorful photoluminescence', *Journal of the American Chemical Society*, 128(24), pp. 7756–7757. doi: 10.1021/ja062677d.
- Takehara, H. *et al.* (2005) 'Experimental study of industrial scale fullerene production by combustion synthesis', *Carbon*, 43(2), pp. 311–319. doi: 10.1016/j.carbon.2004.09.017.
- Tang, J. *et al.* (2013) 'Carbon nanodots featuring efficient FRET for real-time monitoring of drug delivery and two-photon imaging', *Advanced Materials*, 25(45), pp. 6569–6574. doi: 10.1002/adma.201303124.



- Tang, W., S. Tranter, R. and Brezinsky, K. (2006) 'An Optimized Semidetailed Submechanism of Benzene Formation from Propargyl Recombination', *The Journal of Physical Chemistry A*, 110(6), pp. 2165–2175. doi: 10.1021/jp052797s.
- Tani, T., Mädler, L. and Pratsinis, S. E. (2002) 'Homogeneous ZnO nanoparticles by flame spray pyrolysis', *Journal of Nanoparticle Research*. doi: 10.1023/A:1021153419671.
- Tarasenka, N. *et al.* (2017) 'Structure and Optical Properties of Carbon Nanoparticles Generated by Laser Treatment of Graphite in Liquids', *ChemPhysChem*. doi: 10.1002/cphc.201601182.
- Taylor, D. A. (2002) 'Dust in the wind', *Environmental Health*, 110(2), pp. 80–87.
- Thompson, B. C. and Fréchet, J. M. J. (2008) 'Polymer-fullerene composite solar cells', *Angewandte Chemie - International Edition*. doi: 10.1002/anie.200702506.
- Tian, Z. R. *et al.* (2003) 'Complex and oriented ZnO nanostructures', *Nature Materials*, 2(12), pp. 821–826. doi: 10.1038/nmat1014.
- Tite, T. *et al.* (2014) 'Graphene-based textured surface by pulsed laser deposition as a robust platform for surface enhanced Raman scattering applications', *Applied Physics Letters*. doi: 10.1063/1.4863824.
- Tiwari, J. N., Tiwari, R. N. and Kim, K. S. (2012) 'Zero-dimensional, one-dimensional, two-dimensional and three-dimensional nanostructured materials for advanced electrochemical energy devices', *Progress in Materials Science*. Elsevier Ltd, 57(4), pp. 724–803. doi: 10.1016/j.pmatsci.2011.08.003.
- Totton, T. S., Misquitta, A. J. and Kraft, M. (2011) 'A transferable electrostatic model for intermolecular interactions between polycyclic aromatic hydrocarbons', *Chemical Physics Letters*. doi: 10.1016/j.cplett.2011.05.021.
- Totton, T. S., Misquitta, A. J. and Kraft, M. (2012) 'A quantitative study of the clustering of polycyclic aromatic hydrocarbons at high temperatures', *Physical Chemistry Chemical Physics*. doi: 10.1039/c2cp23008a.
- Tregrossi, A., Ciajolo, A. and Barbella, R. (1999) 'The combustion of benzene in rich premixed flames at atmospheric pressure', *Combustion and Flame*. doi: 10.1016/S0010-2180(98)00157-6.
- Valavanidis, A. *et al.* (2008) 'Persistent free radicals, heavy metals and PAHs generated in particulate soot emissions and residue ash from controlled combustion of common types of plastic', *Journal of Hazardous Materials*. doi: 10.1016/j.jhazmat.2007.12.019.
- Violi, A. (2004) 'Modeling of soot particle inception in aromatic and aliphatic premixed flames', *Combustion and Flame*. doi: 10.1016/j.combustflame.2004.08.013.
- Violi, A., Sarofim, A. F. and Truong, T. N. (2001) 'Quantum mechanical study of molecular weight growth process by combination of aromatic molecules', *Combustion and Flame*. doi: 10.1016/S0010-2180(01)00268-1.
- Vitiello, Giuseppe *et al.* (2019) 'Role of radicals in carbon clustering and soot inception:

- A combined EPR and Raman spectroscopic study', *Combustion and Flame*, 205, pp. 286–294. doi: <https://doi.org/10.1016/j.combustflame.2019.04.028>.
- Vitiello, G. *et al.* (2019) 'Role of radicals in carbon clustering and soot inception: A combined EPR and Raman spectroscopic study', *Combustion and Flame*, 205. doi: 10.1016/j.combustflame.2019.04.028.
- De Volder, M. F. L. *et al.* (2013) 'Carbon nanotubes: Present and future commercial applications', *Science*, 339(6119), pp. 535–539. doi: 10.1126/science.1222453.
- Wagner, H. G. G. (1979) 'Soot formation in combustion', *Symposium (International) on Combustion*, 17(1), pp. 3–19. doi: [https://doi.org/10.1016/S0082-0784\(79\)80005-3](https://doi.org/10.1016/S0082-0784(79)80005-3).
- Vander Wal, R. L. (2002) 'Fe-catalyzed single-walled carbon nanotube synthesis within a flame environment', *Combustion and Flame*. doi: 10.1016/S0010-2180(02)00360-7.
- Vander Wal, R. L. and Tomasek, A. J. (2003) 'Soot oxidation: Dependence upon initial nanostructure', *Combustion and Flame*. doi: 10.1016/S0010-2180(03)00084-1.
- Wang, H. (2011) 'Formation of nascent soot and other condensed-phase materials in flames', *Proceedings of the Combustion Institute*. doi: 10.1016/j.proci.2010.09.009.
- Wang, H. *et al.* (2016) 'Nitrogen-doped carbon dots for “green” quantum dot solar cells', *Nanoscale Research Letters*. *Nanoscale Research Letters*, 11(1), pp. 1–6. doi: 10.1186/s11671-016-1231-1.
- Wang, T. *et al.* (2009) 'EPR and DFT study of the polycyclic aromatic radical cations from friedel-crafts alkylation reactions', *Chinese Journal of Chemical Physics*, 22(1), pp. 51–56. doi: 10.1088/1674-0068/22/01/51-56.
- Wang, Y. *et al.* (2018) 'Revised M06 density functional for main-group and transition-metal chemistry', *Proceedings of the National Academy of Sciences of the United States of America*. doi: 10.1073/pnas.1810421115.
- Weir, A. *et al.* (2012) 'Titanium dioxide nanoparticles in food and personal care products', *Environmental Science and Technology*, 46(4), pp. 2242–2250. doi: 10.1021/es204168d.
- Whitesides, R. *et al.* (2009) 'Embedded-ring migration on graphene zigzag edge', *Proceedings of the Combustion Institute*. doi: 10.1016/j.proci.2008.06.096.
- Whitesides, R. and Frenklach, M. (2010) 'Detailed kinetic monte carlo simulations of graphene-edge growth', *Journal of Physical Chemistry A*. doi: 10.1021/jp906541a.
- Wiedemeier, D. B. *et al.* (2015) 'Aromaticity and degree of aromatic condensation of char', *Organic Geochemistry*. Elsevier Ltd, 78, pp. 135–143. doi: 10.1016/j.orggeochem.2014.10.002.
- Wooldridge, M. S. (1998) 'Gas-phase combustion synthesis of particles', *Progress in Energy and Combustion Science*. doi: 10.1016/S0360-1285(97)00024-5.
- Xavier Marguerettaz and Donald Fitzmaurice (1994) 'Heterosupramolecular chemistry: long-lived charge trapping by vectorial electron flow in a heterotriad', *J. Am. Chem. Soc.*, 116(11), pp. 5017–5018.

- Xu, J. *et al.* (2000) 'Grain size control and gas sensing properties of ZnO gas sensor', *Sensors and Actuators, B: Chemical*. doi: 10.1016/S0925-4005(00)00381-6.
- Xu, X. *et al.* (2004) 'Electrophoretic analysis and purification of fluorescent single-walled carbon nanotube fragments', *Journal of the American Chemical Society*. doi: 10.1021/ja040082h.
- Y.Q. Huang, M.D. Liu, Y.K. Zeng, S. B. L. (2001) 'Progress of study on ZnO thin films and its properties', *J. Inorg. Mater*, 16(3), pp. 391–397.
- Bin Yang, H. *et al.* (2013) 'Graphene quantum dots-incorporated cathode buffer for improvement of inverted polymer solar cells', *Solar Energy Materials and Solar Cells*. Elsevier, 117, pp. 214–218. doi: 10.1016/j.solmat.2013.05.060.
- Yang, Y. *et al.* (1995) 'Reversible Fullerene Electrochemistry: Correlation with the HOMO-LUMO Energy Difference for C<sub>60</sub>, C<sub>70</sub>, C<sub>76</sub>, C<sub>78</sub>, and C<sub>84</sub>', *Journal of the American Chemical Society*. doi: 10.1021/ja00134a027.
- Yang, Y. *et al.* (2003) 'Study on relationship between the concentration of hydrocarbon groups in heavy oils and their structural parameter from <sup>1</sup>H NMR spectra', *Fuel*, 82(6), pp. 721–727. doi: 10.1016/S0016-2361(02)00353-8.
- Yazyev, O. V. and Louie, S. G. (2010) 'Electronic transport in polycrystalline graphene', *Nature Materials*. doi: 10.1038/nmat2830.
- Yi, G. C., Wang, C. and Park, W. Il (2005) 'ZnO nanorods: Synthesis, characterization and applications', *Semiconductor Science and Technology*. doi: 10.1088/0268-1242/20/4/003.
- Yogesh, G. K., Shuaib, E. P. and Sastikumar, D. (2017) 'Photoluminescence properties of carbon nanoparticles synthesized from activated carbon powder (4% ash) by laser ablation in solution', *Materials Research Bulletin*. doi: 10.1016/j.materresbull.2017.02.038.
- Yoo, E. and Zhou, H. (2011) 'Li-air rechargeable battery based on metal-free graphene nanosheet catalysts', *ACS Nano*. doi: 10.1021/nn200084u.
- Yordanov, N. D. and Lubenova, S. (2000) 'Effect of dielectric constants, sample container dimensions and frequency of magnetic field modulation on the quantitative EPR response', *Analytica Chimica Acta*. doi: 10.1016/S0003-2670(99)00638-8.
- Yordanov, N. D., Lubenova, S. and Sokolova, S. (2001) 'On the possibility for separate determination of pyrolyzed products (soot and polycyclic aromatic hydrocarbons) in aerosols by EPR spectrometry', *Atmospheric Environment*. doi: 10.1016/S1352-2310(00)00384-8.
- You, X. *et al.* (2011) 'Bay-capping reactions: Kinetics and influence on graphene-edge growth', *Proceedings of the Combustion Institute*. doi: 10.1016/j.proci.2010.05.110.
- Zemel, H. and Fessenden, R. W. (1975) 'Electron spin resonance studies of phenyl and pyridyl radicals in aqueous solution', *Journal of Physical Chemistry*, 79(14), pp. 1419–1427. doi: 10.1021/j100581a016.

- Zhai, X. *et al.* (2012) ‘Highly luminescent carbon nanodots by microwave-assisted pyrolysis’, *Chemical Communications*. doi: 10.1039/c2cc33869f.
- Zhang, J., Langille, M. R. and Mirkin, C. A. (2011) ‘Synthesis of silver nanorods by low energy excitation of spherical plasmonic seeds’, *Nano Letters*, 11(6), pp. 2495–2498. doi: 10.1021/nl2009789.
- Zhang, L. *et al.* (2012) ‘Synthesis of size-controlled monodisperse Pd nanoparticles via a non-aqueous seed-mediated growth’, *Nanoscale Research Letters*, 7(1), pp. 2–7. doi: 10.1186/1556-276X-7-312.
- Zhang, Y., Zhang, L. and Zhou, C. (2013) ‘Review of chemical vapor deposition of graphene and related applications’, *Accounts of Chemical Research*. doi: 10.1021/ar300203n.
- Zhao, B. *et al.* (2003) ‘Analysis of soot nanoparticles in a laminar premixed ethylene flame by scanning mobility particle sizer’, *Aerosol Science and Technology*, 37(8), pp. 611–620. doi: 10.1080/02786820300908.
- Zheng Wei Pan, Zu Rong Dai and Zhong Lin Wang (2001) ‘Nanobelts of semiconducting oxides’, *Science*, 291(5510), pp. 1947–1949. doi: 10.1126/science.1058120.
- Zhou, J. *et al.* (2003) ‘Synthesis of large-scaled MoO<sub>2</sub> nanowire arrays’, *Chemical Physics Letters*, 382(3–4), pp. 443–446. doi: 10.1016/j.cplett.2003.10.002.
- Zhou, J., Gong, L., *et al.* (2005) ‘Growth and field-emission property of tungsten oxide nanotip arrays’, *Applied Physics Letters*. doi: 10.1063/1.2136006.
- Zhou, J., Ding, Y., *et al.* (2005) ‘Three-dimensional tungsten oxide nanowire networks’, *Advanced Materials*. doi: 10.1002/adma.200500885.
- Zhu, S. *et al.* (2013) ‘Highly Photoluminescent Carbon Dots for Multicolor Patterning, Sensors, and Bioimaging’, *Angewandte Chemie*, 125(14), pp. 4045–4049. doi: 10.1002/ange.201300519.
- Zhu, S. *et al.* (2015) ‘The photoluminescence mechanism in carbon dots (graphene quantum dots, carbon nanodots, and polymer dots): current state and future perspective’, *Nano Research*, 8(2), pp. 355–381. doi: 10.1007/s12274-014-0644-3.

## APPENDIX: PUBLICATIONS

- 1) Picca, F., De Falco, G., Commodo, M., Vitiello, G., D'Errico, G., Minutolo, P., D'Anna, A. "Characteristics of flame-nucleated carbonaceous nanoparticles" (2019) *Chemical Engineering Transactions*, 73, pp. 61-66. DOI: 10.3303/CET1973011
- 2) Vitiello, G., De Falco, G., Picca, F., Commodo, M., D'Errico, G., Minutolo, P., D'Anna, A. "Role of radicals in carbon clustering and soot inception: A combined EPR and Raman spectroscopic study" (2019) *Combustion and Flame*, 205, pp. 286-294. DOI: 10.1016/j.combustflame.2019.04.028
- 3) Sabbah, H., Commodo, M., Picca, F., De Falco, G., Minutolo, P., D'Anna, A., Joblin, C. "Molecular content of nascent soot: Family characterization using two-step laser desorption laser ionization mass spectrometry" (2020) *Proceedings of the Combustion Institute*. DOI: 10.1016/j.proci.2020.09.022
- 4) Commodo, M., Picca, F., Vitiello, G., De Falco, G., Minutolo, P., D'Anna, A. "Radicals in nascent soot from laminar premixed ethylene and ethylene-benzene flames by electron paramagnetic resonance spectroscopy" (2020) *Proceedings of the Combustion Institute*. DOI: 10.1016/j.proci.2020.08.024
- 5) De Falco, G., Picca, F., Commodo, M., Minutolo, P. "Probing soot structure and electronic properties by optical spectroscopy"(2020) *Fuel*, 259. DOI: 10.1016/j.fuel.2019.116244
- 6) Gentile, F.S., Picca, F., De Falco, G., Commodo, M., Minutolo, P., Causà, M., D'Anna, A. "Soot inception: A DFT study of  $\sigma$  and  $\pi$  dimerization of resonantly stabilized aromatic radicals"(2020) *Fuel*, 279. DOI: 10.1016/j.fuel.2020.118491